GROWTH AND CHARACTERIZATION OF BORON NITRIDE AND CARBON NITRIDE THIN FILMS

OLIVIER COMETTO

School of Electrical and Electronic Engineering

A thesis submitted to the Nanyang Technological University in partial fulfillment of the requirements for the degree of Doctor of Philosophy

2018

Acknowledgements

First of all, I would like to thank my supervisor Prof. Edwin Teo who made me part of his research team and let me work on challenging projects. Throughout these four long years, he never ceased to encourage and guide me and I am very grateful for learning so much and for being considered as much a friend as a student.

In addition to Edwin, my gratitude goes to his team, especially Tony Tsang for his guidance and ideas that would help me go forward, Manuela Loeblein who started at the same time as me and was always in “the same boat”, Roland Tay for the after-work drinks, and also Li Hongling, Feini Leong and Jing Lin for their help and support.

I would also like to acknowledge the CINTRA (CNRS-Thales-NTU Alliance) lab people, such as my lunch buddies who would entertain me with their discussions and opinions: my brother Mathieu Cometto, Loic Loisel, Ange Maurice, Étienne Rodriguez “la merguez”, Denis Le Goff, Umar Saleem, Ran Xu, Meshal Sinnen and many others who shared the coffee room with me. Many thanks to Prof. Philippe Coquet for enabling partnerships with other research groups through the CINTRA lab and giving me a desk with a window view, as well as Jing Fei for facilitating the administrative procedures. Special mention to Hasman Bin Hassan, without whom nothing in the lab would be working. His hands-on expertise and knowledge on lab equipment, as well as his life advice greatly contributed to the completion of my thesis.

Finally, nothing would have been possible without my wife Jade, who would remind me to enjoy life, her parents and their awesome cooking, and my parents who would come visit my brother and I at least once a year to make sure we were working!

Olivier Cometto

Singapore, August 2017

Abstract

This thesis focuses on Boron Nitride (BN) and Carbon Nitride (CN) thin film nanostructuring. Inspired by its carbon counterpart, BN and CN nanocrystal orientation can be tailored to align themselves in the vertical direction. This material "texturing" at the nanoscale opens up opportunities for uncovering new interesting properties in materials, and the synthesis and properties of textured BN and CN is studied in this work.

Firstly, a new growth method based on High Power Impulse Magnetron Sputtering (HiPIMS) was created in order to grow BN thin films: A Lanthanum Hexaboride (LaB6) target was reactively sputtered in argon and nitrogen gas. Under specific growth conditions, dependent on temperature and sputtering power density, h-BN nanocrystals with the basal planes aligned in the vertical direction were obtained. The growth mechanism involving the change in alignment to produce vertically ordered BN (*voBN*) was studied and attributed to the compressive stress applied on the film during growth, where the maximum amount of stress would produce the best alignment. This novel crystalline structure displayed an improvement in thermal conductivity (TC) in the through plane direction by a factor 3 (at 5.1 $W.m^{-1}.K^{-1}$) compared to a randomly aligned BN film (1.7 $W.m^{-1}.K^{-1}$), and it was attributed to the vertical texturing, which facilitates the phonon transport in the through film direction.

In order to verify the assumption that the phonons move preferentially along the basal planes in the vertical direction, additional thermal characterization was performed using 3 omega, ascertaining an anisotropy in thermal transport with an in plane TC of 0.26 $W.m^{-1}.K^{-1}$, while the through plane TC was found to be 16 times greater at 4.26 $W.m^{-1}.K^{-1}$. Molecular Dynamics (MD) simulations were used to

successfully re-enact the TC anisotropy observed experimentally, attributing the difference to the many interfaces between crystalline and amorphous regions and the preferential phonon propagation along the vertically ordered crystalline basal planes. COMSOL Multiphysics simulations were used to quantify the performance of *voBN* at preventing heat cross talk, allowing an increase by a factor of 4 in hot spot density compared to SiO_2, without inducing any temperature increase.

Finally, some carbon and CN thin films with different nanostructuring were studied. Transient Grating Spectroscopy (TGS) was used to study the Surface Acoustic Waves (SAW) decay in the films, and deduce the thermal diffusivity of the substrate-thin film pair. Pure carbon films, together with CN films were produced with amorphous and vertically ordered structure in order to study the effect of nanostructure on the thermal diffusivity. Vertically ordered CN exhibited an enhanced thermal diffusivity response compared to a-CN with a greater value by a factor 3. It was deduced that this increase is mostly driven by the difference in nanostructuring. In addition, it was shown that the nitrogen content in the film plays a key role in the thermal diffusivity value, and it is assumed that its presence in a film decreases the atomic ordering, thus impeding the phonon transport.

Table of Contents

Acknowledgements....................3

Abstract....................4

Abbreviations....................17

Chapter 1- Introduction....................19

1.1 Background....................19

1.2 Motivation....................20

1.2.1 Objectives....................21

1.3 Scope definition....................22

1.4 Chapter order....................22

1.5 Contributions....................22

1.5.1 Journal articles....................22

1.5.2 Conferences....................24

Chapter 2 - Literature review....................25

2.1 Introduction....................25

2.2 Carbon....................26

2.2.1 Overview on carbon....................26

2.2.1.1 Introduction to carbon....................26

2.2.2 Nanocrystalline Graphite (NCG)....................27

2.2.2.1 Compressive stress in carbon thin films....................27

2.2.2.2 Other models....................31

2.2.2.3 Origins of NCG....................32

2.2.2.4 NCG's properties....................34

2.2.2.5 NCG's potential applications....................35

2.3 Boron Nitride....................36

2.3.1 Hexagonal Boron Nitride....................36

2.3.2 Cubic Boron Nitride....................37

2.3.3 Relation between compressive stress and sp^2/sp^3 bonding....................38

2.3.4 h-BN monolayer and BNNTs....................40

2.4 Carbon Nitride....................42

2.4.1 Graphitic C_3N_4 (g-C_3N_4)....................42

2.4.2 Beta C_3N_4 (β-C_3N_4)....................42

2.4.3 Amorphous carbon nitride (a-CN or CN_x)....................43

2.5 Main parameter affecting structuring: Stress in thin films....................44

2.5.1 Introduction....................44

2.5.2 Types of stress....................44

2.5.3 Stoney's equation........46

2.5.4 Growth induced compressive stress........48

2.6 B, C, N compound PVD growth techniques........50

2.6.1 Pulsed Laser Deposition (PLD)........50

2.6.2 Sputtering........51

2.6.3 Ion Implantation........51

2.6.4 Filtered Cathodic Vacuum Arc (FCVA)........52

2.6.5 High Power Impulse Magnetron Sputtering (HiPIMS)........53

2.7 Conclusion........54

2.8 References........55

Chapter 3- High Power Impulse Magnetron Sputtering (HiPIMS)........59

3.1 Introduction........59

3.2 Description........60

3.2.1 Direct Current Magnetron Sputtering........60

3.2.2 HiPIMS........61

3.2.3 Comparison with FCVA........62

3.2.3.1 Plasma density........63

3.2.3.2 Deposition rates........63

3.2.3.3 Plasma energy........63

3.2.3.4 Scalability and cost effectiveness........64

3.2.3.5 Conclusion........64

3.3 Current work using HiPIMS........65

3.3.1 Theoretical study of HiPIMS........65

3.3.1.1 Defining HiPIMS........65

3.3.1.2 Target ionization rate........66

3.3.1.3 Growth parameters........67

3.3.1.4 Plasma density inhomogeneity........67

3.3.2 Growth of metal based thin films with HiPIMS........69

3.3.3 Growth rate study........70

3.3.4 Growth of non-metals........72

3.4 HiPIMS setup in the lab and upgrades........72

3.4.1 System upgrades........73

3.4.1.1 Hardware upgrades........73

3.4.1.2 Dual-HiPIMS setup........74

3.4.1.3 Grow automation........75

3.4.2 System failures and modifications........77

3.4.2.1 HiPIMS power supply transistor failure........77

3.4.2.2 Bias voltage issue due to arcs........78

3.4.2.3 Water cooling issue and need to change to an internal cooler............79

3.4.2.4 N connector cable burn due to overheating and arcs..........................79

3.4.2.5 Target cracking...79

3.5 Conclusion...81

3.6 References...82

Chapter 4- A study of vertically ordered Boron Nitride grown with HiPIMS............84

4.1 Introduction...84

4.1.1 Rationale...84

4.1.2 Work performed...85

4.2 Experimental setup...86

4.2.1 Sample preparation..86

4.2.2 Sample characterization...86

4.2.3 Thermal Conductivity characterization..87

4.3 Results and discussion...88

4.3.1 HiPIMS setup optimization for BN growth......................................88

4.3.2 Microstructural characterization of the BN samples......................89

4.3.3 Film ordering and film stress dependency......................................92

4.3.3.1 FTIR characterization of the films..92

4.3.3.2 Film stress and impact on nanostructure...................................95

4.3.4 Compressive stress theory for HiPIMS growth...............................98

4.3.5 c-BN nanocrystals seeds for t-BN..101

4.3.6 Lanthanum content in the film...105

4.3.7 Impact of the gas ratio on *voBN* growth......................................106

4.3.8 Cross-plane thermal conductivity of *voBN*..................................107

4.4 Conclusion...110

4.5 References...111

Chapter 5– The anisotropic thermal conductivity of vertically ordered Boron Nitride 113

5.1 Introduction...113

5.1.1 Rationale...113

5.1.2 Work performed...114

5.2 Experimental setup...115

5.2.1 Sample preparation..115

5.2.2 Thermal characterization...115

5.2.3 Molecular Dynamics (MD) simulation...116

5.2.3.1 Amorphous BN generation through MD.................................116

5.2.3.2 TC computation for voBN..118

5.2.3.3 Thermal boundary conductance computation for the amorphous-crystalline interface......121
5.2.4 COMSOL Multiphysics simulation......122
5.2.4.1 Simulation model assumptions......122
5.2.4.2 Set of equations used in the model......123
5.2.4.3 Design of the mesh......124
5.3 Results and discussion......126
5.3.1 *voBN* microstructure verification......126
5.3.2 Dielectric constant computation......127
5.3.3 3ω thermal characterization......129
5.3.4 Molecular Dynamics results......132
5.3.5 *voBN* thermal crosstalk mitigation......138
5.4 Conclusion......142
5.5 References......144
Chapter 6– Texturing CN and its thermal properties......146
6.1 Introduction......146
6.1.1 Rationale......146
6.1.2 Work performed......147
6.2 Experimental setup......149
6.2.1 Sample preparation......149
6.2.2 Sample characterization......150
6.2.3 Transient Grating Spectroscopy......151
6.3 Results and discussion......152
6.3.1 Microstructure analysis......152
6.3.2 Thermal diffusivity analysis......156
6.4 Conclusion......163
6.5 References......164
Chapter 7– Conclusion and recommendations......165
7.1 Further research recommendations......168
7.1.1 Boron Nitride......168
7.1.1.1 Thermal performance test on actual devices......168
7.1.1.2 BN growth with a pure B target......168
7.1.1.3 Cubic BN growth with HiPIMS......169
7.1.1.4 High quality and large area h-BN monolayer growth......169
7.1.2 Carbon Nitride......169
7.1.2.1 Full study of the thermal properties of CN......169
7.1.2.2 Dense CN phases with HiPIMS......170
7.1.2.3 Graphitic CN with HiPIMS......170

7.1.3 Boron Carbon Nitride....170
    7.1.3.1 Dual HiPIMS of CN and BN....170
    7.1.3.2 Thermal, mechanical and electrical study of BCN compounds....170
7.1.4 HiPIMS....171
    7.1.4.1 Ion gun upgrade....171
    7.1.4.2 Plasma simulation....171

Appendices....172

1.Appendix A - HiPIMS SOP....172
1.1.Preparing system to full readiness....172
1.2.Growth operating procedure....173
    1.2.1.Sample loading and unloading....173
    1.2.2.Experiment run in HiPIMS mode....174
    1.2.3.Experiment run in RF mode....176
1.3.Full system shutdown....177

2.Appendix B - HiPIMS maintenance....178
2.1.Standard maintenance work....178
    2.1.1.Chamber cleaning....178
    2.1.2.Vacuum gauge cleaning....178
    2.1.3.Magnetron cleaning....179
    2.1.4.Substrate holder cleaning....179
    2.1.5.Changing magnetron target....179

3.Appendix C – Experimental comparison of SiO_2 and *voBN*....180
3.1.Thin film on heater simulations....180
3.2.Heat sink coupled simulations....181
3.3.Testing the anisotropy of voBN....184

Table of figures

Figure 2.1 - Summary of some material properties for different carbon allotropes. ‖ means in-plane (along the hexagonal sheets) while ⊥ is out-of-plane direction (between 2 hexagonal sheets). RT stands for Room Temperature...27

Figure 2.2 - The P-T phase diagram of carbon with the Berman-Simon curve. The different points in the diagram are the carbon film growth for various ion energies and their computed compressive stress values.27...28

Figure 2.3 - McKenzie's work on correlating compressive stress with ion energy during growth for carbon thin film.[26]...29

Figure 2.4 - Summary of several works on ta-C growth summarized by Marks................30

Figure 2.5 - A refined P-T phase diagram for carbon showing the amorphous regions at low temperature..30

Figure 2.6 - The 4 main models for the formation of ta-C are described. Atomic peening is based on a pressure pulse and relaxation, subplantation is based on sub-surface densification, thermal spike relies on the melting then fast quenching and compressive stress is focused on the biaxial stress in the thin film.[29]...32

Figure 2.7 - (A) Cross section HRTEM of a NCG film, where the preferred orientation of the graphitic basal plane is perpendicularly aligned with the silicon substrate. (B) Plane view of a NCG film, showing the onion-like rings of the characteristic tubular nanostructure of NCG.[25]..33

Figure 2.8 - Amorphous carbon film density as a function of compressive stress grown with ion energies ranging from 35 to 1000 eV. The dashed line is the predicted transition stress required to induce a change in nanocrystalline structure while the grey zone is the experimental zone where the change occurs.[37]..34

Figure 2.9 - Thermal conductivity of the carbon film depending on the degree of their planar orientation (which is directly linked to the deposition temperature).[33].....................35

Figure 2.10 - Representation of the hexagonal BN structure with A-B stacking................36

Figure 2.11 - Comparison of h-BN with graphite. ‖ means in-plane (along the hexagonal sheets) while ⊥ is out-of-plane direction. *the references for graphite's values are given in Figure 2.1...37

Figure 2.12 - Representation of the cubic BN structure...38

Figure 2.13 - Comparison between c-BN and diamond. *the references for diamond's values are given in Figure 2.1...38

Figure 2.14 - The P-T phase diagram for BN with the region in which c-BN can be obtained with the use of catalysts as well as the Berman and Simon boundary line between the cubic and hexagonal phases.[38]...39

Figure 2.15 - Percentage of cubic BN in the thin film grown at 500 degK, in relation with the compressive stress...40

Figure 2.16 - Phase diagram of CNx for varying deposition temperature and: nitrogen film concentration (left) or degree of ion bombardment (right) for reactive DC sputtering deposition techniques.[81]...43

Figure 2.17 - (a) Thin film and substrate without any stress in between. (b) Compressive stress induced by the substrate compressing the thin film. (c) Tensile stress induced by the substrate, applying a stretching force to the film. The red arrows indicate the compressive and stretching forces applied to the thin film..45

Figure 2.18 - Plot of equation 2.5 with $\frac{R}{j}=5$ and $k=0.1$, The curve shows a maximum at an energy of 6.29 eV........49

Figure 3.1 - Working principle of a magnetron sputtering process........61

Figure 3.2 - Left: Pulsed voltage and current discharge cycle.[2] Right: Comparison table between HiPIMS and a DC magnetron........61

Figure 3.3 - HiPIMS system during carbon film growth a 1000 degC........62

Figure 3.4 - Classification of various pulse discharges and where the HiPIMS region is. MPP stands for Modulated Pulse Power and is an in-between regime between HiPIMS and DCMS.[16]........65

Figure 3.5 - Picture of a used carbon target displaying the typical racetrack due to the spokes of plasma always moving along the same circular region........68

Figure 3.6 - Influence of peak current density J_d and Ar pressure P_{Ar} on the discharge: (a) and (e) $J_d=0.75$ A.cm^{-2}, $P_{Ar}=0.17$ Pa; (b) and (f) $J_d=7.5$ A.cm^{-2}, $P_{Ar}=0.17$ Pa; (c) and (g) $J_d=7.5$ A.cm^{-2}, $P_{Ar}=1.0$ Pa; (d) and (h) $J_d=7.5$ A.cm^{-2}, $P_{Ar}=1.7$ Pa. Upper row: fast photography frames (false color), lower row: total light intensity vs azimuthal angle corresponding to a circle along the centre of the racetrack. Angle is counted clockwise.[21]........68

Figure 3.7 - Left: Plasma discharge of a copper target in DCMS mode at 200 W average power, or 4.5 W.cm^{-2} peak power density. The pink colour comes from the argon gas which is being ionized by the glow discharge. Right: Plasma discharge of a copper target in HiPIMS mode at 200 W average power, or 25 W.cm^{-2} peak power density. The green colour comes from the ionized copper and the vertical lines come from the pulsing of the plasma combined with the shutter speed of the camera........70

Figure 3.8 - The deposition rates for DCMS and HiPIMS discharges plotted as bars for the different target materials used (left axis). The deposition rate of HiPIMS over DCMS deposition rate is shown as a scatter plot (right axis).[8]........71

Figure 3.9 - (a) HiPIMS system as first delivered, including one HiPIMS power supply and magnetron source. (b) Upgraded system comprising two HiPIMS power supplies, two magnetron sources, a HiPIMS pulse synchronization unit, one RF power supply and its own closed circuit water cooling system........74

Figure 3.10 - HiPIMS controller software, using the COM port to communicate: either send data using the right hand side of the window (inset (ii)) or receive live status info in the left hand side (inset (i))........76

Figure 3.11 - VBA code for excel to automate the cycles of growth and cooldown. This code relies on the use of VBA libraries to use the COM ports to communicate with the HiPIMS power supply. Inset (a) is the data in the excel spreadsheet with the left column being specified by the user and the right column status update from the VBA code..........77

Figure 3.12 - (a) Brand new DC bias connection between the metallic lamellas (connected to the DC power supply) and the shaft holder the substrate holder. (b) Same shaft and lamellas after electrical breakdowns have occurred and the DC bias function stopped working........78

Figure 3.13 - (a) Brand new N type coaxial cable. (b) Same N type coaxial cable after heavy usage. (c) Same coaxial cable as in (b) without the metallic connector, showing extensive heat damage........79

Figure 3.14 - Picture of LaB_6 target that cracked due to the different coefficient of thermal expansion between the target, the copper magnetron and the Mo target holder.. 80

Figure 4.1 - (a) HRTEM of a BN film grown at room temperature with floating bias showing the interface between the film and silicon substrate. A transition layer of ~6 nm is located at the interface before the vertically ordered structure starts. The smooth interface implies a good film adhesion and no damage to the substrate. The top FFT shows a normal orientation along the (0002) plane, with an inter-planar distance of 0.35 nm. (b) HRTEM of the same film taken in the middle region with its FFT displaying compact partial circles, which indicates normal orientation.[21]..91

Figure 4.2 - Step by step FTIR data processing before computing the peak ratio. Inset (a) displays the raw data taken from the FTIR measurement. Inset (b) Shows the truncated data between 600 and 2000 cm^{-1} and the curve smoothing. Inset (c) represents the baseline computation and inset (d) is the final result after the baseline has been subtracted from the smoothed data.[21]..93

Figure 4.3 - Peak ratio computation of a FTIR spectrum for an ordered h-BN thin film. In order to facilitate the ratio computation, the spectrum is normalized between 0 and 1, making the 1380 cm^{-1} peak the 0 value. The ratio would then be $1-I_{770}$ where I_{770} is the 770 cm^{-1} peak intensity.[21]..94

Figure 4.4 - FTIR spectra of BN samples. The h-BN powder is a high purity powder made of 10 µm particles. The c-BN/t-BN film was grown with HiPIMS at 500 degC, 0 V substrate, and peak power density of $200W.cm^{-2}$. The ordered h-BN sample was grown with HiPIMS at room temperature and 60 $W.cm^{-2}$ peak power density. The computed $R_{770/1380}$ peak ratio for ordered h-BN, c-BN/t-BN and h-BN powder is respectively 0.51, 0.19 and 0.29.[21]..95

Figure 4.5 - Top: Film stress in function of the applied bias voltage and the FTIR peak intensity ratio between the in-plane response at 1380 cm^{-1} and the out-of-plane response located at 770 cm^{-1}. Bottom: Compressive stress value for films grown at different temperatures and bias. The lowest bias is 0 when the substrate holder is connected to the ground. The value at -47 V is the floating bias.[21]..97

Figure 4.6 - Curve plotted from the stress curve formula given by McKenzie depicting the compressive stress depending on the ion energy for carbon. Assuming a similar curve distribution for boron nitride, the current results are located at the high ion energy portion as shown in the inset, displaying the computed compressive stress for ordered h-BN films grown at room temperature.[21]..100

Figure 4.7 - HRTEM of a BN film deposited with a bias of -200 V at 600 degC and a HiPIMS maximum power density of 200 $W.cm^{-2}$. The film is highly disordered, with c-BN nanocrystals of 5 nm, embedded in a matrix of turbostratic sp^2 BN made of the hexagonal and/or rhombohedral structure. (a) is the FFT of the whole image, displaying the characteristic rings for turbostratic BN: the inner (0.36 nm/cycle) and outer (0.21 nm/cycle) rings are induced respectively by the random orientation of the h-BN (0002) and c-BN (111) configurations. (b) and (c) are respectively the FFT of the green (top) zone containing c-BN and the blue (bottom) zone made of h-BN/r-BN.[21]..102

Figure 4.8 - 2θ scan of c-BN/t-BN sample with ω fixed at 3.712°. 2 Gaussian curves are used to fit the graph, which is contributed by c-BN (111) and h-BN (101) respectively. The fixed ω is determined by rocking curve scan on the c-BN/t-BN sample at various phi angles to detect the (111) plane of c-BN at 2θ of 43.314°. A weak peak is detected at ω of 3.712° for the rocking curve scan.[21]..103

Figure 4.9 - Cross-section TEM image of a c-BN nanocrystal and its interface with t-BN and amorphous BN. The c-BN crystal induces changes in the film morphology at the nanoscale due to the change in orientation between the cubic and hexagonal phases. The t-BN planes will preferentially orientate themselves such that the lattice mismatch is minimized, i.e. 45°..103

Figure 4.10 - XRD results for the vertically ordered h-BN film. (a) shows the XRD response for the sample. The particle size was computed using a Gaussian fitting of the

curve and applying Scherrer equation. (b) is the rocking curve, showing a sharp peak indicating the 002 plane is highly oriented.[21]..104

Figure 4.11 - Measurement of the relative atomic % composition of the film using EELS. (a), (b) and (c) respectively show the EELS spectra of B, N and La. (d) Computed atomic concentration of boron (blue), nitrogen (red) and lanthanum (green). The ratio of B and N indicates a BN film stoichiometry of 1.15. The lanthanum content is constant at around 7.5 at.%. The measurement is made along the whole film as shown in (e).[21]............................105

Figure 4.12 - In-plane h-BN FTIR peak centre depending on the nitrogen content during thin film growth. The zone represents the area for which the peaks indicate high quality h-BN crystals. Above values of 25% nitrogen content, h-BN of high quality is consistently obtained...107

Figure 4.13 - Table summarizing the thermal conductivity of various amorphous materials such as BN, as well as textured carbon which is similar in structure to ordered h-BN.[21]..109

Figure 5.1 - Comparison of the RDF between amorphous BN (a) and hexagonal BN (b). 118

Figure 5.2 - Schematics of the simulation models for the thermal conductivity along (a) the inter-plane and (b) the intra-plane directions of the crystalline h-BN phase. The simulation model for the thermal conductivity of the amorphous BN is similar to that for the crystalline h-BN layers and thus is not shown here. The region highlighted with red in the middle is set as the heat source region and held at the temperature at T+ΔT, and the regions highlighted with blue at the two ends are set as heat sinks and held at a lower temperature of T.[28]..119

Figure 5.3 - Schematics of the simulation models for the calculation of the thermal conductance of the interface between the crystalline h-BN layers and amorphous BN with (a) intra-plane covalent bonding and (b) inter-plane non-covalent bonding. The region highlighted with red at the left end is set as the heat source region and held at the temperature of $T+\Delta T$. And the region highlighted with blue at the right end is set as the heat sink and held at a lower temperature T . Atoms in thin slabs with a width of ~2 Å near the heat source and sink are fixed as rigid.[28]..122

Figure 5.4 - Unit cell where thermal crosstalk will be simulated.[28]....................................123

Figure 5.5 - Comparison of isothermal contours simulations with SiO_2 around the hot spot with a bad mesh (a) and a good mesh (b). It can also be observed that the computed temperatures between both simulations are not the same. Inset (c) and (d) show the difference in meshing quality for both simulations.[28]...125

Figure 5.6 - (a) High resolution cross section TEM image of a vertically ordered BN thin film. The top left image is a zoom-in showing in more detail the BN crystal lattice with vertical alignment. The vertical alignment is further confirmed by the computed FFT which displays the typical partial rings for the (0002) h-BN planes with alignment perpendicular to the substrate plane. The outer ring corresponds to the (-2110) h-BN plane. (b) FTIR response for a typical BN film with h-BN planes vertically ordered with respect to the silicon substrate. The determining criteria is a value above 0.5 when computing the normalized ratio between the in-plane and out-of-plane IR active modes.[28] 127

Figure 5.7 - Inset (a) is a photo of the device, with the area of the top copper electrode computed to be 3.41 cm^2. Inset (b) is a schematic of the design in cut view. The *voBN* film thickness was computed to be 600 nm via surface profiling.[28]..128

Figure 5.8 - (a) is a plot of the imaginary part of the complex impedance. (b) is a plot of $\frac{-1}{2\pi X}$ and is linearly fitted in order to extract the capacitance. The computed slope is

45×10^{-6} , which gives a capacitance of 45 nF (there is a factor 1000 due to the plot axis being in kHz instead of Hz).[28]....129

Figure 5.9 - (a) The experimental and the calculated temperature oscillation for the 40 µm wide wire deposited on BN/Si and reference (bare Si), respectively. The temperature difference between the Si substrate and the BN/Si is used to calculate the cross-plane thermal conductivity of BN film on Si substrate. (b) (i) The experimental temperature oscillation for the 4 µm wide deposited wire on BN/Si and corresponding fitting curve from the two-dimensional heat conduction model and calculated curve for ±20% change in the best fitted value for K_x. (ii) The experimental temperature oscillation for 10 µm wide deposited wire on BN/Si and corresponding calculated curve from the two-dimensional heat conduction model based on the Ky, and the fitted K_x and $R_{BN\text{-}Si}$ values determined by fitting the 4 µm wide heater.[28]....132

Figure 5.10 - Temperature distribution and the accumulative energy changes with the simulation time between 2 planes (a, b) and within the same plane (c, d) directions for the crystalline h-BN.[28]....133

Figure 5.11 - Temperature distribution along the heat flux direction for the hybrid system of the crystalline h-BN and amorphous BN with covalent-bonded interface shown in Figure 5.1a. The red lines are drawn to guide the eye.[28]....134

Figure 5.12 - Series chain model for the calculation of thermal conductivity along the (a) through plane and (b) in plane directions.[28]....135

Figure 5.13 - The dependences of (a) the out-of-plane, (b) the in-plane thermal conductivities and (c) the anisotropic ratio between them on the grain size of the crystalline h-BN.[28]....137

Figure 5.14 - Phonon spectra of the amorphous BN and crystalline h-BN in the 0 to 80 THz bandwidth.[28]....138

Figure 5.15 - Isothermal contours around the hot spot for SiO_2 (a) and *voBN* (b). The spherical contour shape in SiO_2 is the typical response from isotropic materials while the stretched contours along the z axis for *voBN* is characteristic of a material with greater thermal conductivity along the z axis compared to the x and y axis.[28]....139

Figure 5.16 - Cross section image (as per the inset image) of the isothermal contours for the temperature response of a hot spot (0.1 W heat source) heating up from the bottom a 100 µm cubic structure. The diagram on the left is for the case of a device made of SiO_2 while the one on the right is a device made of *voBN*. The anisotropy of *voBN* induces an elongated temperature response in height, while keeping the in-plane temperature spread more compact compared to SiO_2.[28]....139

Figure 5.17 - Temperature line plot (inset a) along the temperature line as shown by the vertical dotted arrow located at a distance of d/2 from the hot spot in the unit cell schematic (inset c). The distance d is the square dimensions in the xy plane, which can be seen as the distance between two adjacent hot spots. Each line represents the temperature variation across the 100 µm thick layer, for various hot spot distances. The temperature response of SiO_2 is sandwiched between two *voBN* responses with closer hot spot distances: 50.3 and 54.1 µm. Inset b shows the stretched isothermal contours in the vicinity of a hot spot due to the anisotropic nature of *voBN*.[28]....141

Figure 6.1 - Phase diagram of CN_x for varying deposition temperature and nitrogen film concentration for reactive deposition techniques.[14]....147

Figure 6.2 - Summary of the successful recipes used for the growth of carbon and carbon nitride thin films. All films are grown using HiPIMS except the NCG sample which was grown using FCVA based on a technique reported elsewhere.[18]....149

Figure 6.3 - (a) A cross-section TEM of an amorphous carbon film. EELS measurements give a 81% sp^2 content in the film. (b) FIBTEM of an amorphous carbon nitride film.

EELS measurements give a 93% sp^2 content in the film and an at.% of C and N of respectively 85.21% and 14.79%......152

Figure 6.4 - (a) A cross-section TEM of the NCG film with a 82% sp^2 content. The computed FFT image in the inset at the top of the image shows partial circles indicating an interplanar distance of 0.34 nm corresponding to the 002 direction. (b) FIBTEM of the fullerene-like carbon nitride film. EELS measurements give a 88% sp^2 content in the film with an at.% of C and N of 77.82% and 22.18% respectively. The inset located on top is showing the computed FFT of the image and its circle indicating an interplanar distance of 0.44 nm......154

Figure 6.5 - Raman spectrum of the NCG sample (noisy line) and its curve fitting in thick green color (Lorentzian for the D peak and BWF for the G peak). The red dotted line is the sum of both the Lorentzian and BWF fit which is a close match to the actual Raman response. I(D)/I(G) is 1.28 and the G peak centre is 1585 cm^{-1}.[28]......155

Figure 6.6 - Raman spectra for all 4 samples. The D and G peak regions are shown in here. Each spectrum shows a different shift for the G peak, which is a clue to the nanocrystalline structure of the film.[28]......156

Figure 6.7 - Surface acoustic waves decay after excitation by the grating. The exponential decay curve is input into a fitting model in order to compute the thermal diffusivity of the film-substrate system. The small sinusoidal oscillations are due to the elastic properties of the material. The dashed line in each plot is the zero line.[28]......157

Figure 6.8 - Thermal diffusivity value for each sample. As the excitation wavelength is 7.4 µm deep, the thermal diffusivity value is made of a two-layer system made of the 150 nm thick C or CN film + several microns of silicon 100, which has a thermal diffusivity of around 6x10-5 m^2/s.[28]......159

Figure 6.9 - Sheet resistance measurement on all 4 samples. The y axis is in log scale to account for the wide range in measurements between the amorphous and graphitic samples......161

Figure 1 - Simple COMSOL simulation of the thermal behaviour of a 1 cm x 1 cm heater. The power output is 1 W and the bottom surface has a temperature condition set to 25 degC. The top surfaces are cooled down by natural air convection. A symmetry condition is used on the x-z and y-z planes to divide by 4 the computation time......181

Figure 2 - Simple COMSOL simulation of the thermal behaviour of a 1 cm x 1 cm heater with a 1 cm high heatsink on top. The power output is 10 W and the bottom surface has a temperature condition set to 25 degC. The top surfaces are cooled down by natural air convection, except for the top surface of the heatsink which has a temperature condition of 25 degC. A symmetry condition is used on the x-z and y-z planes to divide by 4 the computation time......184

Abbreviations

BN	Boron Nitride
CN	Carbon Nitride
HiPIMS	High Power Impulse Magnetron Sputtering
LaB_6	Lanthanum Hexaboride
h-BN	Hexagonal Boron Nitride
voBN	Vertically ordered BN
TC	Thermal Conductivity
SiO_2	Silicon Dioxide
TGS	Transient Grating Spectroscopy
SAW	Surface Acoustic Wave
a-CN	Amorphous CN
UTS	Ultimate Tensile Strength
DLC	Diamond-Like Carbon
CNT	Carbon Nanotube
degC	Degree Celcius
EC	Electronic Circuit
BCN	Boron Carbon Nitride
c-BN	Cubic BN
a-C	Amorphous Carbon
FCVA	Filtered Cathodic Vacuum Arc
Ta-C	Tetrahedral a-C
HPHT	High Pressure High Temperature
GPa	GIgapascal
eV	Electron-volt
UV	Ultraviolet
CVD	Chemical Vapor Deposition
CNTFET	CNT Field Effect Transistor
NCG	Nanocrystalline Graphite
HRTEM	High Resolution Transmission Electron Microscope
t-BN	Turbostratic BN
r-BN	Rhombohedral BN
w-BN	Wurtzite BN
BNNT	BN Nanotube
TEM	Transmission Electron Microscope
PVD	Physical Vapor Deposition
PECVD	Plasma Enhanced CVD
PLD	Pulsed Laser Deposition
DCMS	Direct Current Magnetron Sputtering
RF	Radio Frequency
ECR	Electron Cyclotron Resonance
MPP	Modulated Pulse Power
IEDF	Ion Energy Distribution Function
CIV	Critical Ionization Velocity
SOP	System Operational Procedure
MFC	Mass Flow Controller
EELS	Energy Electron Loss Spectroscopy

AFM	Atomic Force Microscopy
FTIR	Fourier Transform Infrared Red spectroscopy
XRD	X-Ray Diffraction
TDTR	Time-Domain Thermoreflectance
FFT	Fast Fourier Transform
MD	Molecular Dynamics
LJ	Lennard-Jones
UFF	Universal Force Field
IC	Integrated Circuit
IBAD	Ion Beam Assisted Deposition
BWF	Breit Wigner Fano
RDF	Radius Distribution Function
LAMMPS	Large-scale Atomic/Molecular Massively Parallel Simulator

Chapter 1 - Introduction

1.1 Background

Materials science relies on exploiting the peculiar and unique properties of materials in order to achieve a desired outcome. These properties range from macro properties such as hardness, elasticity or even color and transparency, to micro properties, where materials can generate heat (phonons), light (photons) or electricity (electrons). The bulk properties of materials were first used to make basic tools where hard materials were required. As technology evolves, the necessity for even harder and more versatile materials was met with structuring of materials, such as concrete reinforced with steel or using the honeycomb structure for instance.

In the last century however, and mostly with the advent of electronics, the properties of a material at the microscopic scale became important, and so did its microstructure. The most common example is carbon, which is most widely found in the graphite form but can also take the much rarer diamond form. Even though both graphite and diamond are made of carbon, they vary greatly in terms of their properties as a material, with graphite being electrically conductive and soft while diamond is a large bandgap material and the strongest material known to mankind. New materials with unique properties will open new ways of solving old engineering problems more efficiently, or simply be the key to unlocking currently impossible engineering feats that have been thought to be far out of reach.

Carbon is now more than just graphite and diamond: it can also be found in an amorphous state (a mixture of graphite and diamond at the atomic level), where the advantages of both crystalline structures can be mixed. In particular, textured carbon or nanocrystalline graphite (NCG), which is a nanostructured carbon thin film with its basal plane oriented normally to its substrate, has shown to have an excellent through plane thermal conductivity of up to 16 $W.m^{-1}.K^{-1}$, as compared with amorphous carbon which is less than 5 $W.m^{-1}.K^{-1}$.[1] Its capability to extract heat vertically as well as its simplicity to obtain at low temperature growth condition (i.e. below 200 degC) have unveiled its potential in thermal dissipation applications in electronics. Indeed, the trend for electronics to have its devices smaller and with more transistors while operating at the same power as before has recently led to overheating issues in devices. This problem, if not properly managed, can lead to a shorter lifespan in the best case, to complete device failure. Now that we are reaching sub micrometer scales in device fabrication, the need for new materials engineered especially for the purpose of heat extraction has become necessary, but is currently lacking. Textured carbon's high thermal performance could be a solution to this problem by directly extracting heat away from the hot spots. Unfortunately, it is electrically conductive and cannot be used for most of the devices, where an insulative material is necessary.

1.2 Motivation

As explained before, the discovery and study of NCG, which is a new form of nanostructure in carbon, has unveiled a new avenue for materials engineering at the nanoscale for the purpose of improving thermal performances at the macroscale. Even though NCG’s promising thermal performance opened a new path towards solving thermal issues in electronics, its intrinsic electrical conductivity prevents its use as a thermal material directly on the heat source in electronics. In a similar fashion as carbon, Boron Nitride (BN) has attracted interest due to its compatibility with carbon when it comes to its similar crystalline structure. This closeness in structure

---

1. M. Shakerzadeh, M. K. Samani, N. Khosravian, E. H. T. Teo, M. Bosman and B. K. Tay, *Carbon*, 2012, **50**, 1428-1431.

suggests that a BN equivalent of textured carbon phase could exist and a similar thermal improvement is expected while preserving its intrinsic insulative property. Such textured BN would have the potential to become an ideal material for heat dissipation purposes due to its high thermal conductivity and the fact that it could be directly applied on top of the hot spots without creating any electrical shorts. The motivation behind this work is to create this new textured BN material and study it as it has never been attempted before. In order to control the texturing of BN, a new growth method based on the High Impulse Magnetron Sputtering will be used as its high plasma energy will enable a better control of the growth parameters.

1.2.1 Objectives

The aim of this thesis is to grow textured BN and CN with HiPIMS and assess the change in thermal properties depending on the nanocrystalline structure. Assessing the thermal property here means to experimentally characterize it, as well as understanding the process behind the change in value between different crystalline structures.

The main objective above can be further broken down into several smaller sub-objectives. For instance, the HiPIMS setup will be tested first for BN and CN growth, then tuned to obtain high quality materials with proper crystalline structure, and finally maintained and upgraded during the whole thesis work. The second objective of texturing and studying the microstructure of BN and CN can be split into the following: one, the optimization of growth recipes to texture BN and CN, and two, the study of their microstructure depending on growth parameters. Finally, the in-depth thermal conductivity study of textured BN was performed in all directions, at the macroscale via experimental method, as well as the microscale via simulations.

1.3 Scope definition

This thesis will concentrate only on the growth and study of BN and CN with HiPIMS, focusing solely on the optimization of the growth parameters to control the crystalline structure during growth. Finally, the thermal properties of various BN and CN crystalline structures will be studied to understand the impact on nanostructure on thermal behavior.

1.4 Chapter order

Including this introduction chapter, this thesis contains 7 chapters. The next chapter is the literature review and will introduce all the background knowledge and research required to perform the research work on BN and CN textured growth. Chapter 3 will introduce the main growth method used for the rest of the research work, and how it was modified and upgraded to create novel and original research. The following chapters (4, 5 and 6) are summarizing the research work performed, respectively on: the nanostructuring study of BN, the anisotropic thermal properties of BN and finally the study of CN thermal and structural properties. Lastly, the conclusion chapter outlines the main achievements as well as what new work could be produced from those results.

1.5 Contributions

This section summarizes the list of contributions to the field in which I was involved and that contain the results obtained from the works to accomplish this PhD thesis.

1.5.1 Journal articles

- Cometto, O.; Sun, B.; Tsang, S. H.; Huang, X.; Koh, Y. K.; Teo, E. H. *"Vertically Self-Ordered Orientation of Nanocrystalline Hexagonal Boron Nitride Thin Films for*

Enhanced Thermal Characteristics" Nanoscale 2015, 7, 18984-18991 (the contents of this paper can be found in chapter 4). My personal contribution was to the research project planning and coordination, the samples preparation, the micro structure characterization (except the TEM, XRD and thermal measurements that were outsourced) and redaction of the manuscript.

- Cometto, O.; Samani, M. K.; Liu, B.; Sun, S.; Tsang, S. H.; Liu, J.; Zhou, K.; Teo, E. H. *"Control of Nanoplane Orientation in voBN for High Thermal Anisotropy in a Dielectric Thin Film: A New Solution For Thermal Hotspot Mitigation in Electronics"* ACS Appl Mater Interfaces 2017 (the contents of this paper can be found in chapter 5). My personal contribution was to the research project planning and coordination, the samples preparation, the micro structure characterization except for the TEM images and the thermal characterization that were outsourced), the COMSOL Multiphysics thermal simulations as well as the manuscript redaction.
- Jing, L.; Li, H.; Tay, R. Y.; Sun, B.; Tsang, S. H.; Cometto, O.; Lin, J.; Teo, E. H. T.; Tok, A. I. Y. *"Biocompatible Hydroxylated Boron Nitride Nanosheets/Poly(vinyl alcohol) Interpenetrating Hydrogels with Enhanced Mechanical and Thermal Responses"* ACS Nano 2017, 11, 3742-3751. My personal contribution in this work was limited to providing advice the first author.
- Jing, L.; Samani, M. K.; Liu, B.; Li, H.; Tay, R. Y.; Tsang, S. H.; Cometto, O.; Nylander, A.; Liu, J.; Teo, E. H. T.; Tok, A. I. Y. *"Thermal Conductivity Enhancement of Coaxial Carbon@Boron Nitride Nanotube Arrays"* ACS Appl. Mater. Interfaces 2017, 9, 14555-14560. My personal contribution was on a specific step of the sample preparation, requiring the growth of a thin layer of amorphous carbon.
- Cometto, O.; Dennett, C. A.; Tsang, S. H.; Short M. P.; Teo, E. H. T. *"A Thermal Study of Amorphous and Textured Carbon and Carbon Nitride Thin Films via Transient*

Grating Spectroscopy" Carbon 2018, 130, 355-361 (the contents of this paper can be found in chapter 6). My personal contribution was on the project planning and coordination, the samples preparation, the micro structure characterization (except for the TEM images and the thermal characterization that were outsourced) and the manuscript redaction.

1.5.2 Conferences

- Cometto, O. *"Thermal Conductivity of Vertically Self-Ordered Nanocrystalline Boron Nitride Thin Films for Enhanced Preferential Phonon Transport"*, Materials Research Society, Boston, Boston, 2015.

Chapter 2 - Literature review

2.1 Introduction

In this literature review, we will focus on concepts that are important for this thesis such as the materials studied. First carbon and in particular NCG, which laid out the groundwork for texturing materials at the nanoscale. Then BN and CN will be described in detail, with all their crystalline forms and properties. Then, compressive stress in thin films, which is one of the most important parameter affecting the material nanostructure will be described and explained as the notion of stress is important for the work of this thesis. Finally, a state of the art of various growths methods for carbon, BN and CN will be summarized, and especially the HiPIMS method will be introduced as well.

2.2 Carbon

2.2.1 Overview on carbon

2.2.1.1 Introduction to carbon

Carbon's most common allotropes are graphite, diamond and amorphous carbon (a-C). Those 3 different atomic structures differ mainly by the bonding type between carbon atoms, which is divided into 2 types: σ and π bonds. Diamond is solely made of carbon atoms arranged in a face-centered cubic fashion, and only made of σ bonds, which is the strongest covalent chemical bond,[1] and is referred to as sp^3 hybridized carbon (each atom is bonded to 4 atoms via a σ bond). This atomic structure is the reason why diamond is extremely hard and to this day, is the hardest known material. On the other hand, graphite is made of planar sheets of atoms with hexagonal structure arrangement, with each sheet stacked on top of each other and bonded with weak van der Walls forces. This structure is referred to as sp^2 hybridization, where each atom is linked to 3 other atoms with a σ bond and one weaker π bond. Graphite is much softer than diamond, and can conduct electricity,[2] unlike diamond which is an insulator.[3] In addition to those 2 structures, carbon can also be amorphous, which means it is neither graphite nor diamond, but a mixture of both at the nanoscale. Amorphous carbon or a-C varies in properties depending on its nanostructure, which can be quantified by its sp^2 to sp^3 ratio. a-C does not display any crystallinity and high sp^2 a-C is referred as graphitic a-C while high sp^3 is called tetrahedral a-C, ta-C or Diamond-Like Carbon (DLC). In addition to those 3 forms of carbon, a new class of nanomaterials has emerged with the successful synthesis of Carbon Nanotubes (CNTs) in 1991[4] and the discovery graphene in 2004[5]. CNTs, which are sheets of carbon in an honeycomb structure and folded upon themselves, exhibit many unique properties such as extremely high thermal conductivity (around 3500

$W.m^{-1}.K^{-1}$)[6] or can be either metallic or semiconducting depending on their tubular structure.[7] On the other hand, graphene is a monolayer single graphite sheet and this peculiarity yields unique results such as being the strongest known material with a tensile strength of 130 GPa[8] (in comparison, steel is below 1 GPa). In addition, graphene has high electron mobility at room temperature in the order of 15000 $cm^{-2}.V^{-1}.s^{-1}$ which is around 10 times greater than silicon.[5] The main carbon structures and some of their properties have been summarized in Figure 2.1 below:

	Diamond	**Graphite**	**Graphene**	**CNT**	**a-C**
Atomic structure	Face-centered cubic	Hexagonal	Hexagonal monolayer	Tubular hexagonal	Amorphous
Bond length (nm)	0.154[9]	0.142 ‖[10]; 0.3354 ⊥[11]	0.142[12]	0.142[12]	0.152 (sp^3) to 0.376 (sp^2)[13]
Density ($g.cm^{-3}$)	3.52[9]	2.09-2.23[11]	N/A	0.03-0.11 (SWNT forests)[14]	2.0 (high sp^2) to 2.7 (high sp^3)[15]
Bulk modulus (GPa)	443[16]	34[17]	N/A	462-546[18]	Approx. 200 (high sp^2) to approx. 400 (high sp^3)[19]
Bandgap (eV)	5.5[16]	N/A	0[12]	0 (metallic CNT), <0.1 (depends on diameter)[20]	1 (high sp^2) to 4 (high sp^3)[21]
Thermal conductivity at RT ($W.m^{-1}.K^{-1}$)	900-2320[22]	250 ‖; 80 ⊥[23]	600-3000[12] ‖	1.52[24] (off-axis); 3500[6] (along tube) for SWNT	1 (low density) to 4 (high density)[25]

Figure 2.1 - Summary of some material properties for different carbon allotropes. ‖ means in-plane (along the hexagonal sheets) while ⊥ is out-of-plane direction (between 2 hexagonal sheets). RT stands for Room Temperature

2.2.2 Nanocrystalline Graphite (NCG)

2.2.2.1 Compressive stress in carbon thin films

The study of stress in carbon films dates back to 1991 with McKenzie et al. demonstrating how tuning the ion energy during growth affects the ratio of sp^3 bonding in the formation of ta-C.[26] Based on the phase diagram of carbon deduced by Berman and Simon,[27] a minimum pressure value is required to induce diamond bonding during carbon growth as shown in Figure 2.2 below.

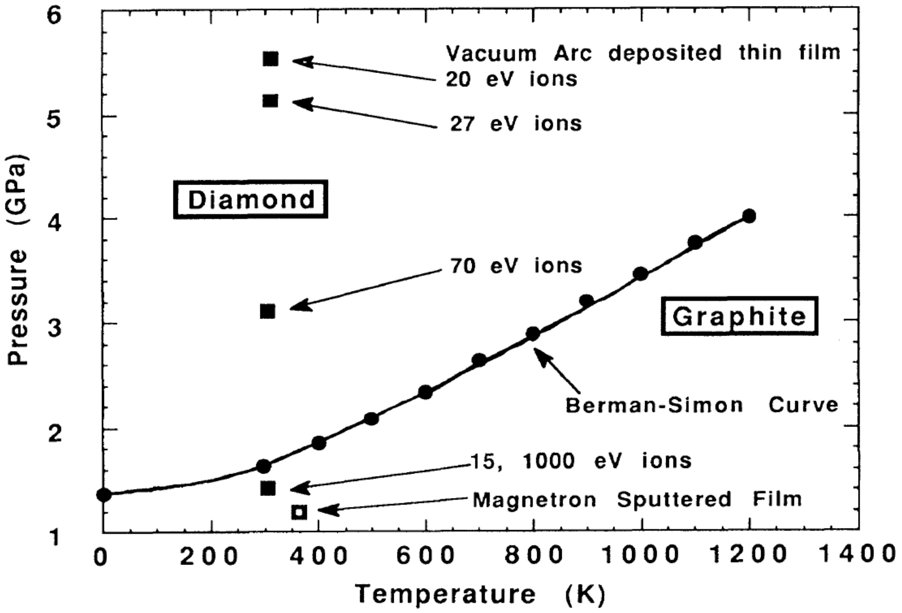

Figure 2.2 - The P-T phase diagram of carbon with the Berman-Simon curve. The different points in the diagram are the carbon film growth for various ion energies and their computed compressive stress values.[27]

The Berman-Simon curve in the P-T diagram provides the border between the pressure and temperature ranges for stable and preferred diamond phase, while the other side of the curve indicates the stable graphite region. It can be noticed that the Earth surface environment falls in the graphite region stability and thus diamond should not be able to exist. However, even though it is not stable, it will take millions of years to convert to graphite and is considered a metastable material at standard pressure and temperature conditions.

In their work on carbon, McKenzie et al. changed the ion energy of the carbon species by changing the bias voltage at the substrate. The compressive stress threshold for diamond bonding is the same as the pressure threshold between graphite and diamond, hence indicating that pressure in the phase diagram can be substituted by in-situ compressive stress following the following relation:[28]

$$P=\frac{2}{3}\sigma \qquad (2.1)$$

This simple equation links the pressure P and biaxial stress σ by a simple linear relation and allows a substitution of pressure in the P-T phase diagram with compressive stress. In addition, by correlating the ion energy with the compressive stress in the carbon thin film as demonstrated by McKenzie et al. in Figure 2.3 below, where a light trend can be seen, with an increase of stress with ion energy until it reaches a maximum at around 40-50 eV before decreasing again.

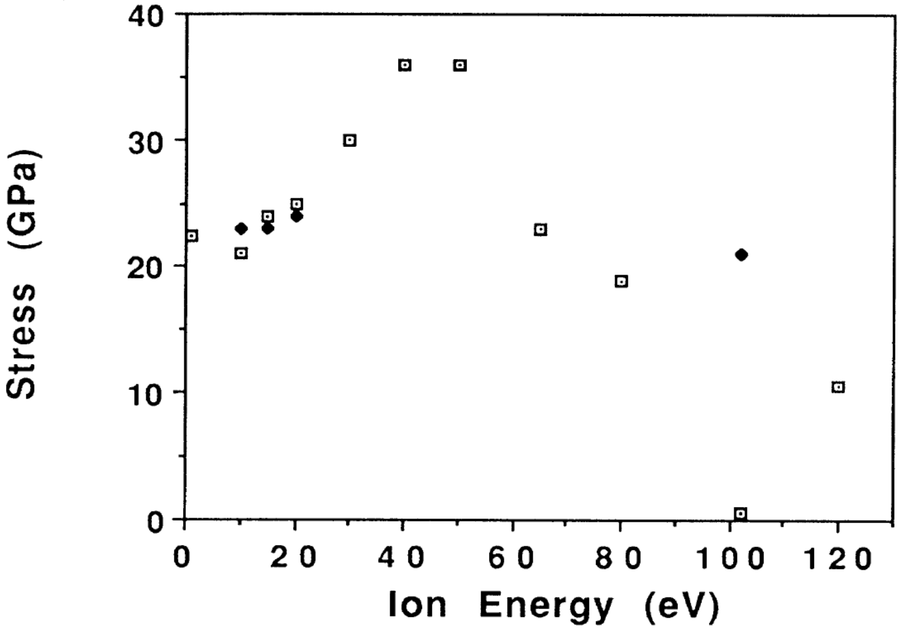

Figure 2.3 - McKenzie's work on correlating compressive stress with ion energy during growth for carbon thin film.[26]

Equation 2.1 true meaning is that looking for the highest compressive stress in the film is equivalent to increasing the pressure and hence moving "up" (in the higher pressure ranges) in the P-T diagram, so as to displace the carbon phase equilibrium into the diamond zone. This means that by tuning the ion energy to maximize compressive stress, diamond can theoretically be obtained. Marks summarizes the main research on ta-C growth in his book *Computer-Based Modeling of Novel Carbon Systems and Their Properties: Beyond Nanotubes* in the Figure 2.4.[29] Most research work agrees on a maximum sp^3 bonding ratio at around 100 eV ion energy, with a decrease in tetrahedral structure with increasing ion energy, in accordance with a decrease in compressive stress.

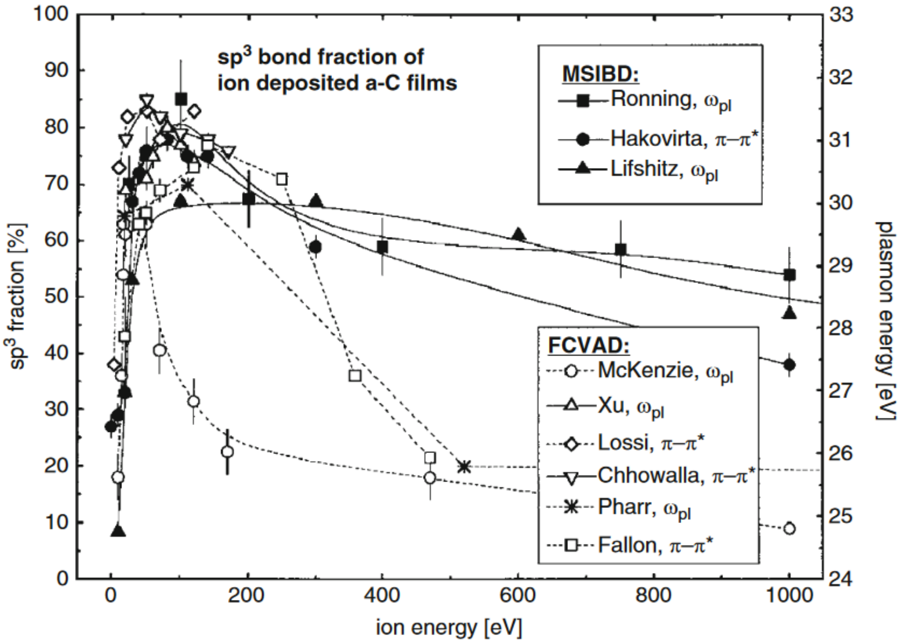

Figure 2.4 - Summary of several works on ta-C growth summarized by Marks.

Such work enabled the refinement of the carbon phase diagram by McKenzie,[30] to specify the amorphous regions along the Berman-Simon line as displayed in Figure 2.5.

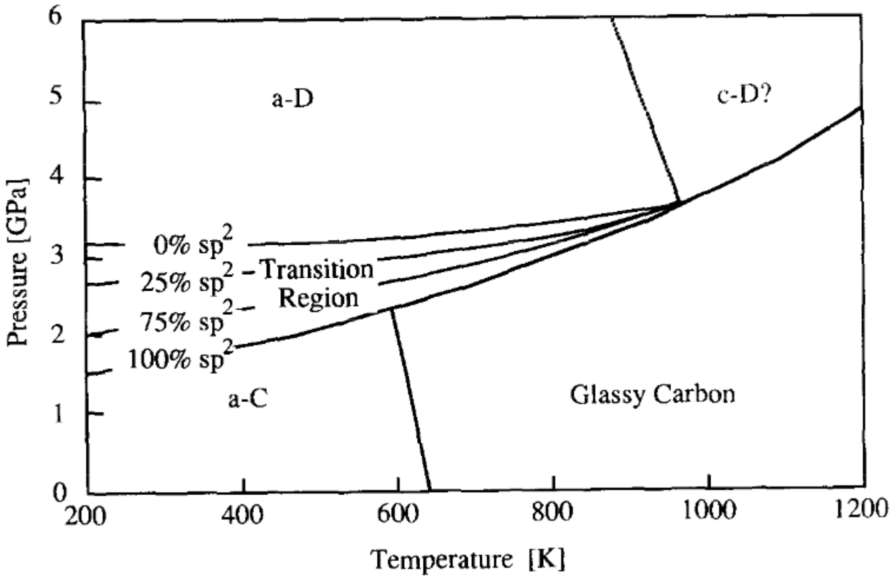

Figure 2.5 - A refined P-T phase diagram for carbon showing the amorphous regions at low temperature.

Glassy carbon is described as the first stage of crystallization of carbon, before becoming fully graphitic. The diagram also clarifies that there is no way currently of obtaining crystalline diamond at temperatures below 1000 degK, where temperature below would induce various degrees of amorphous structures depending on the amount of pressure (or compressive stress applied) applied to the thin film during growth, ranging from fully graphitic amorphous carbon to amorphous diamond (with 100% sp^3 bonding). In addition to the above summary of compressive stress in carbon thin films, a more general overview on stress in thin films is given in section 6 of this chapter.

2.2.2.2 Other models

In addition to the compressive stress theory to explain how ta-C is formed, several other models are competing or completing the story to properly explain the growth process. The main competitor to the compressive stress model is the subplantation model proposed by Lifshitz,[31] which is analogous to using ion implantation to increase stress and densifying the film. Another theory by Hofsäss et al. suggests the idea of thermal spike that would involve fast heat up in the area of the impacting ion followed by fast quenching, preventing the displaced atoms to fully relax.[32] The most common models are pictured in Figure 2.5.

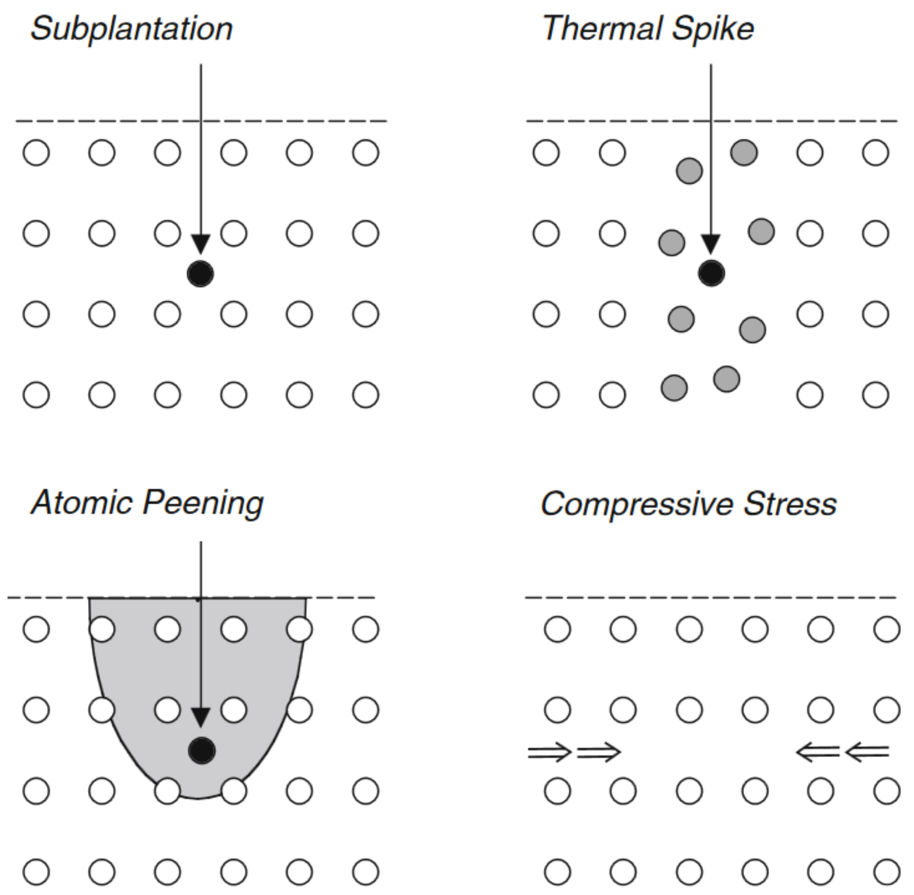

Figure 2.6 - The 4 main models for the formation of ta-C are described. Atomic peening is based on a pressure pulse and relaxation, subplantation is based on sub-surface densification, thermal spike relies on the melting then fast quenching and compressive stress is focused on the biaxial stress in the thin film.[29]

2.2.2.3 Origins of NCG

Recently, nanocrystalline graphite with preferred vertical ordering (NCG) has been studied in depth as it could potentially replace CNTs and graphene in some applications where low temperature growth processes are required.[25, 33-36] NCG consists of nanocrystals of graphite with typical crystal sizes in the tens of nanometers, embedded in a matrix of amorphous carbon. The best NCG quality is almost entirely made of sp^2 bonding, with high ordering in the vertical direction, i.e. perpendicular to the substrate direction as seen in Figure 2.7.

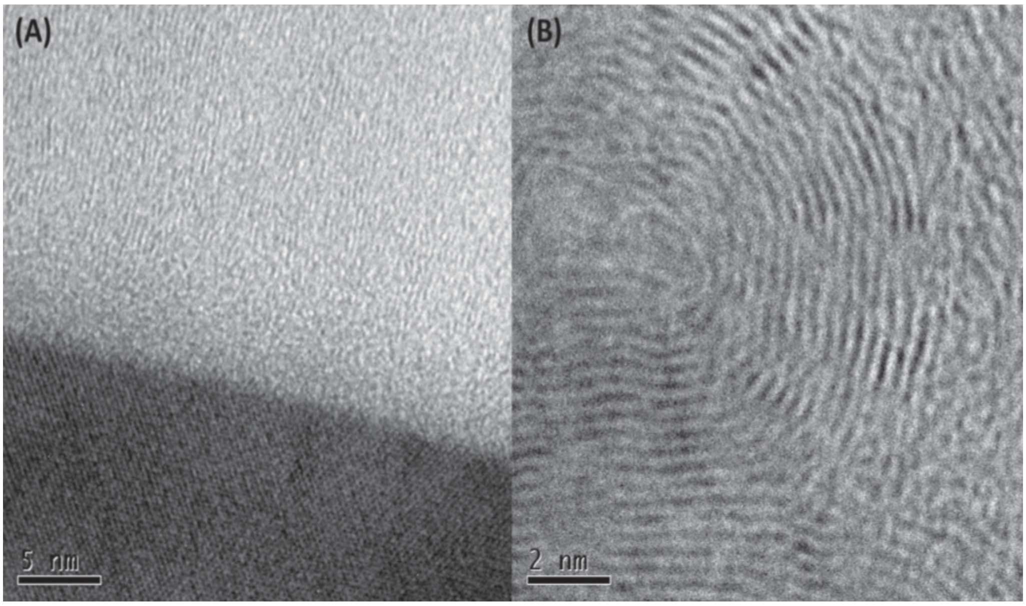

Figure 2.7 - (A) Cross section HRTEM of a NCG film, where the preferred orientation of the graphitic basal plane is perpendicularly aligned with the silicon substrate. (B) Plane view of a NCG film, showing the onion-like rings of the characteristic tubular nanostructure of NCG.[25]

NCG, is commonly obtained by inducing enough intrinsic stress in the film during growth to facilitate the transition from horizontal to vertical ordering. When the compressive stress reaches a sufficient threshold (between 4.5 to 7.5 GPa),[25] the graphite nanocrystals are compelled to re-order themselves with their basal planes in the vertical direction, in order to minimize the Gibbs energy. Figure 2.8 below from Lau et al.[37] shows how the stress threshold is reached and how it is a narrow corridor between low sp^3 low density and high sp^3 high density carbon film.

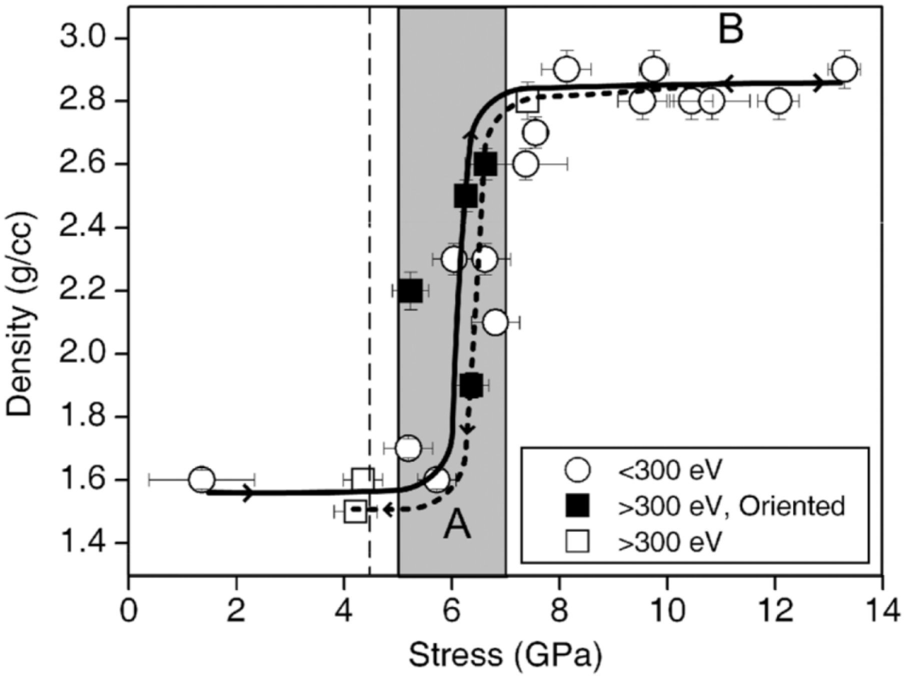

Figure 2.8 - Amorphous carbon film density as a function of compressive stress grown with ion energies ranging from 35 to 1000 eV. The dashed line is the predicted transition stress required to induce a change in nanocrystalline structure while the grey zone is the experimental zone where the change occurs.[37]

It has been shown that ion energy in the plasma during growth is directly related to the compressive stress[38] and Molecular Dynamics simulations confirm that theory where glassy carbon would re-order itself into NCG when subjected to compressive stress as well as sufficient thermal energy.[39] These results have been experimentally verified and exploited to create a NCG patterning in amorphous carbon films, using a laser to induce an amorphous carbon re-ordering to the NCG structure.[40]

2.2.2.4 NCG's properties

NCG's unique properties come from its vertically ordered nanostructure. For instance, it facilitates phonon transport along the basal planes, i.e. in the vertical direction. Such property has been studied and it was shown that the through-film thermal conductivity of NCG was over an order of magnitude higher than its amorphous counterpart (see Figure 2.9).[33]

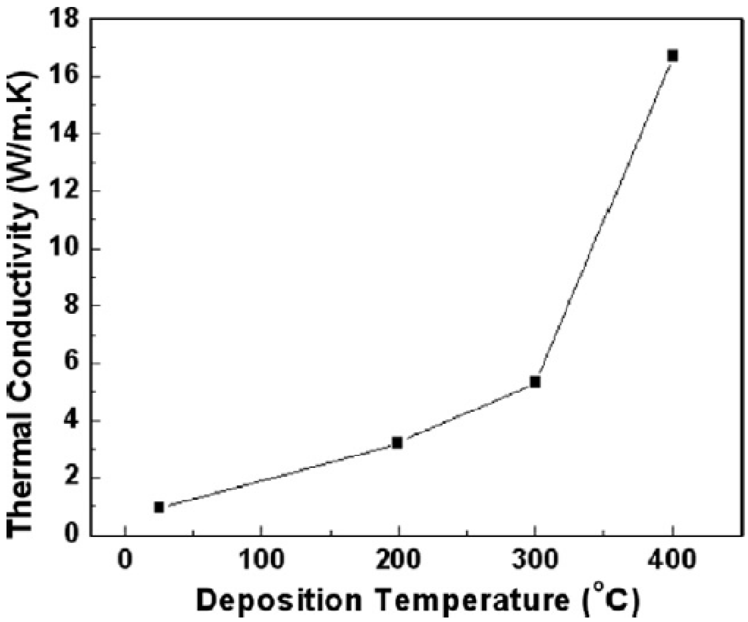

Figure 2.9 - Thermal conductivity of the carbon film depending on the degree of their planar orientation (which is directly linked to the deposition temperature).[33]

Additionally, the intrinsic electrical conductivity of amorphous carbon depends on its sp^2/sp^3 ratio and NCG naturally inherits the electrical properties of high sp^2 content amorphous carbon films with the difference that instead of exhibiting the Schottky contact typical of amorphous carbon, NCG has an Ohmic electrical characteristic in the through-film direction.[37]

2.2.2.5 NCG's potential applications

The capability of obtaining NCG at room temperature and on large areas makes its industrial availability only a step away. Its high thermal conductivity could be used as a directional heat extractor at the nanoscale by directly depositing NCG on the heat generating device. Another application of NCG would be on the growth of interconnects, where laser annealing would create lines of NCG inside an amorphous carbon film.[40] Finally, the ability to switch from high resistivity (high sp^3 amorphous carbon) to low resistivity (NCG) by inducing localized heat spots can lead to the creation of novel carbon based switching memory devices.[41]

2.3 Boron Nitride

Boron Nitride (BN) is a chemical compound formed of both boron and nitrogen in stoichiometric proportions. It is structurally similar to carbon and hence can exist in many different crystalline forms, such as sp^2-bonded hexagonal phase (h-BN), sp^3-bonded cubic phase (c-BN), as well as the less-studied rhombohedral (r-BN), turbostratic (t-BN), wurtzite (w-BN) and amorphous phases. BN is known for its excellent thermal and chemical stability[42], hardness[42], high thermal conductivity[43] and high bandgap of around 6 eV.[44] So far, its thermal and chemical stability are being used as ceramic parts in high temperature systems and most of the research has been focused on h-BN and c-BN due to the potential of the former to be an excellent dielectric substrate for electronics, while the latter exhibits extreme hardness only second to diamond.

2.3.1 Hexagonal Boron Nitride

Hexagonal BN is the most common and stable BN phase. Boron and nitrogen atoms form hexagons sheets stacked on top of each other (as shown in Figure 2.10).

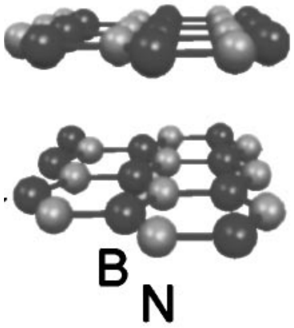

Figure 2.10 - Representation of the hexagonal BN structure with A-B stacking

The hybridization of h-BN is sp^2 and each atom is linked to 3 other neighbors by strong covalent bonding to form hexagon sheets which are held by weak van der Waals forces. It is similar in this fashion to graphite in its atomic arrangement and shares several common properties listed in Table 2.11 below:

	Bulk h-BN	Graphite*
Bond length (nm)	0.145 ∥; 0.334 ⊥[45]	0.142 ∥; 0.335 ⊥
Density (g/cm^3)	2.1[45]	2.09-2.23
Bulk modulus (GPa)	36.5[45]	34
Thermal conductivity (W.m^{-1}.K^{-1})	600 ∥; 30 ⊥[45]	200–2000 ∥ ; 2–800⊥
Bandgap (eV)	5.2[46]	N/A

Figure 2.11 - Comparison of h-BN with graphite. ∥ means in-plane (along the hexagonal sheets) while ⊥ is out-of-plane direction. *the references for graphite's values are given in Figure 2.1

Hexagonal BN has already many applications in today's industry thanks to its high thermal and chemical stability: unlike graphite, it can withstand temperatures up to 1000 degC in an oxidizing environment which enables applications for industrial parts requiring self-lubricating properties as well as chemical inertness. It was primarily used for cosmetics in the first half of the twentieth century before falling out of use due to its high price. Once its production cost became affordable again at the end of the century, it started to be used again for many cosmetics as well as paints and in pencil leads.[47, 48] The weak inter plane Van der Waals force in between each h-BN sheet makes it a lubricant with similar performances as graphite, and is particularly interesting when an electrically insulative material is required. Finally, thanks to its large bandgap of more than 5 eV[44], h-BN can be used to for UV electronics[44, 49, 50]. In addition, it has similar lattice constant as graphene and is extremely smooth which makes h-BN a very promising substrate for graphene electronics and is currently outperforming any other graphene-based device.[51] Thus, it is sometimes called "white graphene" due to its shared properties and compatibility with the monolayer allotrope of carbon.

2.3.2 Cubic Boron Nitride

Cubic BN was first synthesized in 1957 by Wentorf.[52] In a similar fashion as diamond, it was produced by heating and compressing the hexagonal structure of BN to induce a change in crystal structure. The cubic structure of BN exhibits high hardness and is classified as a super hard material along with diamond. Figure 2.12 shows the face-centered cubic (or diamond) structure of c-BN.

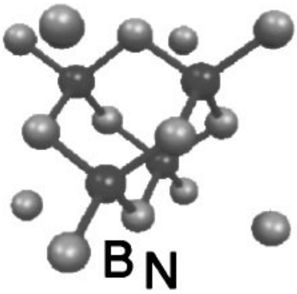

Figure 2.12 - Representation of the cubic BN structure.

In a similar fashion as h-BN which is exclusively of sp^2 bonding, c-BN is solely made of sp^3 bonding which is the reason why this configuration yields a much harder material, in the same way diamond is much harder than graphite. Figure 2.13 below compares the main properties of c-BN with diamond:

	c-BN	Diamond*
Bond length (nm)	0.1565[53]	0.1545
Density (g/cm^3)	3.45[54]	3.515
Bulk modulus (GPa)	400[55]	443
Thermal conductivity ($Wm^{-1}K^{-1}$)	Up to 1300[56]	600-2000
Bandgap (eV)	6.4[57]	5.5

Figure 2.13 - Comparison between c-BN and diamond. *the references for diamond's values are given in Figure 2.1.

Cubic BN is ideal for machining steel[58] and is mostly used as an abrasive when required to work with nickel or iron as it is insoluble in those metals at high temperature (which is not the case of diamond).

2.3.3 Relation between compressive stress and sp^2/sp^3 bonding

In a similar fashion to carbon with diamond, research was driven by the search for an understanding on how to obtain cubic BN. By extending Berman and Simon's[27] results for carbon to BN, a phase diagram between c-BN and h-BN was obtained and its accuracy was experimentally established (at least at temperatures above 500 K). Figure 2.14 is the phase diagram for BN represented by McKenzie[71] which looks very similar to the carbon one.

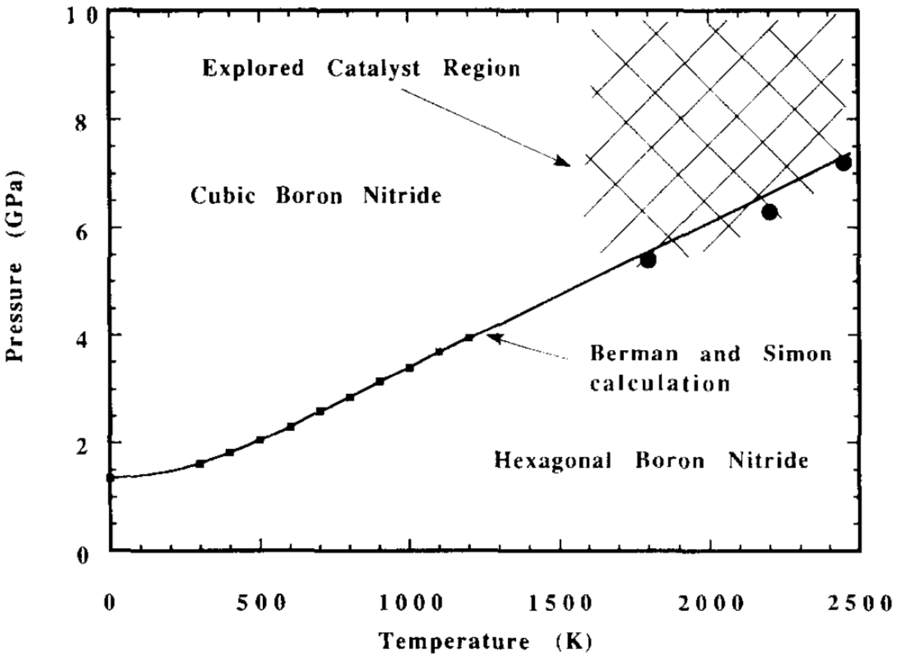

Figure 2.14 - The P-T phase diagram for BN with the region in which c-BN can be obtained with the use of catalysts as well as the Berman and Simon boundary line between the cubic and hexagonal phases.[38]

From that P-T diagram, the same relation between compressive stress and pressure as for carbon was drawn, in order to attempt the growth of cubic BN. In the end, a parallel conclusion was drawn between compressive stress in the film and the ratio between sp^3 bonding (c-BN) and sp^2 (h-BN), where a minimum amount of compressive stress is required to induce a preferential growth of the cubic structure, as shown by McKenzie in Figure 2.15. The Berman-Simon line for the P-T diagram of BN at 500 K display a strict line that needs to be crossed before sp^3 bonding can be formed.

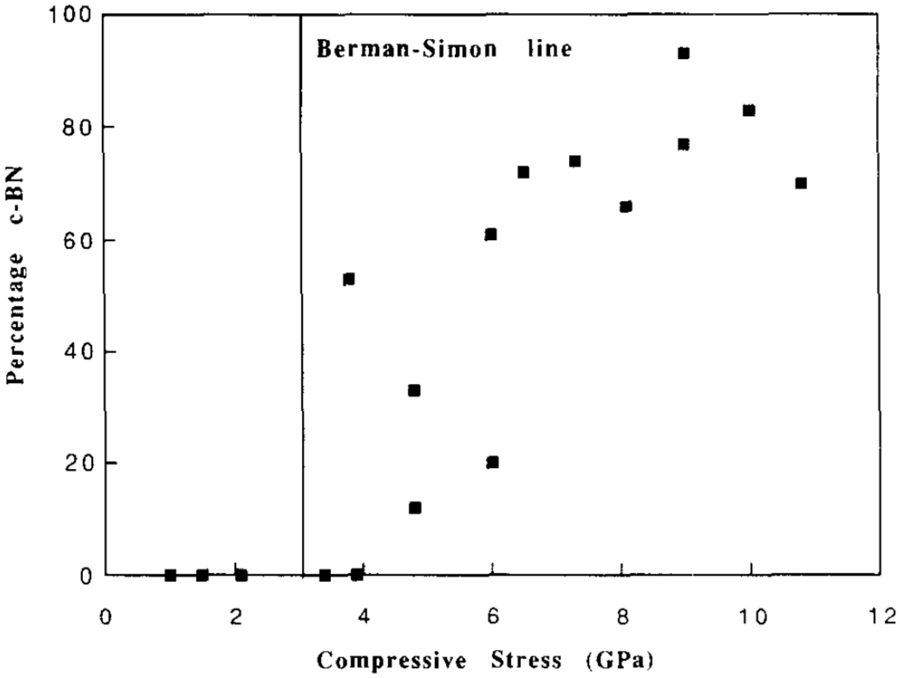

Figure 2.15 - Percentage of cubic BN in the thin film grown at 500 degK, in relation with the compressive stress.

2.3.4 h-BN monolayer and BNNTs

The monolayer version of hexagonal BN has a similar structure to graphene, with the same B-N bond length of 0.145 nm as bulk hexagonal BN. In a similar fashion, those monolayer BN sheets can be rolled onto themselves to form Boron Nitride Nanotubes (BNNTs).[60] Both monolayer h-BN and BNNTs share similarities with their carbon allotrope, such as high thermal conductivity (theoretical computations estimate conductivities of up to 1700-2000 $W.m^{-1}.K^{-1}$)[43] and mechanical strength (elastic modulus slightly lower than CNTs),[61] while remaining electrically insulative[62] as well as chemically inert.[62, 63] Monolayers of h-BN have been particularly interesting for their compatibility with graphene as it is currently the most efficient substrate thanks to its atomically smooth surface, as well as being free of dangling bonds and surface charge traps, yielding electron and hole mobilities of up to 40000 $cm^{-2}.V^{-1}.s^{-1}$ at room temperature,[51] which is already as good as the theoretical limit for graphene on SiO_2. On the other hand, BNNTs show promise in radiation-shielding applications, as the isotope 10 of boron is capable of absorbing neutrons and BNNTs are light weight and have high surface to volume ratio.[64]

2.4 Carbon Nitride

Carbon nitride (CN) materials have attracted a lot of interest since Liu and Cohen formally computed in 1989 that the predicted β-C_3N_4 phase could have properties similar to diamond,[65, 66] such as a high thermal conductivity (theoretical computation suggest a value of 520 $W.m^{-1}.K^{-1}$)[67] and hardness of 422 GPa[66] with is just shy of diamond’s value of 443 GPa. Since then, many research groups have attempted to synthesize the β metastable phase with only very limited results even though some claim to have obtained nanosized crystallites.[68] However, amorphous CN (a-CN) films have been studied extensively as nitrogen implantation in an amorphous carbon matrix proved to substantially improve the hardness (a hardness of up to 60 GPa was reported[69] – in comparison, diamond’s hardness is 100 GPa) as well as the elastic behavior of the film (≈90% recovery).[70, 71]

2.4.1 Graphitic C_3N_4 (g-C_3N_4)

Similar to graphite in its planar structure, g-C_3N_4 has numerous potential applications such as light emitting devices[72] or metal-free visible-light photocatalysis.[73] The later has attracted a lot of attention as it could provide a natural way (solar) of producing hydrogen and oxygen fuel thanks to its water splitting ability.[74] So far, g-C_3N_4 has been solely produced using chemical means by reaction of precursors such as melamine or via thermal CVD.[72] Until now, there has been no successful report of g-C_3N_4 using physical vapor deposition and the focus for physical growth of CN has shifted to other crystalline structures such as β-C_3N_4 and amorphous CN.

2.4.2 Beta C_3N_4 (β-C_3N_4)

Beta carbon nitride (zincblende structure) has remained an elusive material from its inception in 1989[75] until the early 2000s when finally, some undeniable proof of the β-

C_3N_4 structure was characterized by TEM.[68, 76] So far, obtaining the beta structure involves a mechanochemical method which is highly impractical for any applications other than characterizing the material itself.

2.4.3 Amorphous carbon nitride (a-CN or CN_x)

Amorphous CN_x (or a-CN) was first investigated as a by-product of attempts to get the β-C_3N_4 phase. Its structure is similar to a-BN or a-C and it presents a mixture of sp^2 and sp^3 hybridization. Some of its properties such as high hardness[77] have been used in magnetic hard disk drives as a protective layer.[78] CN_x can be divided in several sub-structural families: amorphous, graphite like (alternatively called graphitic-like) and fullerene-like structures. Hellgren et al.[79-81] created and refined a phase diagram for amorphous carbon nitride, predicting the CN_x structure depending on the temperature and nitrogen concentration in the film (Figure 2.16). Only films with amorphous structure could be obtained for deposition temperatures below 200 degC, while higher temperatures would yield graphitic-like or fullerene-like films.

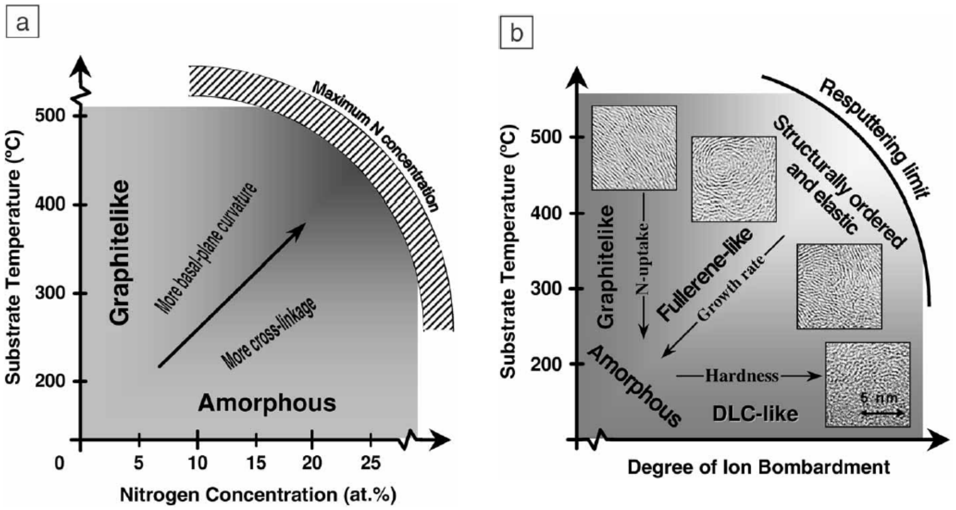

Figure 2.16 - Phase diagram of CN_x for varying deposition temperature and: nitrogen film concentration (left) or degree of ion bombardment (right) for reactive DC sputtering deposition techniques.[81]

2.5 Main parameter affecting structuring: Stress in thin films

An overview explaining what stress in thin films is, as well as its origins is described in the section below. Indeed, controlling the growth and crystallinity of materials is highly dependent on understanding the stress applied to the thin film as it is one of the main parameters affecting the crystalline structure, and will influence the result, going from growth rate to film delamination.

2.5.1 Introduction

Growing thin films on substrates will always be imperfect as both substrate and thin film have different properties such as thermal expansion coefficient or crystal lattice constant. The former will be the cause for thin film peel off when heating up or cooling down the substrate, as both (or more) layers need to accommodate each other's change in size, and thus can cause mechanical failure. The latter is called lattice mismatch and depending on how large the mismatch is, it can create large stress buildup while growing the film, causing delamination. It is crucial to be able to understand and control the stress in the film as it is a way to induce in-situ changes in the thin film crystallinity during growth or even after during annealing as will be explained later.

2.5.2 Types of stress

Figure 2.17 below shows the 3 different conditions a thin film can be in: no stress, compressive stress and tensile stress. The stress in a thin film/substrate pair is due to constraints applied from one to the other mainly due to the reasons explained above. This means that if there is compressive stress applied from the substrate to the thin film, therefore there is tensile stress applied on the substrate from the thin film. However, as the substrate is typically much thicker than the thin film which means the substrate will only carry small and inelastic deformations. As the stress is inversely proportional to the layer thickness (as will be explained later), any mention of stress will indirectly refer to the stress applied on the thin film even when it is not specified. From Figure 2.17, it can be easily understood that the radius of curvature can provide information about the stress, where a radius of infinity would be an unstressed film, while a negative radius would yield a tensile stress and a positive one would be compressive.

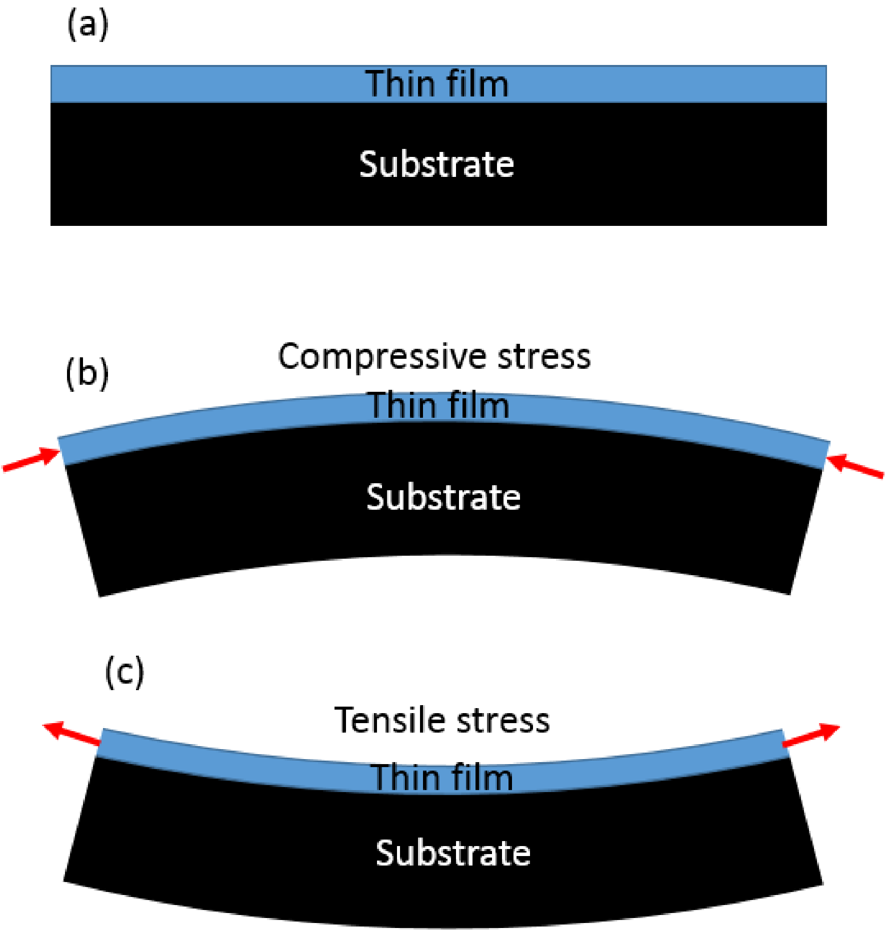

Figure 2.17 - (a) Thin film and substrate without any stress in between. (b) Compressive stress induced by the substrate compressing the thin film. (c) Tensile stress induced by the substrate, applying a stretching force to the film. The red arrows indicate the compressive and stretching forces applied to the thin film.

2.5.3 Stoney's equation

Stoney published in 1909 a paper where he derived the formula describing the stress of a thin layer on a steel strip according to its radius of curvature.[97] The equation (2.2) looks as follows:

$$\sigma_f t_f = \frac{E_s h^2}{6\left(1 - v_s\right) R} \qquad (2.2)$$

The stress in the thin film is given by σ_f , with t_f being the thin film thickness, E_s is the substrate Young's modulus, h is the substrate thickness, v_s is the substrate Poisson's ratio and R is the radius of curvature of the sample (substrate with thin film on top). Several things can be deduced from this equation. First, the higher the radius of curvature, the smaller the thin film stress (assuming all other parameters are kept constant). This makes sense with the fact that the greater R is, the flatter the substrate, with a perfectly flat substrate being equivalent to an infinite radius of curvature, hence a stress of 0. Secondly, for the same radius of curvature, a thinner thin film would yield a greater stress. Thirdly, Stoney's equation relies solely on the substrate properties, where the Poisson ratio and Young's modulus of the thin film deposited do not matter. Unfortunately, Stoney's equation was originally designed for uniaxial stress along only one direction and for elastic isotropic materials. In the case of thin film grown on Si wafers it gets slightly more complex due to the fact the single crystal silicon wafers are elastically anisotropic, depending on the crystal orientation. For Si(001) wafers, which are the most used wafers in research, an updated formula has been derived to take into account the anisotropic behavior:[98]

$$\sigma_f t_f = \frac{h^2}{6\left(s_{11}^{Si} + s_{12}^{Si}\right) R} \qquad (2.3)$$

The 2 coefficients s_{11}^{Si} and s_{12}^{Si} are called the compliance tensor of silicon and the whole term $\frac{1}{s_{11}^{Si}+s_{12}^{Si}}$ is called the biaxial modulus M of Si(001). In the case of Si(001), $M=1.803.10^{11}$ Pa.

The two formulas above are assuming a zero curvature before the film growth which is not the case in reality and equation 2.3 should be amended to equation 2.4 as follows:

$$\sigma_f t_f=\frac{h^2}{6\left(s_{11}^{Si}+s_{12}^{Si}\right)}\left(\frac{1}{R_{after}}-\frac{1}{R_{before}}\right) \qquad (2.4)$$

The radius of curvature R_{before} is the radius before thin film growth, while R_{after} is the radius after growth. As $R_{before}>R_{after}$ (due to the fact that before growth, the substrate is supposed to be almost flat, i.e. it has a large radius of curvature), $\frac{1}{R_{after}}$ will always be greater than $\frac{1}{R_{before}}$ which indicates that a positive value will indicate compressive stress condition while the negative value would mean the stress is tensile. Also, as mentioned before, a flat unstressed substrate would tend to have a radius of curvature tending towards infinity, which means that $\frac{1}{R_{before}}\overset{\rightarrow}{\infty}0$ so equation 2.4 can be simplified to:

$$\sigma_f t_f=\frac{h^2}{6\left(s_{11}^{Si}+s_{12}^{Si}\right)}\left(\frac{1}{R_{after}}\right) \qquad (2.5)$$

Equation 2.5 is exactly equation 2.4 when taking the assumption that the radius of curvature before the film growth is much larger than the radius of curvature of the substrate after thin film growth. Typically, this assumption is valid as R_{before} is in the hundreds of meters while R_{after} is below 1 meter.

2.5.4 Growth induced compressive stress

Biaxial compressive stress during growth can be attained during thin film growth by the impact of incident atoms or ions. McKenzie et al. derived a formula correlating compressive stress with ion energy as per equation 2.6:[59]

$$\sigma \propto \frac{\sqrt{E}}{\frac{R}{j}+kE^{\frac{5}{3}}} \qquad (2.6)$$

The coefficient $k=0.016\rho E_0^{-5/3}$, E is the ion energy, j is the ion flux, and ρ , E_0 and R are parameters related to the thin film material. When plotting the curve for the arbitrary values of $\frac{R}{j}=5$ and $k=0.1$, we obtain the result shown in Figure 2.18:

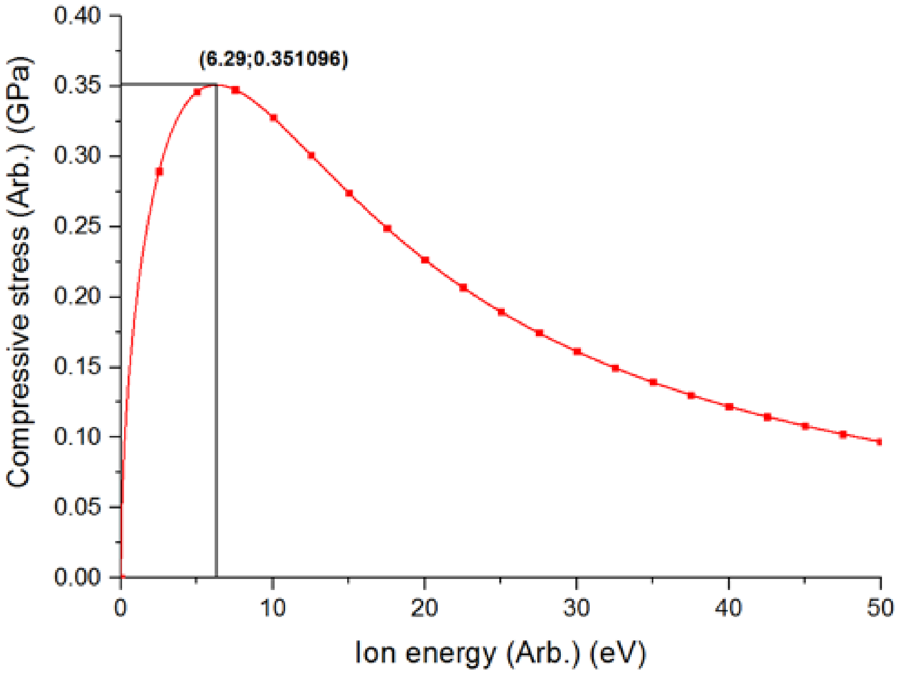

Figure 2.18 - Plot of equation 2.5 with $\frac{R}{j}=5$ and $k=0.1$, The curve shows a maximum at an energy of 6.29 eV.

The curve shape has several implications on the stress applied on the film according to the growth conditions and more particularly the ion energy. The first part of the curve shows a rapid rise in stress with increasing ion energy until it reaches a maximum (in Figure 2.18 this maximum is reached for an ion energy of 6.29 eV). Once this maximum is reached, the stress starts decreasing with greater ion energies, until it will eventually go back to zero (not shown in Figure 2.18). This can be explained by the ions penetrating the subsurface of the thin film, which induces local compression, while higher ion energies will cause the incident ions to sputter away the film, hence creating a condition for stress relaxation. Stress tuning during growth is an important factor to control the nanocrystal formation in thin films as certain material phases can only occur at specific pressures and temperatures, and stress is a way to locally induce pressure on nanocrystals. As such, compressive stress will be a central player in the growth process as explained later in this chapter as well as in this work.

2.6 B, C, N compound PVD growth techniques

C, BN and CN films have been produced using many different growth techniques falling under two main methods which are the chemical growth involving chemical reactions between reactants, while the other method uses plasmas to obtain a material. The chemical means of deposition have the advantage of yielding high crystallinity with few defects and an easy control of the film growth. However, the lack of energetic deposition favors the lowest density phase as per the Ostwald-Wolmer rule, which is generally the graphitic phase (graphene, h-BN, g-C_3N_4 and g-BC_xN), leaving the denser cubic phases out of reach for this kind of process. Nevertheless, c-BN and diamond was successfully grown[99, 100] thanks to Plasma-Enhanced CVD (PECVD) that overcame this energy issue by introducing plasmas into the reaction. However, CVD growth techniques require high temperatures to induce the chemical reaction and are unsuitable for the growth of thick and/or amorphous materials, so far limiting the scope of study for B, C and N to only pure 2D crystalline phases. On the other hand, Physical Vapor Deposition (PVD) uses energetic plasmas to grow films. Relying on energetic plasmas instead of heat induced chemical reactions allows the growth of denser materials with improved adhesion and mechanical properties. Here, we focus only on PVD growth methods as the objective is to study thin films instead of 2D materials. The main PVD systems reported in the literature to grow B, C and N compounds are listed below.

2.6.1 Pulsed Laser Deposition (PLD)

PLD uses a high-power laser ablating a solid target to create plasma. This method yields good results for getting c-BN[101] from the ablation of a h-BN target as well as C and CN_x films from a graphite target in either nitrogen gas[102] or vacuum.[103] BCN thin film were also grown using PLD as well, using various laser power on a boron carbide

(B_4C) target in nitrogen gas.[104] The target ablation by a high-power laser provides high plasma energies and yields dense films, which is an advantage when aiming for materials with high hardness. However, the downside to this method is the quantity of micro particles directly sputtered from the target onto the substrate and the difficulty to get an even film over large areas.

2.6.2 Sputtering

The 2 main sputtering systems used are Direct Current Magnetron Sputtering (DCMS) and RF Sputtering. Reactive DCMS of a graphite target in nitrogen has been widely used to study various a-C[105] and CN_x[70] films but only marginally used for BN growth as BN is insulative and DCMS requires a conductive target. The only exception is the use of a heated boron target to several hundred degrees to make it conductive.[106, 107] In order to overcome the insulative property of BN, RF sputtering is used.[108, 109] The simple setup of dual sputtering systems even enabled the concurrent growth of BN and CN at the same time in order to obtain BCN compounds,[95, 110, 111] but other methods such as RF sputtering of a BN target in acetylene[112] or sputtering of a B_4C target in nitrogen is possible,[93] though they offer limited flexibility in controlling the stoichiometry between carbon, boron and nitrogen. Both sputtering techniques have the advantage of producing clean and even films. Yet, the low energies involved in the sputtering process leads to a low ionization rate of the sputtered species, which in turn limits the density of the deposited films.

2.6.3 Ion Implantation

The main challenge when growing a compound material is to get the proper stoichiometry, especially for nitrogen containing films where nitrogen ions will preferentially recombine into the most stable N_2 phase instead of bonding with other species. Ion implantation systems such as Electron Cyclotron Resonance (ECR) or Ion beam source allows greater maneuverability with the nitrogen contents in the film as one can directly implant N+ ions. It is usually used in a hybrid system, complementing another PVD source such as PLD or DCMS. This configuration has been used to grow CN_x films,[113-115] as well as BN films[116] and more recently for BCN films[117] where the ternary compound nature of BCN makes the control of element stoichiometry more difficult. With such method, the nitrogen concentration in CN films was able to reach 50% and above,[118] while a maximum of only 35 at.% can be reached without ion implantation.[79]

2.6.4 Filtered Cathodic Vacuum Arc (FCVA)

As FCVA is one of the most energetic way of depositing films, it became a very successful method to grow DLC with a sp^3 ratio in the film of over 80%[119] and hence was a natural choice for hard CN films.[120] However, a vacuum arc alone makes the increase of nitrogen in the films difficult and it is usually used in conjunction with a nitrogen ion source. Similarly to CN, the growth of BCN via FCVA is possible by using a B_4C target in nitrogen gas.[121] However, it has the same downside where the nitrogen content cannot be properly controlled. Finally, when it comes to BN films, it is impossible to use a pure BN target as FCVA requires an electrically conductive target. Nonetheless, one instance of FCVA produced BN films exists so far, using a modified FCVA setup where a special boron target would be heated up to 1000 degC.[122] Even though this setup can virtually reach a 100% c-BN phase, the difficulty to control the nitrogen doping remains a continued issue.

2.6.5 High Power Impulse Magnetron Sputtering (HiPIMS)

In the recent years, a novel PVD technique was developed that would combine the versatility of DCMS with the high ion energies of FCVA. HiPIMS is a fairly new physical deposition system first reported in 1999.[123] Its principle of functioning is based on the standard direct current magnetron sputtering for the plasma source, with the main difference being the power source, which is based on a pulsed current pattern instead of constant source. The pulses can vary from a few microseconds to a few hundreds, with the pulse frequency usually below 1 KHz. Thanks to its easy plasma tuning, HiPIMS can generate a huge variety of materials with different crystalline structures. However, there has been no previous attempt to produce BN or CN thin films with HiPIMS even though the high plasma density it generates makes it the ideal tool for the job. As such, it will be the main equipment for the growth of materials in this work and will be discussed in more details in a separate chapter.

2.7 Conclusion

This chapter serves a dual purpose. Firstly, it helps to provide an overview of the research conducted on carbon, boron and nitrogen based thin films, as well as the various physical growth methods used to produce the materials. This is required for the reader to get a better understanding of the work achieve in this thesis. Lastly, it summarizes the main and most important literature research work on which this whole thesis was built upon. In particular, the research on boron nitride and carbon nitride was key to understanding better how each material is grown (especially the methods based on magnetron sputtering), as well as what growth parameters impact the growth process most (DC bias, gas ratio and magnetron power). In addition, the literature review on HiPIMS proved crucial to understand better what limitations were to be expected from it, and what advantages can be exploited to obtain the intended results. This is why the next chapter will be dedicated to the HiPIMS system used for this work, where we will explain in more details how it works and how it has been modified, upgraded and optimized for the growth of boron nitride and carbon nitride.

2.8 References

1. J. Moore, C. Stanitski and P. Jurs, *Principles of Chemistry: The Molecular Science*, Cengage Learning, 2009.
2. N. Deprez and D. S. McLachlan, *J. Phys. D: Appl. Phys.*, 1988, **21**, 101.
3. A. T. Collins, *Philosophical Transactions of the Royal Society of London. Series A: Physical and Engineering Sciences*, 1993, **342**, 233-244.
4. S. Iijima, *Nature*, 1991, **354**, 56-58.
5. A. K. Geim and K. S. Novoselov, *Nat Mater*, 2007, **6**, 183-191.
6. E. Pop, D. Mann, Q. Wang, K. Goodson and H. Dai, *Nano Lett.*, 2006, **6**, 96-100.
7. M. Ouyang, J. L. Huang, C. L. Cheung and C. M. Lieber, *Science*, 2001, **292**, 702-705.
8. C. Lee, X. Wei, J. W. Kysar and J. Hone, *Science*, 2008, **321**, 385-388.
9. mindat.org, Minerological information about Diamond., 2016.
10. P. Delhaes, *Graphite and Precursors (World of Carbon)*, CRC Press.
11. mindat.org, Minerological information about Graphite., 2016.
12. D. R. Cooper, B. D'Anjou, N. Ghattamaneni, B. Harack, M. Hilke, A. Horth, N. Majlis, M. Massicotte, L. Vandsburger, E. Whiteway and V. Yu, *ISRN Condensed Matter Physics*, 2012, **2012**, 1-56.
13. K. W. R. Gilkes, P. H. Gaskell and J. Yuan, *J. Non-Cryst. Solids*, 1993, **164**, 1107-1110.
14. S. Sakurai, M. Inaguma, D. N. Futaba, M. Yumura and K. Hata, *Small*, 2013, **9**, 3584-3592.
15. M. Iwaki, *Surf. Coat. Technol.*, 2002, **158–159**, 377-381.
16. C. Kittel, *Introduction to Solid State Physics*, Wiley, 8th Edition edn., 2004.
17. B. T. Kelly, *Physics of graphite*, Applied Science, 1981.
18. M. Popov, M. Kyotani, R. J. Nemanich and Y. Koga, *Physical Review B*, 2002, **65**, 033408.
19. E. B. Halac and E. Burgos, *Physical Review B*, 2009, **80**, 045426.
20. Y. Matsuda, J. Tahir-Kheli and W. A. Goddard, *The Journal of Physical Chemistry Letters*, 2010, **1**, 2946-2950.
21. V. Stolojan, P. Moreau, M. J. Goringe and S. R. P. Silva, 2005, **107**, 307-310.
22. L. Wei, P. K. Kuo, R. L. Thomas, T. R. Anthony and W. F. Banholzer, *Phys. Rev. Lett.*, 1993, **70**, 3764-3767.
23. R. L. Powell and G. E. Childs, *American Institute of Physics Handbook*, 1972.
24. S. Sinha, S. Barjami, G. Iannacchione, A. Schwab and G. Muench, *J. Nanopart. Res.*, 2005, **7**, 651-657.
25. M. Shakerzadeh, G. C. Loh, N. Xu, W. L. Chow, C. W. Tan, C. Lu, R. C. C. Yap, D. Tan, S. H. Tsang, E. H. T. Teo and B. K. Tay, *Adv. Mater.*, 2012, **24**, 4112-4123.
26. D. R. McKenzie, D. Muller and B. A. Pailthorpe, *Phys. Rev. Lett.*, 1991, **67**, 773-776.
27. R. Berman and S. F. Simon, *Zeitschrift für Elektrochemie, Berichte der Bunsengesellschaft für physikalische Chemie*, 1955, **59**, 333-338.
28. L. D. Landau and E. M. Lifshitz, *Theory of Elasticity*, Pergamon, London, 1959.
29. N. A. Marks, in *Computer-Based Modeling of Novel Carbon Systems and Their Properties: Beyond Nanotubes*, eds. L. Colombo and A. Fasolino, Springer Netherlands, Dordrecht, 2010, DOI: 10.1007/978-1-4020-9718-8_5, pp. 129-169.
30. D. R. McKenzie, D. A. Muller, E. Kravtchinskaia, D. Segal, D. J. H. Cockayne, G. Amaratunga and R. Silva, *Thin Solid Films*, 1991, **206**, 198-203.
31. Y. Lifshitz, S. R. Kasi and J. W. Rabalais, *Phys. Rev. Lett.*, 1989, **62**, 1290-1293.
32. H. Hofsäss, H. Feldermann, R. Merk, M. Sebastian and C. Ronning, *Appl. Phys. A*, 1998, **66**, 153-181.
33. M. Shakerzadeh, M. K. Samani, N. Khosravian, E. H. T. Teo, M. Bosman and B. K. Tay, *Carbon*, 2012, **50**, 1428-1431.

34. M. Shakerzadeh, E. H. T. Teo, A. Sorkin, M. Bosman, B. K. Tay and H. Su, *Carbon*, 2011, **49**, 1733-1744.
35. M. Shakerzadeh, E. H. T. Teo and B. K. Tay, *Thickness dependency of field emission in amorphous and nanostructured carbon thin films*, 2012.
36. C. W. Tan, S. Maziar, E. H. T. Teo and B. K. Tay, *Diamond Relat. Mater.*, 2011, **20**, 290-293.
37. D. W. M. Lau, D. G. McCulloch, M. B. Taylor, J. G. Partridge, D. R. McKenzie, N. A. Marks, E. H. T. Teo and B. K. Tay, *Phys. Rev. Lett.*, 2008, **100**, 176101.
38. D. R. McKenzie, *Journal of Vacuum Science & Technology B: Microelectronics and Nanometer Structures*, 1993, **11**, 1928.
39. D. G. McCulloch, N. A. Marks, D. R. McKenzie and S. Prawer, *Nuclear Instruments and Methods in Physics Research Section B: Beam Interactions with Materials and Atoms*, 1995, **106**, 545-549.
40. M. Shakerzadeh, N. Xu, M. Bosman, B. K. Tay, X. Wang, E. H. T. Teo, H. Zheng and H. Yu, *Carbon*, 2011, **49**, 1018-1024.
41. Y. Chai, Y. Wu, K. Takei, H.-Y. Chen, S. Yu, P. C. H. Chan, A. Javey and H. S. P. Wong, *IEEE Transactions on Electron Devices*, 2011, **58**, 3933-3939.
42. P. Beiss, R. Ruthardt and H. Warlimont, 2002.
43. T. Ouyang, Y. Chen, Y. Xie, K. Yang, Z. Bao and J. Zhong, *Nanotechnology*, 2010, **21**, 245701.
44. K. Watanabe, T. Taniguchi and H. Kanda, *Nat Mater*, 2004, **3**, 404-409.
45. S. L. Rumyantsev, M. E. Levinshtein, A. D. Jackson, S. N. Mohammmad, G. L. Harris, M. G. Spencer and M. S. Shur, *Properties of Advanced Semiconductor Materials: GaN, AIN, InN, BN, SiC, SiGe*, Wiley, New York, 2001.
46. D. M. Hoffman, G. L. Doll and P. C. Eklund, *Physical Review B*, 1984, **30**, 6051-6056.
47. J. Greim and K. A. Schwetz, 2006, DOI: 10.1002/14356007.a04_295.pub2.
48. G. Deutsche Keramische, *Ceramic forum international : CFI : Berichte der DKG.*, 1980.
49. R. Gao, L. Yin, C. Wang, Y. Qi, N. Lun, L. Zhang, Y.-X. Liu, L. Kang and X. Wang, *The Journal of Physical Chemistry C*, 2009, **113**, 15160-15165.
50. R. Sevak Singh, R. Yingjie Tay, W. Leong Chow, S. Hon Tsang, G. Mallick and E. H. Tong Teo, *Appl. Phys. Lett.*, 2014, **104**, -.
51. C. R. Dean, A. F. Young, MericI, LeeC, WangL, SorgenfreiS, WatanabeK, TaniguchiT, KimP, K. L. Shepard and HoneJ, *Nat Nano*, 2010, **5**, 722-726.
52. R. H. Wentorf, *The Journal of Chemical Physics*, 1957, **26**, 956-956.
53. R. C. DeVries, *Cubic Boron Nitride: Handbook of Properties*, General Electric Company, 1972.
54. T. Sōma, A. Sawaoka and S. Saito, *Mater. Res. Bull.*, 1974, **9**, 755-762.
55. M. Grimsditch, E. S. Zouboulis and A. Polian, *J. Appl. Phys.*, 1994, **76**, 832-834.
56. G. A. Slack, *J. Phys. Chem. Solids*, 1973, **34**, 321-335.
57. R. M. Chrenko, *Solid State Commun.*, 1974, **14**, 511-515.
58. R. H. Todd, D. K. Allen and L. Alting, *Manufacturing Processes Reference Guide*, Industrial Press Inc., 1994.
59. D. R. McKenzie, W. D. McFall, W. G. Sainty, C. A. Davis and R. E. Collins, *Diamond Relat. Mater.*, 1993, **2**, 970-976.
60. D. Golberg, Y. Bando, C. C. Tang and C. Y. Zhi, *Adv. Mater.*, 2007, **19**, 2413-2432.
61. T. Dumitrică, H. F. Bettinger, G. E. Scuseria and B. I. Yakobson, *Physical Review B*, 2003, **68**, 085412.
62. X. Blase, A. Rubio, S. G. Louie and M. L. Cohen, *EPL (Europhysics Letters)*, 1994, **28**, 335.
63. W.-Q. Han, W. Mickelson, J. Cumings and A. Zettl, *Appl. Phys. Lett.*, 2002, **81**, 1110-1112.
64. J. Yu, Y. Chen, R. G. Elliman and M. Petravic, *Adv. Mater.*, 2006, **18**, 2157-2160.
65. A. Y. Liu and M. L. Cohen, *Physical Review B*, 1990, **41**, 10727-10734.
66. C.-M. Sung and M. Sung, *Mater. Chem. Phys.*, 1996, **43**, 1-18.

67. D. T. Morelli and J. P. Heremans, *Appl. Phys. Lett.*, 2002, **81**, 5126-5128.
68. L.-W. Yin, M.-S. Li, G. Luo, J.-L. Sui and J.-M. Wang, *Chem. Phys. Lett.*, 2003, **369**, 483-489.
69. H. Sjöström, S. Stafström, M. Boman and J. E. Sundgren, *Phys. Rev. Lett.*, 1995, **75**, 1336-1339.
70. E. Broitman, N. Hellgren, O. Wänstrand, M. P. Johansson, T. Berlind, H. Sjöström, J. E. Sundgren, M. Larsson and L. Hultman, *Wear*, 2001, **248**, 55-64.
71. D. Li, Y. W. Chung, M. S. Wong and W. D. Sproul, *J. Appl. Phys.*, 1993, **74**, 219-223.
72. G. Dong, Y. Zhang, Q. Pan and J. Qiu, *Journal of Photochemistry and Photobiology C: Photochemistry Reviews*, 2014, **20**, 33-50.
73. Y. Zheng, J. Liu, J. Liang, M. Jaroniec and S. Z. Qiao, *Energy & Environmental Science*, 2012, **5**, 6717-6731.
74. X. Wang, K. Maeda, A. Thomas, K. Takanabe, G. Xin, J. M. Carlsson, K. Domen and M. Antonietti, *Nat Mater*, 2009, **8**, 76-80.
75. A. Y. Liu and M. L. Cohen, *Science*, 1989, **245**, 841-842.
76. L. W. Yin, Y. Bando, M. S. Li, Y. X. Liu and Y. X. Qi, *Adv. Mater.*, 2003, **15**, 1840-1844.
77. D. Li, X. Chu, S. C. Cheng, X. W. Lin, V. P. Dravid, Y. W. Chung, M. S. Wong and W. D. Sproul, *Appl. Phys. Lett.*, 1995, **67**, 203-205.
78. E. G. Wang, *Prog. Mater Sci.*, 1997, **41**, 241-298.
79. N. Hellgren, M. P. Johansson, E. Broitman, L. Hultman and J.-E. Sundgren, *Physical Review B*, 1999, **59**, 5162-5169.
80. N. Hellgren, K. Macák, E. Broitman, M. P. Johansson, L. Hultman and J.-E. Sundgren, *J. Appl. Phys.*, 2000, **88**, 524-532.
81. L. Hultman, J. Neidhardt, N. Hellgren, H. Sjöström and J.-E. Sundgren, *MRS Bull.*, 2003, **28**, 194-202.
82. A. R. Badzian, *Mater. Res. Bull.*, 1981, **16**, 1385-1393.
83. E. Knittle, R. B. Kaner, R. Jeanloz and M. L. Cohen, *Physical Review B*, 1995, **51**, 12149-12156.
84. S. Nakano, M. Akaishi, T. Sasaki and S. Yamaoka, *Chem. Mater.*, 1994, **6**, 2246-2251.
85. T. Komatsu, M. Nomura, Y. Kakudate and S. Fujiwara, *J. Mater. Chem.*, 1996, **6**, 1799-1803.
86. V. L. Solozhenko, D. Andrault, G. Fiquet, M. Mezouar and D. C. Rubie, *Appl. Phys. Lett.*, 2001, **78**, 1385-1387.
87. V. L. Solozhenko, S. N. Dub and N. V. Novikov, *Diamond Relat. Mater.*, 2001, **10**, 2228-2231.
88. C. Y. Zhi, J. D. Guo, X. D. Bai and E. G. Wang, *J. Appl. Phys.*, 2002, **91**, 5325-5333.
89. S. Azevedo and R. d. Paiva, *EPL (Europhysics Letters)*, 2006, **75**, 126.
90. P. Sutter, R. Cortes, J. Lahiri and E. Sutter, *Nano Lett.*, 2012, **12**, 4869-4874.
91. G. H. Han, J. A. Rodríguez-Manzo, C.-W. Lee, N. J. Kybert, M. B. Lerner, Z. J. Qi, E. N. Dattoli, A. M. Rappe, M. Drndic and A. T. C. Johnson, *ACS Nano*, 2013, **7**, 10129-10138.
92. X. Wei, M.-S. Wang, Y. Bando and D. Golberg, *ACS Nano*, 2011, **5**, 2916-2922.
93. A. Prakash and K. B. Sundaram, *ECS Journal of Solid State Science and Technology*, 2015, **4**, N25-N29.
94. D. H. Kim, E. Byon, S. Lee, J.-K. Kim and H. Ruh, *Thin Solid Films*, 2004, **447–448**, 192-196.
95. A. Prakash, University of Central Florida, 2016.
96. T. Tavsanoglu, M. Jeandin and O. Addemir, *Surf. Eng.*, 2016, DOI: 10.1080/02670844.2016.1143197, 1-6.
97. G. G. Stoney, *Proceedings of the Royal Society of London. Series A*, 1909, **82**, 172-175.
98. G. C. A. M. Janssen, M. M. Abdalla, F. van Keulen, B. R. Pujada and B. van Venrooy, *Thin Solid Films*, 2009, **517**, 1858-1867.
99. P. Thevenin, A. Soltani and A. Bath, 2001.

100. Y. A. Mankelevich and P. W. May, *Diamond Relat. Mater.*, 2008, **17**, 1021-1028.
101. F. Qian, V. Nagabushnam and R. K. Singh, *Appl. Phys. Lett.*, 1993, **63**, 317-319.
102. Y. K. Yap, S. Kida, T. Aoyama, Y. Mori and T. Sasaki, *Appl. Phys. Lett.*, 1998, **73**, 915-917.
103. D. L. Pappas, K. L. Saenger, J. Bruley, W. Krakow, J. J. Cuomo, T. Gu and R. W. Collins, *J. Appl. Phys.*, 1992, **71**, 5675-5684.
104. C. B. Wang, J. L. Xiao, Q. Shen and L. M. Zhang, *Thin Solid Films*, 2016, **603**, 323-327.
105. N. A. Sánchez, C. Rincón, G. Zambrano, H. Galindo and P. Prieto, *Thin Solid Films*, 2000, **373**, 247-250.
106. A. Schütze, K. Bewilogua, H. Lüthje, S. Kouptsidis and S. Jäger, *Surf. Coat. Technol.*, 1995, **74-75**, 717-722.
107. J. Hahn, M. Friedrich, R. Pintaske, M. Schaller, N. Kahl, D. R. T. Zahn and F. Richter, *Diamond Relat. Mater.*, 1996, **5**, 1103-1112.
108. M. Mieno and T. Yoshida, *Japanese Journal of Applied Physics*, 1990, **29**, L1175-L1177.
109. J. J. Cuomo, P. A. Leary, D. Yu, W. Reuter and M. Frisch, *Journal of Vacuum Science & Technology*, 1979, **16**, 299-302.
110. A. Prakash and K. B. Sundaram, *Diamond Relat. Mater.*, 2016, 80, 254
111. S. C. Chien, S. Chattopadhyay, L. C. Chen, S. T. Lin and K. H. Chen, *Diamond Relat. Mater.*, 2003, **12**, 1463-1471.
112. S. Ulrich, H. Ehrhardt, T. Theel, J. Schwan, S. Westermeyr, M. Scheib, P. Becker, H. Oechsner, G. Dollinger and A. Bergmaier, *Diamond Relat. Mater.*, 1998, **7**, 839-844.
113. F. Fujimoto and K. Ogata, *Japanese Journal of Applied Physics*, 1993, **32**, L420-L423.
114. M. Kohzaki, A. Matsumuro, T. Hayashi, M. Muramatsu and K. Yamaguchi, *Thin Solid Films*, 1997, **308–309**, 239-244.
115. A. Bousetta, M. Lu, A. Bensaoula and A. Schultz, *Appl. Phys. Lett.*, 1994, **65**, 696-698.
116. D. L. Medlin, T. A. Friedmann, P. B. Mirkarimi, P. Rez, M. J. Mills and K. F. McCarty, *J. Appl. Phys.*, 1994, **76**, 295-303.
117. H. Yasui, Y. Hirose, K. Awazu and M. Iwaki, *Colloids and Surfaces B: Biointerfaces*, 2000, **19**, 291-295.
118. K. Ogata, J. F. D. Chubaci and F. Fujimoto, *J. Appl. Phys.*, 1994, **76**, 3791-3796.
119. S. Xu, D. Flynn, B. K. Tay, S. Prawer, K. W. Nugent, S. R. P. Silva, Y. Lifshitz and W. I. Milne, *Philosophical Magazine Part B*, 1997, **76**, 351-361.
120. S. E. Rodil, W. I. Milne, J. Robertson and L. M. Brown, *Appl. Phys. Lett.*, 2000, **77**, 1458-1460.
121. P.-C. Tsai, *Surf. Coat. Technol.*, 2007, **201**, 5108-5113.
122. G. Krannich, F. Richter, J. Hahn, R. Pintaske, V. B. Filippo and Y. Paderno, *Diamond Relat. Mater.*, 1997, **6**, 1005-1009.
123. V. Kouznetsov, K. Macák, J. M. Schneider, U. Helmersson and I. Petrov, *Surf. Coat. Technol.*, 1999, **122**, 290-293.

Chapter 3 - High Power Impulse Magnetron Sputtering (HiPIMS)

3.1 Introduction

High Power Impulse Magnetron Sputtering or HiPIMS is a fairly new physical vapor deposition method invented in 1999 by Kouznetsov et al.[1] Based on Direct Current Magnetron Sputtering (DCMS), it relies on extremely high peak power densities to increase the ionization rate and energy of the target species, which in turns improves film density. This chapter will explain in detail the principle of work for HiPIMS, as well as its specificities. In addition, the HiPIMS setup used for producing the research samples will be presented and described, with all its modifications and improvements performed on it over time.

3.2 Description

As mentioned in the introduction, HiPIMS’ working principle is based on a standard magnetron sputtering system, combined with a pulsed power supply in order to tune the plasma properties. HiPIMS relies on the exact same physical principle as DCMS, which is depending on the glow discharge of a gas (typically a noble gas such as argon or xenon) in order to get plasma.

3.2.1 Direct Current Magnetron Sputtering

A simple diagram describing how sputtering occurs in a standard magnetron sputtering device is shown in Figure 3.1. A high negative voltage of several hundred volts is applied at the cathode (target), inducing a glow discharge in the gas (usually argon and/or nitrogen) in order to ionize it. As the gas molecules become positively charged, they would be accelerated towards the negatively charged target and sputter it. A magnetron would trap the ionized species and confine them to the vicinity of the target thanks to powerful magnetic field lines, thus increasing the sputter yield, as well as the ionization rate or the target thanks to gas and electron secondary collision with the sputtered atoms. Those ionized atoms will then either be trapped in the field lines and re-sputter the target or they will escape them and contribute to the thin film growth at the substrate.

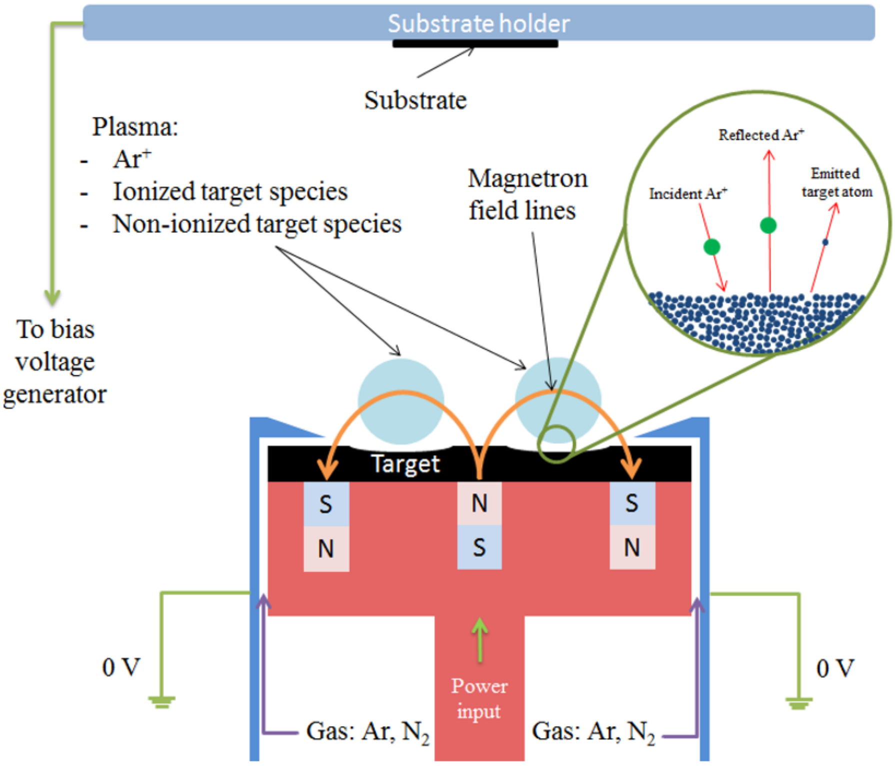

Figure 3.1 - Working principle of a magnetron sputtering process

3.2.2 HiPIMS

HiPIMS distinction with DCMS comes from its On/Off ratio, working in a pulsed fashion. The duty cycle usually remains below 5%, allowing an increase in current densities a few orders of magnitude higher while keeping the average power the same as that of a typical DCMS setup. The table below in Figure 3.2 compares the performances of HiPIMS with DC Magnetron Sputtering.

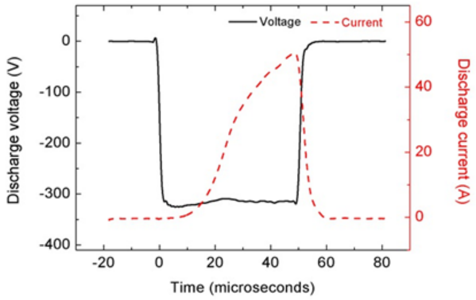

Property	DC Magnetron	HiPIMS
Peak power density	1 W.cm^{-2}	1000 W.cm^{-2}
Average power density	1 W.cm^{-2}	1 W.cm^{-2}
Current density	0.01-0.1 A.cm^{-2}	1-1000 A.cm^{-2}
Discharge voltage	500 V	500 V
Ionization rate (for metals)	<5 %	30-100 %
Average Ion energy	5 eV	20 eV

Figure 3.2 - Left: Pulsed voltage and current discharge cycle.[2] Right: Comparison table between HiPIMS and a DC magnetron

Figure 3.2 shows a typical voltage and current pulse cycle where the voltage would decrease to a few hundred volts for a few ten of microseconds, allowing a current up to several hundred amps to channel through the ionized gas and target.[1] This high energy density of several hundred watts per square centimeter enables the formation of a very high density plasma with an increased ionization rate compared to DC sputtering. A picture of the HiPIMS setup used for this work is shown in Figure 3.3, where carbon plasma can be observed.

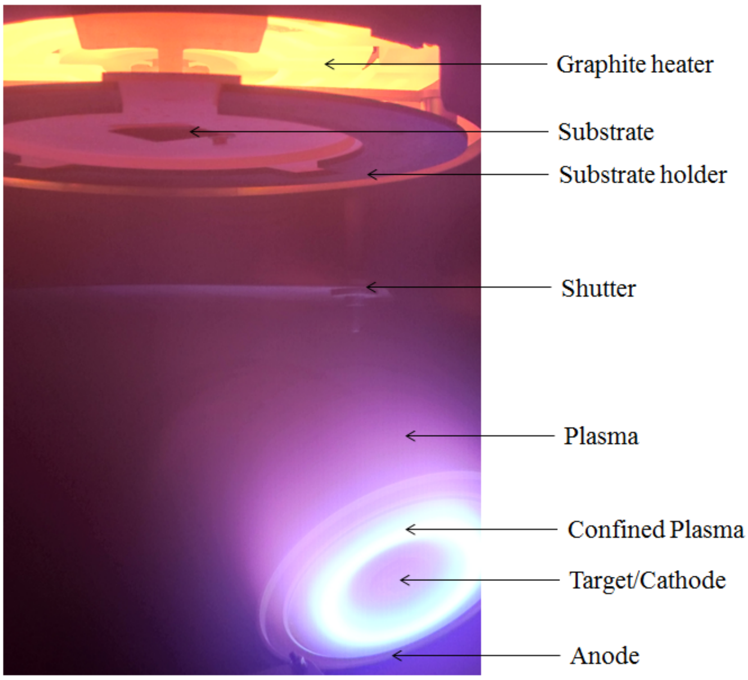

Figure 3.3 - HiPIMS system during carbon film growth a 1000 degC

The advantage of HiPIMS is that it is easily upgradable from a DCMS system where only the power supply needs replacement, while the vacuum chamber and magnetron do not require any change. This provides an advantage for industrial applications as there is no need for huge investments into a brand new system and the transition from DC to pulsed current can be made seamless.

3.2.3 Comparison with FCVA

From the beginning, HiPIMS has been a successful solution for material growth as it was able to combine the advantages of conventional sputtering with the increased plasma ionization of more energetic deposition methods such as cathodic arc or ion plating. The difference between a plasma discharge in DC mode and HiPIMS mode has been discussed above and lies in the plasma energetics obtained by high intensity short pulses in HiPIMS mode. This kind of operating mode is very close to Filtered Cathodic Vacuum Arc or FCVA, which uses vacuum arc discharges to generate plasma. Even though FCVA and HiPIMS are similar in principle, the plasma they generate is vastly different.

3.2.3.1 Plasma density

Looking at the plasma density is a good way of understanding how much energy is involved during plasma discharge. Indeed, a denser plasma means a higher energy discharge. For instance, FCVA's plasma density is extremely high due to the explosive nature of the vacuum arc discharge, with values up to 10^{18} m^3 in the substrate area (10^{26} m^3 at the target area),[3, 4] while HiPIMS' plasma density is notably a few orders of magnitudes lower, with values of 10^{18} m^3 at the target area.[5, 6]

3.2.3.2 Deposition rates

The plasma density directly affects the growth rates, as more species in the plasma will increase the likelihood of them reaching the substrate and contributing to the overall thin film growth. For instance, due to the extremely high energy process during plasma generation in the FCVA process, deposition rates can reach up to 5 nm/s for the growth of carbon.[7] In comparison, and as will be discussed later in this chapter, the deposition rate at the same average power for HiPIMS is already lower compared to DCMS[8] and the maximum reported growth rate for carbon was below 2 nm/s, in the condition of using extremely high average power (50kW), otherwise the rate would significantly drop to below 0.5 nm/s.[9]

3.2.3.3 Plasma energy

An important parameter in PVD growth is the plasma energy, or more commonly the energy of the charged ions that will make up the thin film material. HiPIMS type plasma discharges comprise 3 main parts: a low energy sharp thermal peak at around

1 eV, followed by a broad main peak in the tens of eV caused by the impact of energetic particles (energized ions and electrons) with the sputtered species[10] and finally a very long energy tail reaching up to several hundreds of eV.[11] On the other hand, FCVA plasma energy distribution is much simpler due to the fact that it is filtered. Indeed, filtering via magnetic coils will selectively keep only the charged ions with a specific energy window, which is typically in the tens of eV or even up to around 100 eV.[12]

3.2.3.4 Scalability and cost effectiveness

The previous aspects comparing FCVA with HiPIMS seemed to show that FCVA is superior in all areas. However, that last comparison point is the most critical when seen from an industrial point of view. Undeniably, the scalability of HiPIMS has been demonstrated with peak power in the megawatt range and target sizes up to a meter, while exhibiting particle free, high coating quality.[13, 14] Unfiltered on the other hand vacuum arc is commonly used in industrial processes, as its high deposition rate makes it economically viable. However, it is limited to technological processes where macroparticles are tolerated and is not usable for high precision fabrication processes such as electronic devices.

3.2.3.5 Conclusion

Due to its pulsed regime, HiPIMS is capable of drastically increase its plasma density (and thus plasma energy) to approach the FCVA plasma conditions. In comparison, the plasma density for a DCMS process is around 1000 times lower than HiPIMS, with typical values in the order of 10^{15} m^3.[15]

3.3 Current work using HiPIMS

3.3.1 Theoretical study of HiPIMS

3.3.1.1 Defining HiPIMS

The first work undertaken on HiPIMS was to properly define its properties, and what can be considered a "HiPIMS mode". Gudmundsson et al.[16] gave an accurate definition of HiPIMS growth regime as seen in Figure 3.4 where the HiPIMS region is defined as the zone where the duty cycle falls below 5%, with peak power densities in the hundreds of Watts per square centimeter.

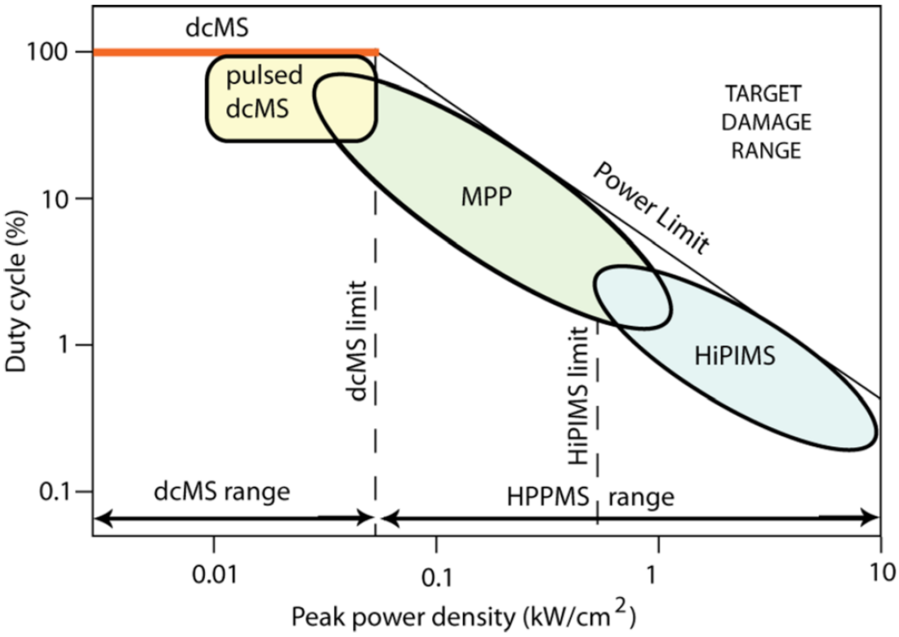

Figure 3.4 - Classification of various pulse discharges and where the HiPIMS region is. MPP stands for Modulated Pulse Power and is an in-between regime between HiPIMS and DCMS.[16]

Here, the peak power density is computed using the following equation:

$$P_{peak} = \frac{V_{discharge} I_{average}}{\delta_{ON} A_{target}} \quad (3.1)$$

$V_{discharge}$ is the voltage during plasma discharge, $I_{average}$ is the average current during growth (not the peak current per pulse), δ_{ON} is the duty cycle and A_{target}

is the target area. Typically, the target area for a 3 inch target is 45.6 cm^2. δ_{ON} varies from 0 to 1, where 0 is a duty cycle of 0% (no pulsing), and 1 is 100% (DCMS operation). For instance, a duty cycle of 1%would give $\delta_{ON}=0.01$. The peak power density is important in HiPIMS literature as it is one of the main metrics to directly compare the growth conditions between two different HiPIMS systems.

3.3.1.2 Target ionization rate

The main advantage of HiPIMS compared to DCMS is its capability to increase the ionization rate of the sputtered target, and as such, a lot of studies worked on quantifying the increase in ionization. The experimental setup remains fairly the same across the literature, with a magnetron device connected to a HiPIMS power supply, and an instrument positioned 5 to 10 cm away from the magnetron to measure the ion energy distribution functions (IEDFs) of the incoming plasma. The measuring instrument is typically a Langmuir probe or a more complex derivation of it, capable of increasing signal-to-noise ratio or time/energy resolution. Many studies were performed to quantify exactly the impact of various parameters, such as the discharge voltage, pulse length, peak current, peak power density, gas pressure or the type of ionized gas used. For instance, Ehiasarian et al. studied the impact of peak current and its effects on chromium plasma. By increasing the peak current to values as high as 40 A, the ratio between Cr^{2+} and Cr^0 as well as Cr^+ and Cr^0 was multiplied by 10.[17] In a similar study, Lundin et al. showed that an increase in pulse current density would increase the ionization rate of Ti and Al plasmas, with this trend verified at several growth pressure and discharge pulse length.[18] In a general fashion, the current research work has demonstrated that an increase in peak power density would induce an increase in ionization of the sputtered target.

3.3.1.3 Growth parameters

A lot of HiPIMS studies were focused on the impact of growth parameters on the film properties. For instance, Schmidt et al. studied the influence of sputtering gas on the microstructure of CN thin films, showing that Ar and Kr display a more pronounced fullerene-like structure compared to Ne.[19] DC bias voltage can also be applied to the substrate and due to the increase ionization rate of the sputtered species, a greater film growth control can be obtained with HiPIMS, as observed for example by Wang et al. in the study of TiN coatings with bias voltages varying from 50 V to 400 V.[20] A combination of parameters can be changed simultaneously and Zhang et al. studied the hardness and smoothness of TiB_2 coatings as various bias voltages and temperatures.

3.3.1.4 Plasma density inhomogeneity

Plasma studies of HiPIMS are numerous and are either focused on the plasma composition as explained in section 3.1.2, or on localized changes in plasma density, with zones in the sputtering area that have higher plasma density and are commonly called plasma spokes. Spokes are obtained in $\vec{q}=-k\nabla T$ discharges as the ionized species are rotating along the field lines in the azimuthal direction (planar to the target), generating a preferential sputter zone called the racetrack (see Figure 3.5).

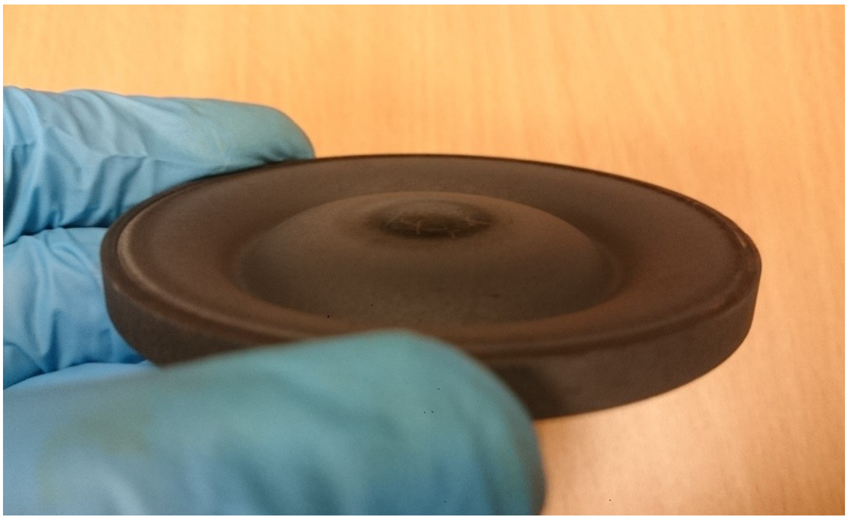

Figure 3.5 - Picture of a used carbon target displaying the typical racetrack due to the spokes of plasma always moving along the same circular region.

Those spokes have been experimentally observed in HiPIMS mode and their shape changes depending on the growth conditions as shown by Ehiasarian et al. in Figure 3.6.[21]

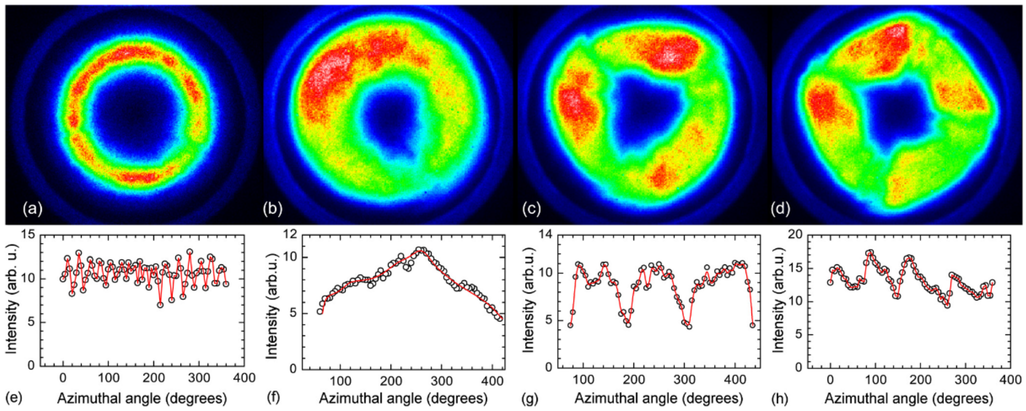

Figure 3.6 - Influence of peak current density J_d and Ar pressure P_{Ar} on the discharge: (a) and (e) $J_d=0.75$ A.cm^{-2}, $P_{Ar}=0.17$ Pa; (b) and (f) $J_d=7.5$ A.cm^{-2}, $P_{Ar}=0.17$ Pa; (c) and (g) $J_d=7.5$ A.cm^{-2}, $P_{Ar}=1.0$ Pa; (d) and (h) $J_d=7.5$ A.cm^{-2}, $P_{Ar}=1.7$ Pa. Upper row: fast photography frames (false color), lower row: total light intensity vs azimuthal angle corresponding to a circle along the centre of the racetrack. Angle is counted clockwise.[21]

Brenning et al. suggested the spokes were related to the critical ionization velocity (CIV)[22] and used this theoretical background to explain in which conditions spokes are formed and how their geometry varies accordingly to the discharge parameters. CIV comes from Alfvén in 1942 and suggested that a plasma would incur a strong increase in ionization rate if its relative motion in a magnetic field is greater than the CIV υ_c , given by equation 3.2:[22]

$$\upsilon_c = \sqrt{\frac{2eU_i}{m_n}} \qquad (3.2)$$

Where U_i and m_n are the ionization potential and mass of the atom or molecule making the plasma species, respectively. In the case of HiPIMS, the typical speed for ions in the plasma is in the range of 10 km/s while electrons move at a speed an order of magnitude higher. Explaining how spokes behave during a HiPIMS discharge is critical in the understanding of how to increase the ionization rate as well as how to get a stable plasma in HiPIMS discharges.

3.3.2 Growth of metal based thin films with HiPIMS

HiPIMS has so far mostly been used for the growth of metals, where it can reach an ionization rate of the target up to 100%.[18] The increased plasma density yields a better film adhesion to the substrate with improved density. Using those advantages, research mainly focused on the improvement for example in optical,[23] corrosion[24] or oxidation[25] properties with HiPIMS grown films compared to DCMS. Figure 3.7 shows the difference in plasma between the sputtering of copper in DCMS mode and HiPIMS mode. DCMS would only slightly ionize the sputtered copper species and the glow discharge would be pink, which is the typical emission spectrum of argon. Once the current density is increased, the glow will turn towards a greenish color which is typical of the optical emission of ionized copper, indicating an increase in ionized copper in the sputtered species.

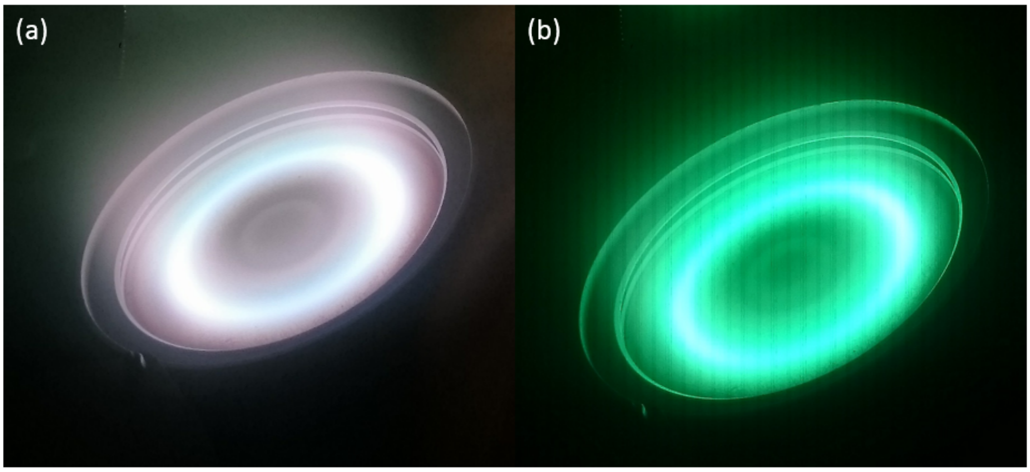

Figure 3.7 - Left: Plasma discharge of a copper target in DCMS mode at 200 W average power, or 4.5 W.cm^{-2} peak power density. The pink colour comes from the argon gas which is being ionized by the glow discharge. Right: Plasma discharge of a copper target in HiPIMS mode at 200 W average power, or 25 W.cm^{-2} peak power density. The green colour comes from the ionized copper and the vertical lines come from the pulsing of the plasma combined with the shutter speed of the camera.

3.3.3 Growth rate study

The main downside about HiPIMS is its lower growth rate, which is to be expected by the lower duty cycle compared to DCMS mode. However, an increase peak power density is supposed to counteract the lower duty cycle, by inducing a plasma of higher density during the ON time. Samuelsson et al. summarized some metal growth rates with HiPIMS and compared them with DCMS at equivalent average power to quantify the difference between the two,[8] as shown in Figure 3.8 below:

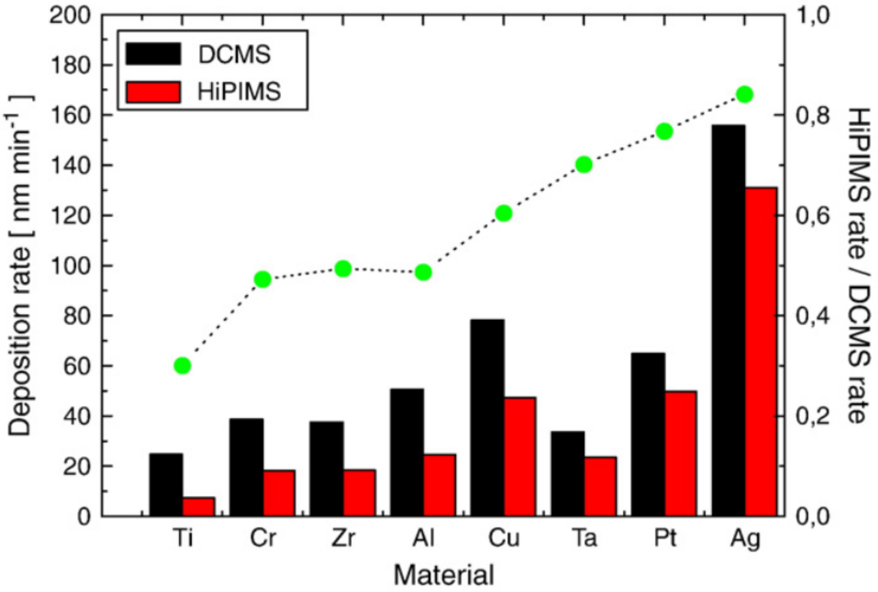

Figure 3.8 - The deposition rates for DCMS and HiPIMS discharges plotted as bars for the different target materials used (left axis). The deposition rate of HiPIMS over DCMS deposition rate is shown as a scatter plot (right axis).[8]

This weakness in HiPIMS growth is the main drawback for a more global industrial use compared to DCMS, and is studied in depth in order to find a way to close the gap. For instance, a study of the impact on growth rate by the magnetic field strength at the magnetron or the racetrack depth has been performed, concluding a shallower racetrack and a strong magnetic field would improve the growth rate the most.[26] Another study concluded that the deposition rate ratio between HiPIMS and DCMS would decrease exponentially with an increase of peak current density and is independent of the target source. This effect is attributed to the “return effect” where ionized target materials get trapped by the magnetic field and re-sputter the target instead of contributing to the growth rate. This happens less at lower current densities where much less target material is ionized and hence affected by the magnetic field trap.[27] In conclusion, improving the growth rate for HiPIMS is a topic of research attracting a lot of industrial interest and HiPIMS has yet to reach the same performance as DCMS with this regard.

3.3.4 Growth of non-metals

As a PVD growth method with high plasma density and energy, HiPIMS attracted the same research interests as FCVA growth. As such, some work has been carried on the HiPIMS growth of carbon and carbon nitride. However, the results are somewhat disappointing with sp^3 ratio of maximum 40% (except for a few cases discussed below) as carbon is extremely difficult to ionize and hence no high density film can be grown to obtain good quality diamond-like carbon.[28] Other works reported ratios as high as 80% by increasing the power up to 50 kW[9] to induce a higher film density, while others used a gas with higher ionization energy such as neon to increase the ionization rate of carbon[29] or some voluntarily induced HiPIMS discharges that would create arcs to get a plasma similar to what can be obtained with an FCVA source.[30] In a similar fashion to the growth of carbon using neon gas, carbon nitride was attempted with HiPIMS using different sputter gases, such as argon, neon or krypton and their impact on microstructure was reported,[19] but not many innovative applications or materials were found that were not possible before HiPIMS was invented.

3.4 HiPIMS setup in the lab and upgrades

This section summarizes all the work I performed on the HiPIMS system. As the Principal Investigator (PI) for the HiPIMS system, I was in charge of its cleaning and maintenance. In addition, I was given some freedom on designing upgrades, purchasing and installing the required equipment which was necessary to enable the growth of BN and CN with HiPIMS. While using the system, many avenues for optimization and improvement were found. This section outlines the main upgrades performed and some modifications implemented as a fix to existing defects. A System Operational Procedure (SOP) document was created to help the user follow standard procedure when using the equipment. This document was maintained and updated on the fly to take into account the new upgrades as well as maintenance procedures and this document can be found in Appendix A.

3.4.1 System upgrades

3.4.1.1 Hardware upgrades

The HiPIMS system has been upgraded over time, in order to improve its capabilities as well as making the whole system more reliable and efficient. The initial sputtering system as seen in Figure 3.9a was made up of a vacuum chamber with its backing and turbomolecular pumps, one magnetron source, a graphite heater and DC bias voltage source. The rack would include a DC power supply for the bias, another one to feed power to the HiPIMS power supply as well as one last to provide power for the graphite heater. Two mass flow controllers (MFCs) are hooked up to the chamber, one for argon and the other one for nitrogen. There is a vacuum gauge capable of providing the chamber pressure from atmospheric pressure to 1e^{-8} mbars. The HiPIMS power supply is controlled by a software installed on the computer (see Figure 3.10 further down).

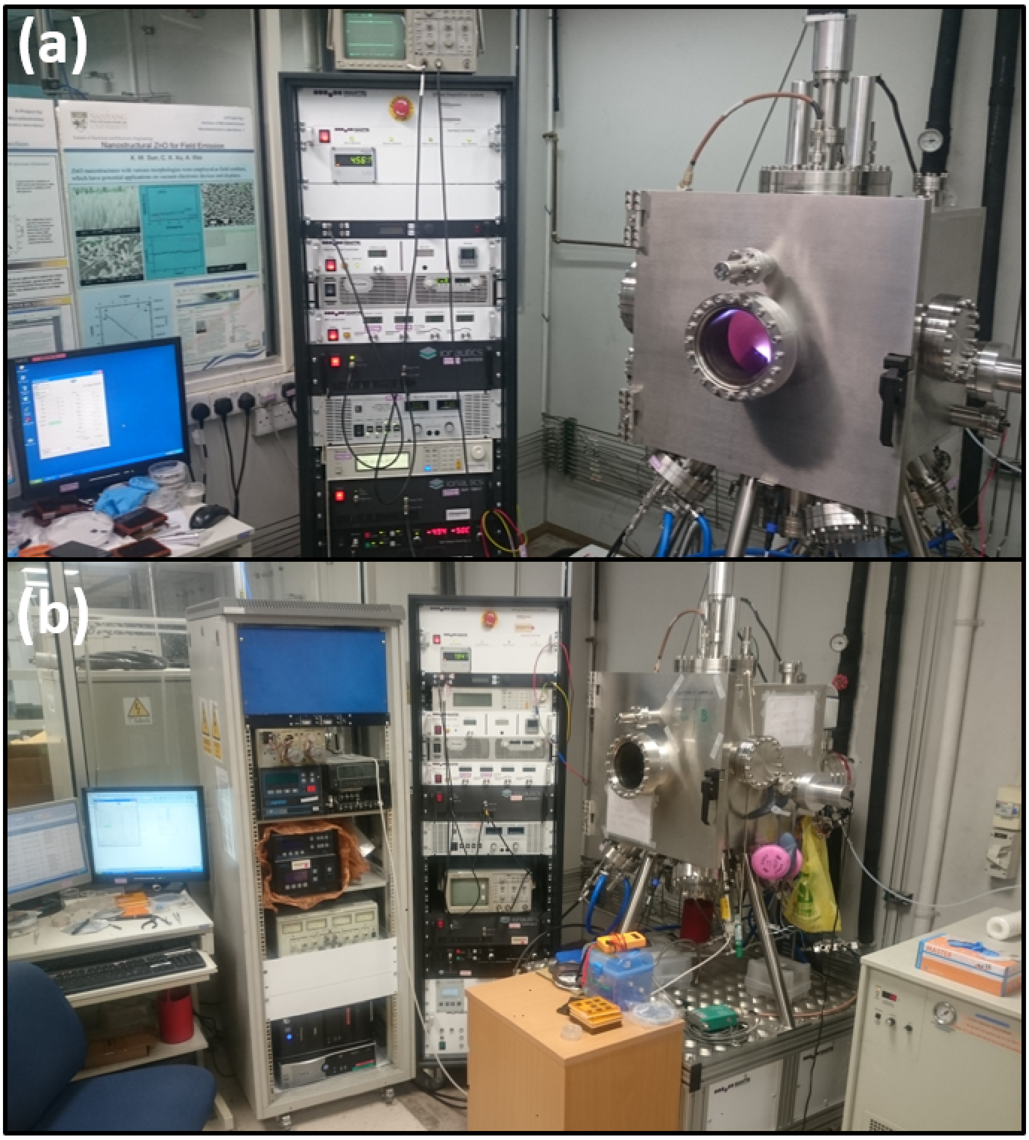

Figure 3.9 - (a) HiPIMS system as first delivered, including one HiPIMS power supply and magnetron source. (b) Upgraded system comprising two HiPIMS power supplies, two magnetron sources, a HiPIMS pulse synchronization unit, one RF power supply and its own closed circuit water cooling system.

The upgraded HiPIMS system (Figure 3.9b) contains an additional rack for the two computers, as well as two sets of RF power supplies (only one is currently used) and an additional vacuum gauge to provide redundancy in the pressure reading. The additional computer is to control the second HiPIMS power supply that has been added.

3.4.1.2 Dual-HiPIMS setup

In addition to adding another HiPIMS power supply with a second magnetron, an extra pulse synchronization unit capable of fine tuning the pulse triggering between the two magnetron sources was setup. This unit would allow the control of the pulse discharge between the two magnetron sources, allowing greater flexibility when using both sources at the same time. It has two modes: Delay and Burst, the former triggers a pulse from a source and waits exactly an amount of time t before triggering a pulse from the other source, while the latter would trigger n pulses from one magnetron source followed by m pulses from the other one.

3.4.1.3 Grow automation

The HiPIMS Control software (Figure 3.10) allows to remotely control the pulse parameters by varying the discharge voltage and current or set the pulse frequency and pulse length. It also has some limiting parameters such as the maximum set power or peak current in order to make sure the plasma will not reach regions of instability or dangerous for the equipment and the user. The downside of this software is that it does not include any automation and the user has to be present to switch on and off the plasma, or change parameters when required. This becomes quite troublesome when certain growths require several cycles of growth and cooldown, and last for several hours when the user has to start and stop the plasma every 10 minutes for instance.

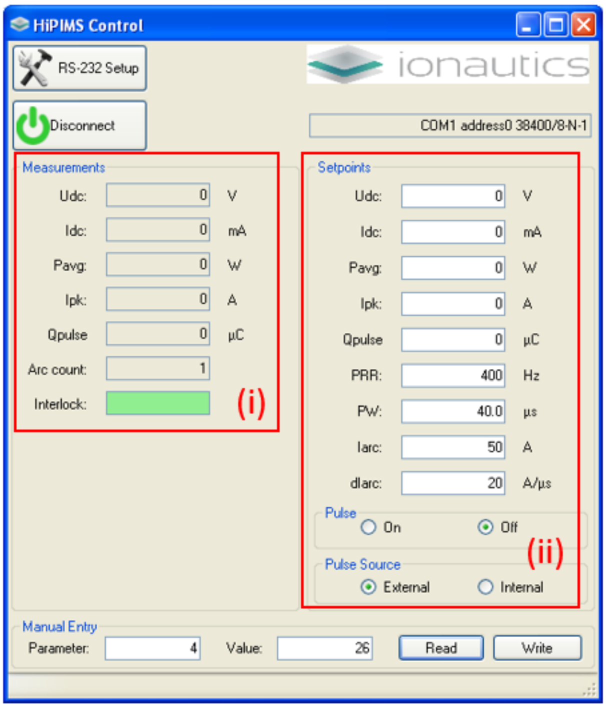

COM1 address0 38400/8-N-1

Measurements
Udc: 0 V
Idc: 0 mA
Pavg: 0 W
Ipk: 0 A
Qpulse 0 µC
Arc count: 1
Interlock: 🟩

Setpoints
Udc: 0 V
Idc: 0 mA
Pavg: 0 W
Ipk: 0 A
Qpulse 0 µC
PRR: 400 Hz
PW: 40.0 µs
Iarc: 50 A
dIarc: 20 A/µs
Pulse ○ On ● Off
Pulse Source ● External ○ Internal

Manual Entry
Parameter: 4 Value: 26

Figure 3.10 - HiPIMS controller software, using the COM port to communicate: either send data using the right hand side of the window (inset (ii)) or receive live status info in the left hand side (inset (i)).

In order to simplify the process, some VBA code has been written to bypass the HiPIMS control software and directly communicate with the HiPIMS power supply. The code is shown in Figure 3.11 and uses loops and "wait" functions in order to create timers and start/stop the plasma whenever required. The user inputs data via the spreadsheet as shown in Figure 3.11a and the VBA code will pick it up to run the recipe on its own.

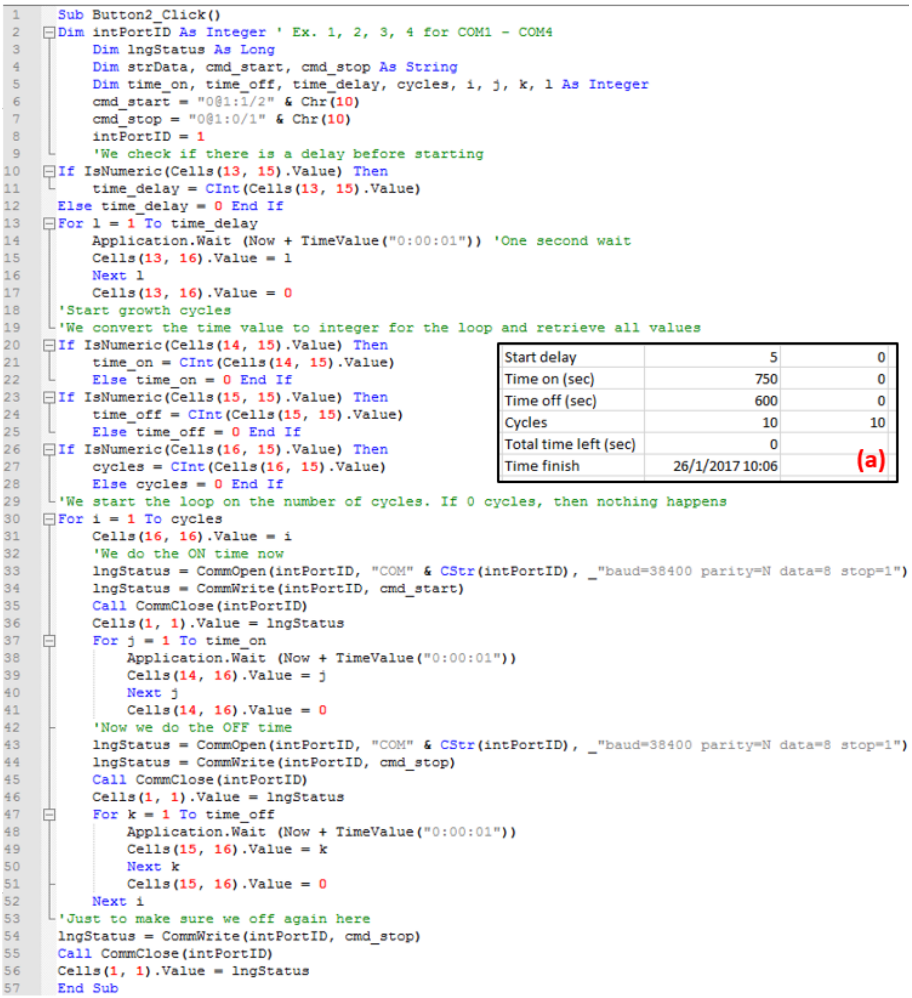

```vba
Sub Button2_Click()
Dim intPortID As Integer ' Ex. 1, 2, 3, 4 for COM1 - COM4
    Dim lngStatus As Long
    Dim strData, cmd_start, cmd_stop As String
    Dim time_on, time_off, time_delay, cycles, i, j, k, l As Integer
    cmd_start = "0@1:1/2" & Chr(10)
    cmd_stop = "0@1:0/1" & Chr(10)
    intPortID = 1
    'We check if there is a delay before starting
If IsNumeric(Cells(13, 15).Value) Then
    time_delay = CInt(Cells(13, 15).Value)
Else time_delay = 0 End If
For l = 1 To time_delay
    Application.Wait (Now + TimeValue("0:00:01")) 'One second wait
    Cells(13, 16).Value = l
    Next l
    Cells(13, 16).Value = 0
'Start growth cycles
'We convert the time value to integer for the loop and retrieve all values
If IsNumeric(Cells(14, 15).Value) Then
    time_on = CInt(Cells(14, 15).Value)
    Else time_on = 0 End If
If IsNumeric(Cells(15, 15).Value) Then
    time_off = CInt(Cells(15, 15).Value)
    Else time_off = 0 End If
If IsNumeric(Cells(16, 15).Value) Then
    cycles = CInt(Cells(16, 15).Value)
    Else cycles = 0 End If
'We start the loop on the number of cycles. If 0 cycles, then nothing happens
For i = 1 To cycles
    Cells(16, 16).Value = i
    'We do the ON time now
    lngStatus = CommOpen(intPortID, "COM" & CStr(intPortID), _"baud=38400 parity=N data=8 stop=1")
    lngStatus = CommWrite(intPortID, cmd_start)
    Call CommClose(intPortID)
    Cells(1, 1).Value = lngStatus
    For j = 1 To time_on
        Application.Wait (Now + TimeValue("0:00:01"))
        Cells(14, 16).Value = j
        Next j
        Cells(14, 16).Value = 0
    'Now we do the OFF time
    lngStatus = CommOpen(intPortID, "COM" & CStr(intPortID), _"baud=38400 parity=N data=8 stop=1")
    lngStatus = CommWrite(intPortID, cmd_stop)
    Call CommClose(intPortID)
    Cells(1, 1).Value = lngStatus
    For k = 1 To time_off
        Application.Wait (Now + TimeValue("0:00:01"))
        Cells(15, 16).Value = k
        Next k
        Cells(15, 16).Value = 0
    Next i
'Just to make sure we off again here
lngStatus = CommWrite(intPortID, cmd_stop)
Call CommClose(intPortID)
Cells(1, 1).Value = lngStatus
End Sub
```

Start delay	5	0
Time on (sec)	750	0
Time off (sec)	600	0
Cycles	10	10
Total time left (sec)	0	
Time finish	26/1/2017 10:06	(a)

Figure 3.11 - VBA code for excel to automate the cycles of growth and cooldown. This code relies on the use of VBA libraries to use the COM ports to communicate with the HiPIMS power supply. Inset (a) is the data in the excel spreadsheet with the left column being specified by the user and the right column status update from the VBA code.

3.4.2 System failures and modifications

While being used, the HiPIMS system had several issues with the most notable ones reported below. Most of the issues came from design issues that have been solved by modifying the equipment.

3.4.2.1 HiPIMS power supply transistor failure

This issue is unfortunately unavoidable and will eventually happen. However, there are ways of increasing the transistors life. Indeed, each HiPIMS power supply contains four power transistors in parallel capable of taking up to 100 A of current each, or peaks of 400 A together before reaching failure state. As the power supply is designed to be used for currents below 100 A, this limit of 400 A should never be reached. However, arcs happen and this is when the transistors get damaged. A way to reduce the risk is to use the power supply with a very stable recipe where very few arcs occur, at peak current well below the limit.

3.4.2.2 Bias voltage issue due to arcs

The HiPIMS system has initially been designed for the growth of metals which are always conductive. When starting to grow dielectric materials, the deposition of non-conductive coatings onto the chamber walls and especially the main substrate holder rotating shaft created unforeseen issues. For instance, the bias voltage connection from the sample holder to the DC power supply is done by two metallic lamellas in contact with the shaft. Unfortunately, when growing dielectric materials, the shaft would get coated with a thin layer of non-conductive material, creating electrical breakdowns between the lamellas and the shaft. This would damage the lamellas until the stop being in contact with the shaft, effectively making DC biasing impossible (see Figure 3.12). A solution to this issue was to replace the lamellas with a thicker copper cable, wrapped around the shaft, and moved much further away from the substrate holder to avoid the deposition of dielectric thin films on the shaft.

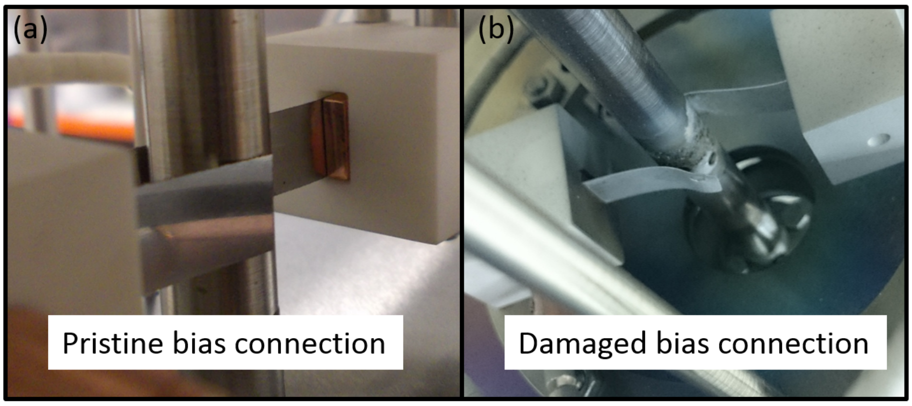

Figure 3.12 - (a) Brand new DC bias connection between the metallic lamellas (connected to the DC power supply) and the shaft holder the substrate holder. (b) Same shaft and lamellas after electrical breakdowns have occurred and the DC bias function stopped working.

3.4.2.3 Water cooling issue and need to change to an internal cooler

Figure 3.9b shows the addition of a closed circuit water cooling system in the bottom right corner of the picture. This is due to the main water cooling network being unstable and frequently going down. Using a dedicated chiller allowed the magnetron sources and turbopump to always be cooled at the same temperature, and increases the system stability.

3.4.2.4 N connector cable burn due to overheating and arcs

The use of N connectors on coaxial cables is a design issue as they are not designed to sustain loads of several dozens of amperes. In addition, a weak contact between the male and female connector would lead to arcs and overheating of the cable. Eventually, the cable would fail and need to be changed (see Figure 3.13). A new design based on HN connectors, which are more robust, is being investigated to permanently avoid this issue in the future.

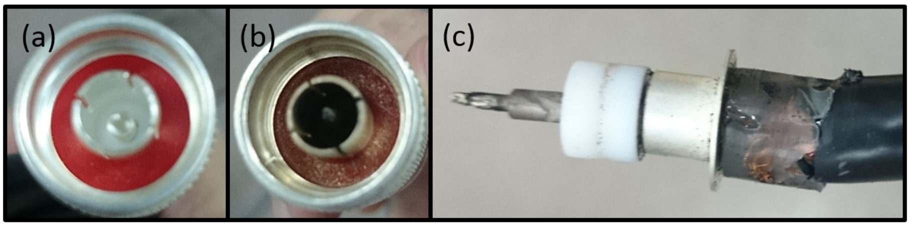

Figure 3.13 - (a) Brand new N type coaxial cable. (b) Same N type coaxial cable after heavy usage. (c) Same coaxial cable as in (b) without the metallic connector, showing extensive heat damage.

3.4.2.5 Target cracking

In order to maintain process stability, the duty cycle has to remain low. This is mainly to prevent the target from heating up too much, which could lead to melting or cracking (see Figure 3.14). A way to avoid target cracking is to keep the power down in order to make the temperature range smaller, as well as not tightening the Mo target holder too much to allow for small changes in target geometry. Another reason for keeping the high current pulses duration short is the current discharge mode that evolves with time. As the pulse starts, the type of discharge is a glow discharge; but after certain critical time, it will move to an arc discharge type which will make the plasma unstable and can damage the target and power supply.

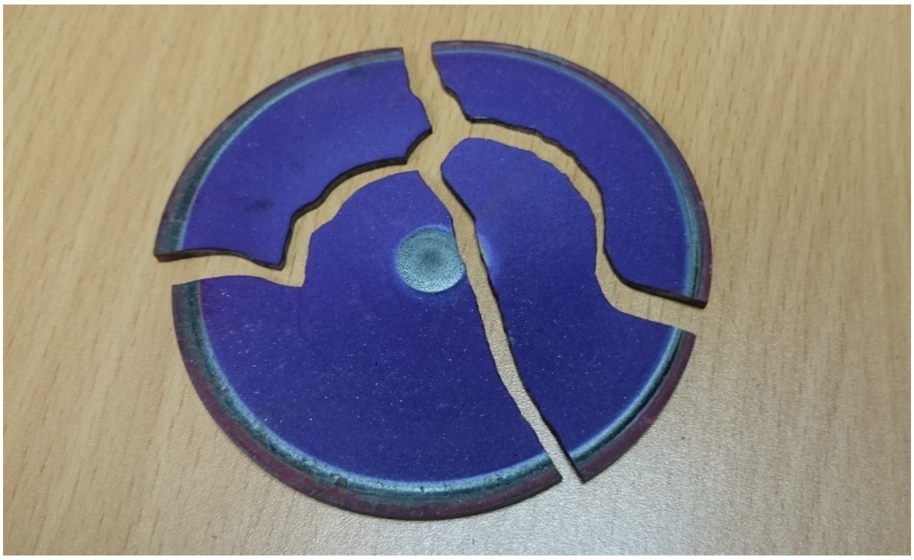

Figure 3.14 - Picture of LaB6 target that cracked due to the different coefficient of thermal expansion between the target, the copper magnetron and the Mo target holder.

3.5 Conclusion

HiPIMS growth of metals and plasma studies are well covered in the literature, with the current work being focused on the growth of dense metal oxides or metal nitrides. However, apart from carbon where the results are not as promising as for metallic materials, very little work has been done on the growth of ceramic materials and this remains a topic to explore for HiPIMS. In particular, the growth of BN with HiPIMS is completely absent from the literature while many studies have been performed with DCMS or RF sputtering. This is why current HiPIMS system has been modified and upgraded to permit the growth of ceramic based materials such as carbon, boron nitride, carbon nitride and eventually BCN, in order the explore the growth of such materials with the capabilities of HiPIMS.

3.6 References

1. V. Kouznetsov, K. Macák, J. M. Schneider, U. Helmersson and I. Petrov, *Surf. Coat. Technol.*, 1999, **122**, 290-293.
2. D. Lundin and K. Sarakinos, *J. Mater. Res.*, 2012, **27**, 780-792.
3. B. Juttner, H. Pursch and S. Anders, *J. Phys. D: Appl. Phys.*, 1984, **17**, L111.
4. A. Anders, S. Anders, B. Juttner, W. Botticher, H. Luck and G. Schroder, *IEEE Transactions on Plasma Science*, 1992, **20**, 466-472.
5. A. P. Ehiasarian, A. Vetushka, A. Hecimovic and S. Konstantinidis, *J. Appl. Phys.*, 2008, **104**, 083305.
6. A. Anders, *Appl. Phys. Lett.*, 2012, **100**, 224104.
7. P. Siemroth, J. Berthold, B. Petereit, H. H. Schneider and H. Hilgers, *Surf. Coat. Technol.*, 2004, **188–189**, 684-690.
8. M. Samuelsson, D. Lundin, J. Jensen, M. A. Raadu, J. T. Gudmundsson and U. Helmersson, *Surf. Coat. Technol.*, 2010, **205**, 591-596.
9. M. Hiratsuka, A. Azuma, H. Nakamori, Y. Kogo and K. Yukimura, *Surf. Coat. Technol.*, 2013, **229**, 46-49.
10. P. Matjaž, F. Robert and A. André, *Plasma Sources Sci. Technol.*, 2014, **23**, 025007.
11. M. Aiempanakit, A. Aijaz, D. Lundin, U. Helmersson and T. Kubart, *J. Appl. Phys.*, 2013, **113**, 133302.
12. A. Anders and G. Y. Yushkov, *J. Appl. Phys.*, 2002, **91**, 4824-4832.
13. A. Surpi, T. Kubart, D. Giordani, M. Tosello, G. Mattei, M. Colasuonno and A. Patelli, *Surf. Coat. Technol.*, 2013, **235**, 714-719.
14. E. Broitman, Z. Czigány, G. Greczynski, J. Böhlmark, R. Cremer and L. Hultman, *Surf. Coat. Technol.*, 2010, **204**, 3349-3357.
15. C. Christou and Z. H. Barber, *Journal of Vacuum Science & Technology A: Vacuum, Surfaces, and Films*, 2000, **18**, 2897-2907.
16. J. T. Gudmundsson, N. Brenning, D. Lundin and U. Helmersson, *Journal of Vacuum Science & Technology A*, 2012, **30**, -.
17. A. P. Ehiasarian, R. New, W. D. Münz, L. Hultman, U. Helmersson and V. Kouznetsov, *Vacuum*, 2002, **65**, 147-154.
18. L. Daniel, Č. Martin and H. Zdeněk, *Plasma Sources Sci. Technol.*, 2015, **24**, 035018.
19. S. Schmidt, Z. Czigány, G. Greczynski, J. Jensen and L. Hultman, *Journal of Vacuum Science & Technology A*, 2013, **31**, -.
20. Z. Wang, D. Zhang, P. Ke, X. Liu and A. Wang, *Journal of Materials Science & Technology*, DOI: .
21. A. P. Ehiasarian, A. Hecimovic, T. d. l. Arcos, R. New, V. S.-v. d. Gathen, M. Böke and J. Winter, *Appl. Phys. Lett.*, 2012, **100**, 114101.
22. N. Brenning, D. Lundin, T. Minea, C. Costin and C. Vitelaru, *J. Phys. D: Appl. Phys.*, 2013, **46**, 084005.
23. S. Konstantinidis, J. P. Dauchot and M. Hecq, *Thin Solid Films*, 2006, **515**, 1182-1186.
24. Y. P. Purandare, A. P. Ehiasarian and P. E. Hovsepian, *Journal of Vacuum Science & Technology A: Vacuum, Surfaces, and Films*, 2008, **26**, 288-296.
25. P. E. Hovsepian, C. Reinhard and A. P. Ehiasarian, *Surf. Coat. Technol.*, 2006, **201**, 4105-4110.
26. V. Tiron, I. L. Velicu, O. Vasilovici and G. Popa, *J. Phys. D: Appl. Phys.*, 2015, **48**, 495204.
27. G. Greczynski and L. Hultman, *Vacuum*, 2016, **124**, 1-4.
28. T. Konishi, K. Yukimura and K. Takaki, *Surf. Coat. Technol.*, 2016, **286**, 239-245.
29. A. Aijaz, K. Sarakinos, D. Lundin, N. Brenning and U. Helmersson, *Diamond Relat. Mater.*, 2012, **23**, 1-4.

30. R. Ganesan, D. G. McCulloch, N. A. Marks, M. D. Tucker, J. G. Partridge, M. M. M. Bilek and D. R. McKenzie, *J. Phys. D: Appl. Phys.*, 2015, **48**, 442001.

Chapter 4 - A study of vertically ordered Boron Nitride grown with HiPIMS

4.1 Introduction

4.1.1 Rationale

As seen in Chapter 2, it was previously demonstrated that NCG has an excellent through-plane (i.e. perpendicular to its substrate) thermal conductivity[1] (TC) of up to 16 $W.m^{-1}.K^{-1}$, where fully amorphous carbon exhibits a maximum TC of 5 $W.m^{-1}.K^{-1}$. Producing NCG is straightforward and can be grown either at low temperature (below 200 degC) or by phase transformation of amorphous carbon films (i.e. laser annealing[2], stress induction[3]) making it potentially useful as a thermal dissipation material for electronic devices. However, its good electrical conductivity[4] prevents it from being used directly on active electronics as it would induce shorts. The objective here is to induce a similar phase transformation with Boron Nitride in order to study the impact on the material's TC, which is expected to increase in the through-plane direction, in the same fashion as for NCG. The assumption that BN can also exist in the same form as textured carbon comes from the fact that it is structurally similar to the carbon polymorphs, while remaining electrically insulative. In particular, turbostratic BN is of interest as it is isomorphically close to NCG. Unfortunately it is made of basal planes oriented in random directions which impedes the transport of phonon as the lack of continuity in the planes will induce phonon scattering, hence reducing the overall thermal conductivity. This is why from its discovery in the 1960s[5] until now, turbostratic BN is still considered undesirable and the research effort focused on suppressing its formation while trying to obtain cubic or hexagonal BN.[6-9] However, such turbostratic structure is a good indication that vertically aligned BN basal planes can be obtained from the control of the t-BN planes orientation.

4.1.2 Work performed

In this work, we produce the first controlled growth of hexagonal BN with basal planes vertically ordered, using HiPIMS.[10] The BN thin films obtained in this study are made of h-BN nanocrystals as described in chapter 2, where their plane alignment is in the vertical direction. When such nanostructure is observed in a BN film, and in order to distinguish it with other BN films made of the usual h-BN structure, this material is thermed vertically ordered h-BN, or *voBN*. As seen in Chapter 3, High Power Impulse Magnetron Sputtering or HiPIMS is a fairly new growth method mainly used for the growth of metals and their nitrides/oxides. Here, we exploit the advantages of HiPIMS to grow BN thin films. As a BN target cannot be used with HiPIMS due to its electrically insulative property, a Lanthanum Hexaboride (LaB_6) one was used instead to grow BN by reactively sputter it in nitrogen gas. When studying the thin film, it is shown that the resulting BN film is still electrically insulative with little lanthanum presence. In addition, the sp^2 clusters of BN, all ordered in the vertical direction across the film, are morphologically equivalent to the hexagonal BN structure and retain the same characteristics. Due to the continuously vertical ordering of the BN structure, phonon transport is improved in the through-film direction, with an out-of-plane thermal conductivity of 5.1 $W.m^{-1}.K^{-1}$. It is proposed that the high ordering of h-BN nanocrystals in the vertical direction is due to compressive stress induced by energetic ions during growth and as such, vertical ordering would minimize the Gibbs energy,[11, 12] as previously shown with carbon.[4, 13]

4.2 Experimental setup

4.2.1 Sample preparation

The BN films were prepared using a HiPIMS system as described in chapter 3. The plasma was obtained with a pulse length of 25 µs at a frequency of 4000 Hz, which is equivalent to a 10% duty cycle compared to DCMS. Each pulse would be 25-30 A (for a 3" target, this gives a peak current density of around 0.65 A.cm^{-2}) with a voltage of 350 V. The average power used to generate the pulses was 270 W, which gives a peak power density of around 60 W.cm^{-2}. The base pressure in the chamber was 10^{-6} mbar before growth, and 8x10^{-3} mbar during. A mentioned earlier, a three inches LaB_6 target was used as it has been shown it could generate a very dense and highly ionized boron plasma. [14, 15] The gas used for the glow discharge at the magnetron head was a mixture of nitrogen (20%) and argon (80%). Argon was used to make the glow discharge more stable (pure nitrogen gas is quite unstable and tends to generate a lot of arcs) while nitrogen was required to react with the boron ions and produce BN. Several BN samples were prepared on un-doped, double side polished silicon (100) substrates with various bias voltages (0 V or grounded, -47 V or floating, -75 V and -100 V) and various temperatures (room temperature or RT, 600 degC and 1000 degC).

4.2.2 Sample characterization

The crystalline structure of the film was studied using a High Resolution Transmission Electron Microscope (HRTEM Tecnai F20). The samples' cross section was analyzed and a slice of each sample was cut and thinned down using Focused Ion Beam (FIB) milling. A gallium ion beam of 30 kV was used to cut a slice in each sample, as well as thin down its thickness to below 100 nm. A beam at 5 kV was then used to clean up the sample before inserting it in the TEM. In addition to high resolution images, Electron Energy Loss Spectroscopy, or EELS, was used to determine the elemental composition (B, N and La atomic percentages). The film smoothness was quantified via Atomic Force Microscopy (AFM) by measuring a 25 µm square surface. A sheet resistance measurement was performed using a prober (Keithley 4500-SCS) using the 4-point probe method. In order to establish and quantify the presence of cubic or hexagonal BN, as well their ordering, Fourier Transform Infrared Spectroscopy (FTIR) was performed on the samples. This measurement requires samples transparent to infrared which is why un-doped silicon wafers were used, and they had to be double side polished as to avoid diffusing the IR incident beam. In order to evaluate the impact of film stress on the film structure, the samples' film stress were measured thanks to a surface profiler (Bruker DektakXT). The substrate's profile was measured before and after film growth (over a length of 10000 µm) and both profiles were compared to compute the film stress. Finally, some X-Ray Diffraction (XRD) measurements using the Bragg Brentano Geometry (Shimadzu XRD 600) were performed to cross-reference the presence and/or absence of cubic/hexagonal BN crystals in the samples. The slit divergence was 1 degree and the receiving slit 0.3 mm.

4.2.3 Thermal Conductivity characterization

Time Domain Thermoreflectance (TDTR)[16] was used to measure the thermal conductivity. TDTR has previously been widely used to measure the thermal properties on interfaces[17] and thin films.[18, 19] TDTR requires a known material on the sample surface to be used as a transducer and thus a 90 nm Al film was deposited. TDTR relies on a pump beam to provide excitation and a probe beam to quantify it. Both beams are generated via a polarizing beam splitter dividing a series of ultrashort laser pulses with a radius $1/e^2$ of 6-30 µm and a power of 25-130 mW. The power was dependant on the spot size as the steady state rise of temperature at the sample was kept below 10 K. Using an electro-optic modulator set at frequencies between 1 and 10 MHz, the probe beam excites the Al layer to heat it in a periodical fashion, while the time-delayed and synchronized probe beam resolves the periodic temperature change from the known change of reflectance of the Al layer. Using a thermal model capable of computing the heat flow in layered structures,[20] the thermal boundary resistance of the Al/BN interface as well as the out-of-plane BN thermal conductivity were derived, and the use of various modulation frequencies allowed a greater accuracy in the measurements.

4.3 Results and discussion

4.3.1 HiPIMS setup optimization for BN growth

As specified earlier, HiPIMS has been mostly used for the growth of metals sputtered either in Argon or reactively sputtered in nitrogen or oxygen gas. Some work has been done on the growth of carbon as well (see chapter 2) but no work was ever done on the growth of BN and hence the recipe and setup had to be designed from scratch in order to obtain some BN of proper quality. Similarly to DCMS, HiPIMS is not able to sputter a pure BN target as it requires a conductive material. In order to solve this issue, LaB_6 was used as it was previously shown to exhibit high ionization rate when sputtered in HiPIMS mode.[14, 15] Sputtering of LaB_6 is fairly straightforward and the plasma discharge mode can be set from DC (as in continuous) all the way to extremely short pulses with low duty cycle. However, DC mode would generate lower amount of ionized species while a low duty cycle would slow down the growth rate significantly as well as create plasma instabilities with arcs discharges occurring. Many parameters can be changed for the pulse discharge, the main ones being the average current, the pulse frequency and pulse length. The best trade-off between growth rate, stable plasma and high ionization rate seems to be for duty cycles of around 10% (ON to OFF ratio is 10% of the time). This value was reached by first adjusting the peak current to at least 25 A per pulse, as previous research work mentioned a value of over 20 A in order to get a plasma dominated by B species.[14] In addition to setting the peak current value to 25 A, the growth rate needed to be maximized, which can be done by adjusting the average current to its maximum value (1000 mA), as the growth rate is directly proportional to the average current. With the average current fixed to 1000 mA, it was only a matter of getting the maximum number of pulses per second, while keeping a peak current of around 25 A, which was obtained for a frequency of 4000 Hz, with pulses of 25 µs long, hence a duty cycle of 10%. It can be noted that this recipe is virtually equivalent to 2000 Hz with pulses 50 µs long, which provides a duty cycle of 10% as well, with peak current pulses of 25 A. However, it was observed that in HiPIMS mode a LaB_6 target would tend to easily arc when the pulses get any longer than 25 µs. This would make the plasma less stable and increase the risk of damaging the HiPIMS power supply so the final recipe was set to 4000 pulses per second, each pulse lasting 25 µs, with an average DC current of 1000 mA, leading to a peak current of 25 A per pulse.

4.3.2 Microstructural characterization of the BN samples

Vertically ordered BN (*voBN*) films with thicknesses up to 1500 nm were grown and no film dislocation was observed between the silicon substrate and the film. Figure 4.1 is a set of HRTEM images taken from a *voBN* film grown at room temperature and floating bias. In Figure 4.1a, a thin layer of amorphous BN of around 6 nm acts as a buffer layer between the substrate and the *voBN* layer. Film dislocations are averted as this layer plays the role of a buffer to alleviate the lattice mismatch between Si and *voBN*. The inset in Figure 4.1a is a Fast Fourier Transform (FFT) of Figure 4.1a and displays the pattern for high vertical ordering of the (0002) plane (with a distance between two planes of 0.35 nm). An additional FFT in Figure 4.1a shows that the silicon substrate is undamaged and highly crystalline, which is proof that the growth of BN did not damage it. The second image shown in Figure 4.1b is another HRTEM a few hundred nanometers up towards the film surface, with its computed FFT (see inset) displaying the characteristic arcs from the vertically aligned basal planes. This shows that such vertical alignment can be found everywhere in the film.

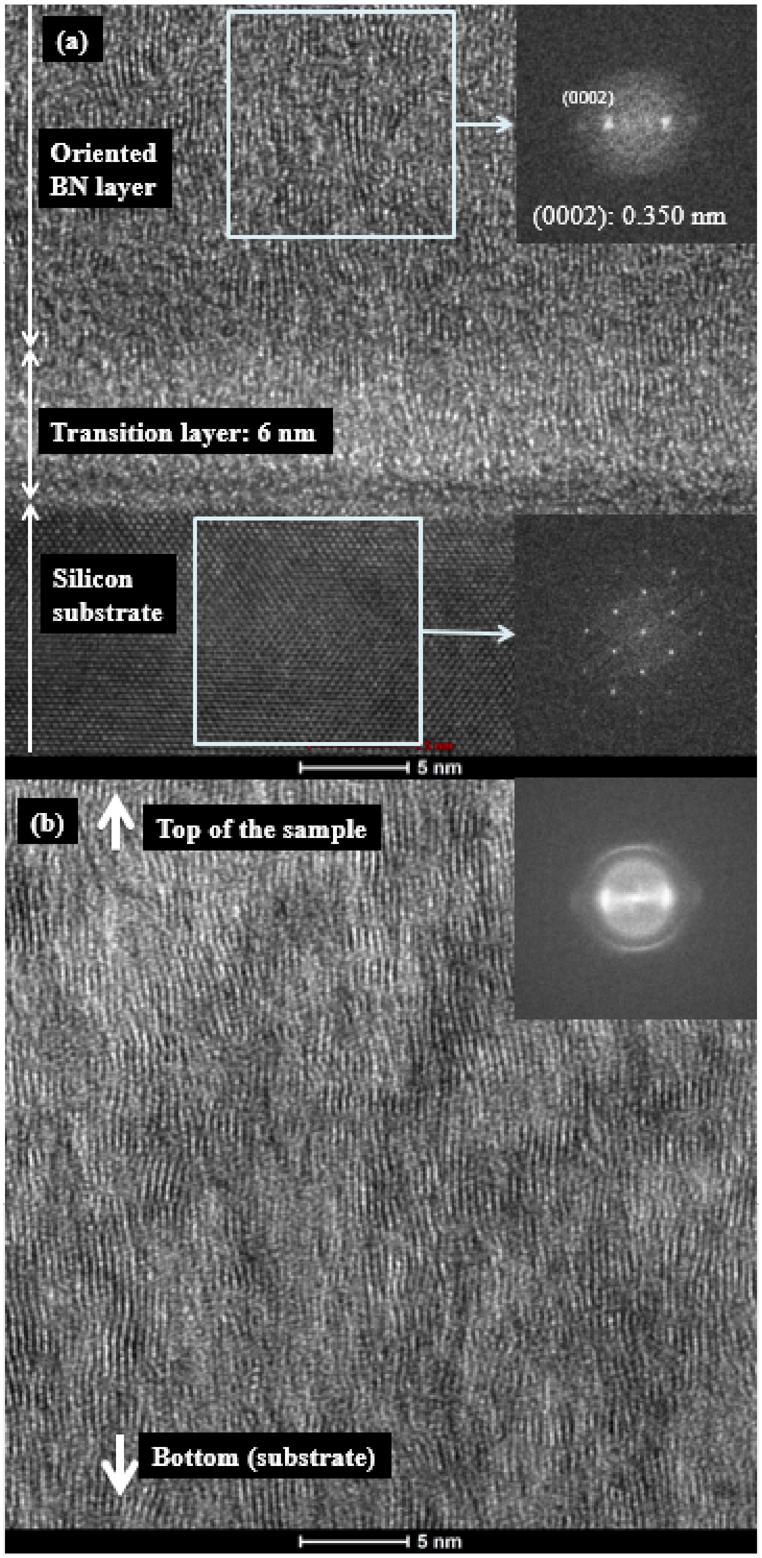

Figure 4.1 - (a) HRTEM of a BN film grown at room temperature with floating bias showing the interface between the film and silicon substrate. A transition layer of ~6 nm is located at the interface before the vertically ordered structure starts. The smooth interface implies a good film adhesion and no damage to the substrate. The top FFT shows a normal orientation along the (0002) plane, with an inter-planar distance of 0.35 nm. (b) HRTEM of the same film taken in the middle region with its FFT displaying compact partial circles, which indicates normal orientation.[21]

4.3.3 Film ordering and film stress dependency

4.3.3.1 FTIR characterization of the films

FTIR was used to quantify the film ordering. This technique has been previously extensively used for the thin film analysis[7, 22, 23] and especially for BN where the IR vibrational response can give useful information about the presence of cubic or hexagonal BN. More importantly, FTIR can resolve the different orientation of the hexagonal phase of BN. Indeed, two IR vibrations are characteristic of h-BN, one at 800 cm^{-1} which is due to the absorption of the out-of-plane bending mode of the B-N-B chain while the "main" h-BN peak located at 1380 cm^{-1} accounts for the stretch mode of the B-N bond in the plane direction. In addition, the out-of-plane ordering of h-BN also induces a "derivative-like" or two-phonon peak response[24, 25] at around 1500-1600 cm^{-1}. The IR mode located at 800 cm^{-1} is only active when the h-BN planes are oriented in the same direction as the IR beam. In FTIR, the IR beam is hitting the sample with normal incidence, meaning that the 800 cm^{-1} mode will be the most active when the h-BN basal planes are also normal to the substrate.[24-26] The ratio between the out-of-plane and in-plane IR response was computed so as to provide a way to quantify the amount of ordering in the BN film. After the FTIR raw signal was retrieved, it had to be processed so that all results are standard and can be compared with each other. The first step was to take the FTIR raw data which spans from 400 cm^{-1} to 4000 cm^{-1} (Figure 4.2a) and only select the region of interest in the spectrum (namely 780 cm^{-1} and 1380 cm^{-1}), so the raw data was truncated and the new spectrum spanned from 600 cm^{-1} to 2000 cm^{-1} (see Figure 4.2b). As the silicon substrate background is highly irregular in some places, especially the 2000 cm^{-1} region, some parts of the FTIR spectra would contain some noise and required smoothing as the noise could impact the baseline calculation (see Figure 4.2b). Once the curve has been smoothed, a baseline computed from two points taken at the extremes of the plot was subtracted in order to have a horizontal spectrum as seen in Figure 4.2c and Figure 4.2d.

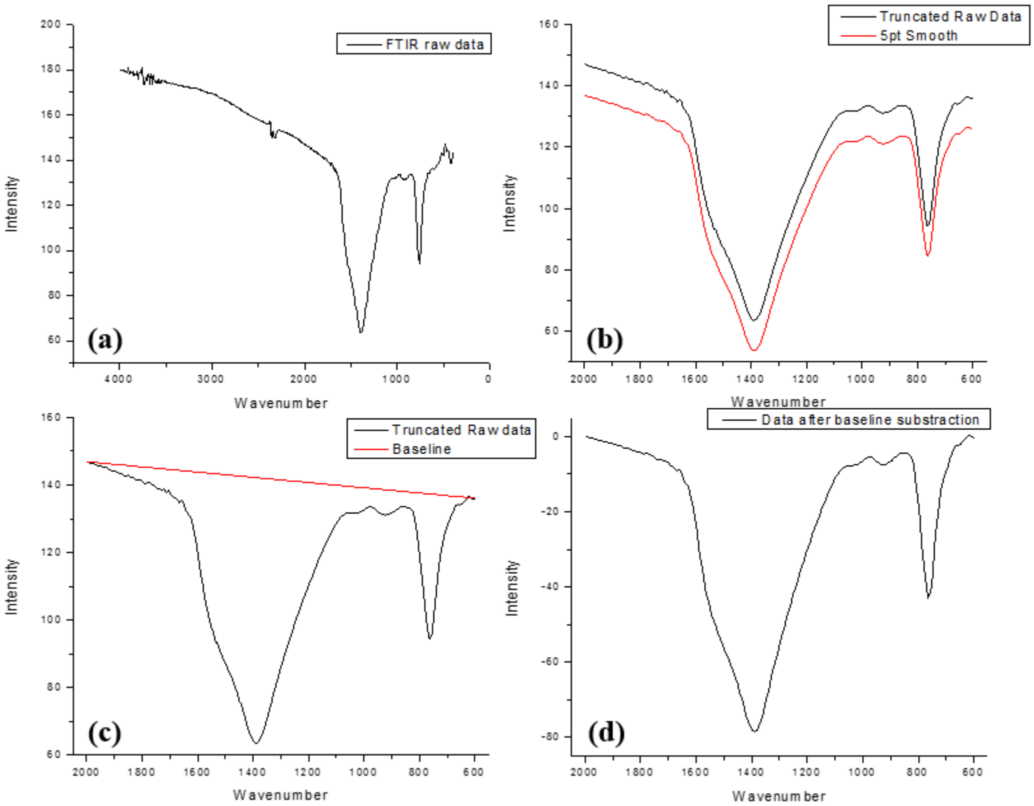

Figure 4.2 - Step by step FTIR data processing before computing the peak ratio. Inset (a) displays the raw data taken from the FTIR measurement. Inset (b) Shows the truncated data between 600 and 2000 cm-1 and the curve smoothing. Inset (c) represents the baseline computation and inset (d) is the final result after the baseline has been subtracted from the smoothed data.[21]

After processing the FTIR data as explained above, the spectrum is normalized between 0 and 1 in order to simplify the peak ratio computation as well as allowing two FTIR spectra to be compared with each other. The $R_{770/1380}$ ratio is given by equation 4.1 and its graphical interpretation can be found in Figure 4.3:

$$R_{770/1380} = \frac{1 - I_{770}}{1 - I_{1380}} = \frac{1 - I_{770}}{1} \qquad (4.1)$$

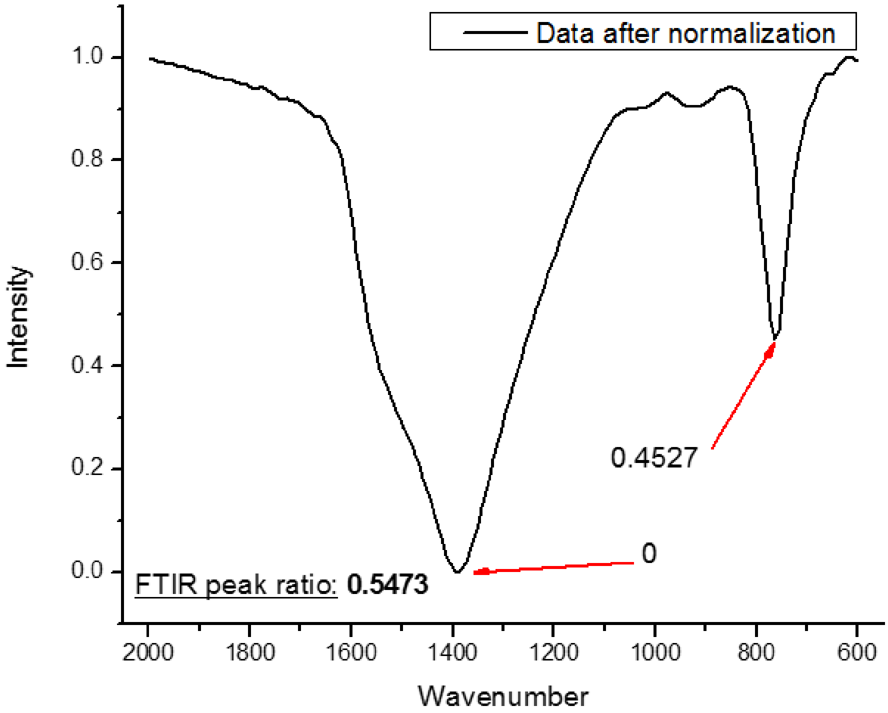

Figure 4.3 - Peak ratio computation of a FTIR spectrum for an ordered h-BN thin film. In order to facilitate the ratio computation, the spectrum is normalized between 0 and 1, making the 1380 cm-1 peak the 0 value. The ratio would then be 1-I770 where I770 is the 770 cm-1 peak intensity.[21]

There are some uncertainties in the computation of $R_{770/1380}$ and the accuracy would change by around 2%. This is due to various factors such as the data acquisition at the FTIR, the baseline computation that could change depending on which points are used. The FTIR spectrum of a *voBN* thin film was compared to other spectra of samples containing cubic BN and turbostratic BN (c-BN/t-BN), and h-BN powder. The results are shown in Figure 4.4 and the cubic content a_{cBN} in the c-BN/t-BN sample was deduced from a direct computation of the ratio between the peak intensity of the cubic response and the main h-BN response, as shown in equation 4.2:[22, 27]

$$a_{cBN} = \frac{I_c}{I_c + I_h} \qquad (4.2)$$

I_c is the maximum c-BN peak intensity located at 1080 cm^{-1} and I_h is the maximum in-plane h-BN peak intensity located at 1380 cm^{-1}. Using equation 4.2 on the FTIR spectrum of c-BN/t-BN, the c-BN content is computed to be 20%. In the case of the *voBN* and h-BN powder spectra, no peak at 1080 cm^{-1} could be found, confirming the absence of c-BN in those two samples. The presence of a broad peak in the area of 1400 cm^{-1} as well as a strong absorption response at 800 cm^{-1} is a typical FTIR response for *voBN*, while the h-BN powder only exhibits a sharp peak at 1380 cm^{-1} and a very small response at 800 cm^{-1}. Using equation 4.1, the out-of-plane to in-plane peak ratio for the *voBN* sample grown at room temperature with a grounded substrate is 0.51. In comparison, the c-BN/t-BN sample and h-BN powder have a much lower peak ratio, with a value of respectively 0.19 and 0.29.

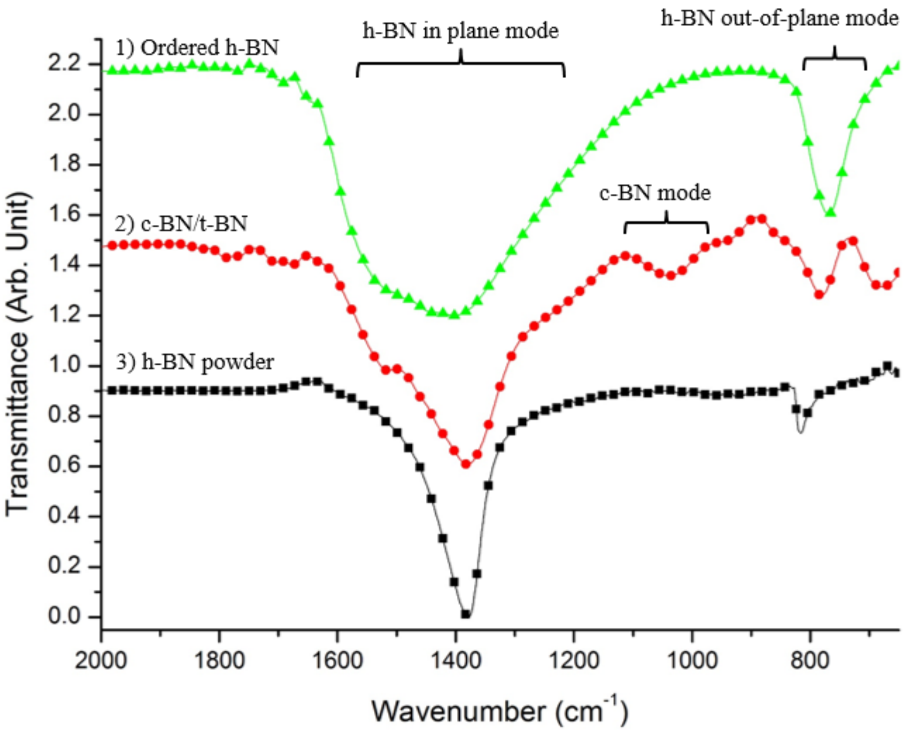

Figure 4.4 - FTIR spectra of BN samples. The h-BN powder is a high purity powder made of 10 µm particles. The c-BN/t-BN film was grown with HiPIMS at 500 degC, 0 V substrate, and peak power density of 200W.cm^{-2}. The ordered h-BN sample was grown with HiPIMS at room temperature and 60 W.cm^{-2} peak power density. The computed $R_{770/1380}$ peak ratio for ordered h-BN, c-BN/t-BN and h-BN powder is respectively 0.51, 0.19 and 0.29.[21]

4.3.3.2 Film stress and impact on nanostructure

In Figure 4.5a, the FTIR peak ratio and film stress were plotted against the negative substrate bias. As the substrate bias during growth is increased, both the compressive stress and FTIR peak ratio are showing a downward trend, implying that both could be correlated. Such correlation means that the amount of vertical alignment in the film is directly related to the amount of compressive stress. It can be noticed that the FTIR peak ratio at a bias of -75 V is slightly higher (which would be going against the trend) and it is most likely due to the FTIR raw data processing (especially baseline fitting) that could introduce a small error in peak ratio value, as explained above. In Figure 4.5b, the effect of temperature on the compressive is shown, with a decrease in stress with an increase of temperature at constant substrate bias.

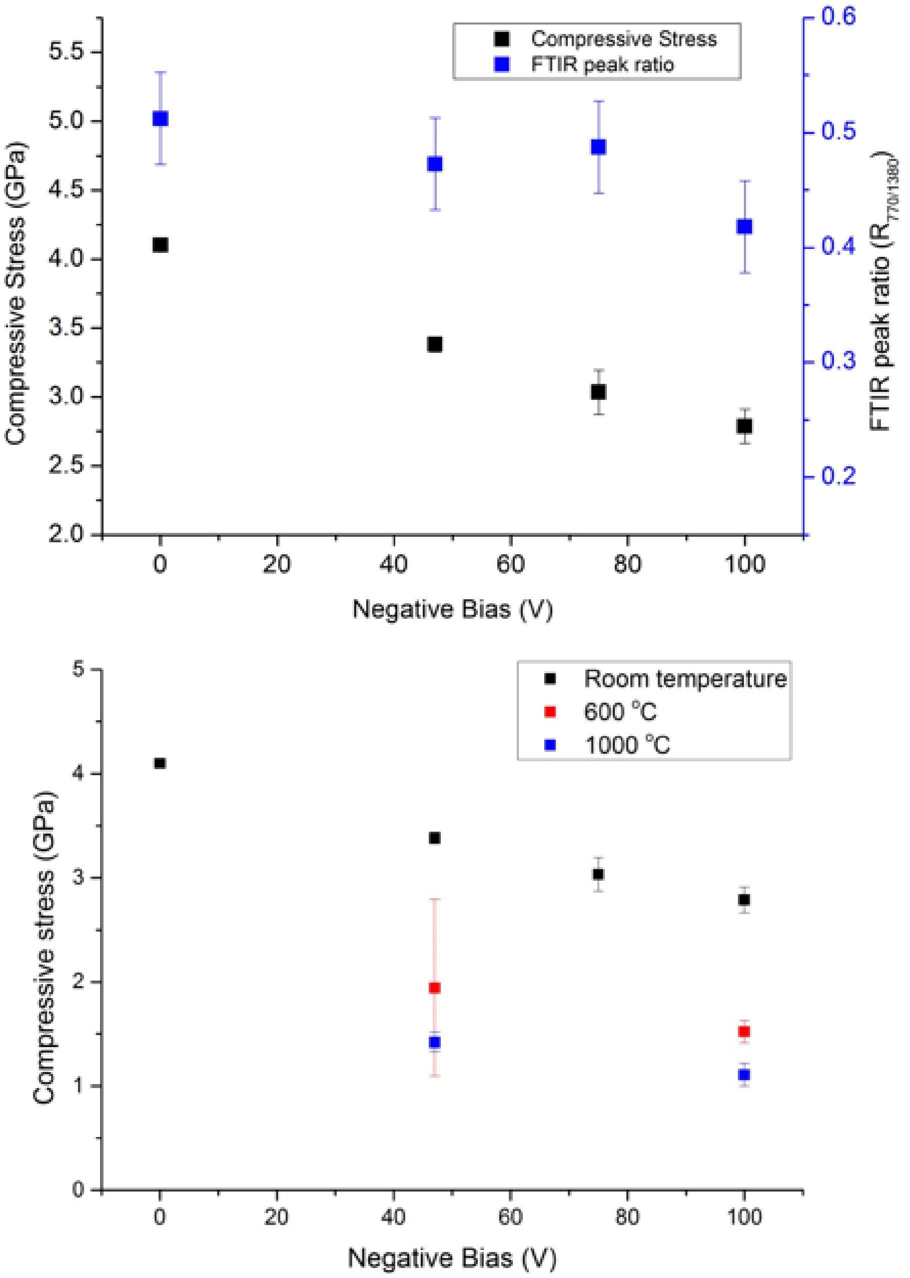

Figure 4.5 - Top: Film stress in function of the applied bias voltage and the FTIR peak intensity ratio between the in-plane response at 1380 cm^{-1} and the out-of-plane response located at 770 cm^{-1}. Bottom: Compressive stress value for films grown at different temperatures and bias. The lowest bias is 0 when the substrate holder is connected to the ground. The value at -47 V is the floating bias.[21]

As seen and deduced from Figure 4.5, two competing effects contribute to the growth mechanism of *voBN*: ion energy (via the substrate bias) and temperature. Increasing the temperature would increase the ion mobility at the substrate, which would shift the equilibrium of the hexagonal/cubic BN phase towards higher pressures (see chapter 2 for more details).[28] Here, no planar h-BN could be obtained even at 1000 degC as there would still be too much ion energy in the plasma to lower the stress enough and instead *voBN* would be the preferred micro structural formation. A way to lower the stress even more would be to increase the voltage bias at the substrate (as shown in the top plot of Figure 4.5), so that the stress would be low enough to get planar h-BN. However, any attempt at growing BN with a bias above -100 V failed due to the emergence of electrical breakdowns. Indeed, as BN is deposited on the substrate (and substrate holder), it would act as a thin dielectric layer, sandwiched on one side by the negatively charged substrate holder and silicon wafer, and on the other side by the plasma mostly made of positively charged B, N and La ions. During growth, charges on both sides would build up until they reach a critical point leading to an electrical breakdown, destroying the BN thin film in the process.

4.3.4 Compressive stress theory for HiPIMS growth

As seen in the previous section, the experimental results have shown a correlation between the ion energy, the film ordering and the residual compressive stress in the BN thin film. Figure 4.5 displays a decreasing compressive stress with increasing ion energy, which is contradictory with what has been found with carbon, which increases to a maximum for a certain ion energy (around 100 eV) before decreasing again.[29] For carbon, the curve for the compressive stress σ can be represented by equation 4.3 as suggested by McKenzie et al.:[11]

$$\sigma \propto \frac{\sqrt{E}}{\frac{R}{j}+kE^{\frac{5}{3}}} \qquad (4.3)$$

The coefficient $k=0.016\rho E_0^{-5/3}$. In addition, j is the ion flux, E is the ion energy, and ρ , E_0 and R are parameters related to the material properties. From equation 4.3, it can be seen that there are three different regions of stress depending on the ion energy E . Low values of E would not impact the film structure much and just bounce off the sample, resulting in a low stressed film. Increasing the incident ion energy will produce a film with high stress as impacting ions are penetrating the film surface and increase the film density. Increasing E further would be detrimental to the film stress as such high energies would increase the re-sputtering effect: the ions impact the film surface with too much energy, which would either rip off more ions away from the film structure or displace the atoms so much they would end up relaxing the crystal structure instead of straining it more. Based on the stress curve shape seen in figure 4.5a, it seems that the growth of BN with LaB_6 produces ion energies high enough to move the compressive stress in the last part of the curve where there is a decrease of stress with increasing ion energy, as described in figure 4.6. As such, equation 4.3 can be approximated as equation 4.4 when E is large enough:

$$\sigma \propto \frac{1}{k E^{\frac{7}{6}}} (4.4) \qquad (4.4)$$

When fitting the experimental data with the curve obtained from equation 4.4, a k of $3.73.10^{-4}$ and E of 259 eV was found. The average energy distribution of 259 eV for the plasma in HiPIMS is high and noticeably higher than other highly energetic deposition methods such as PLD and FCVA. The literature about high energy sputtering of LaB_6 suggests ion energies for boron as high as 750 eV, mostly due to the high energy boron self-sputtering as well as backscattering of boron ions on lanthanum ions contained in the target.[15] Such high ion energy would impact the computed average ion energy and even though La ions play an important role in the high ion energy reading, it is not yet fully understood to draw a definitive conclusion on the matter. For instance, the carbon growth via FCVA has an average ion energy of around 20 eV,[30] and this value is located in the first area of the curve, where the stress increases with increasing ion energy, meaning that bias voltage can be used to increase stress and generate high density amorphous carbon film, such as ta-C for instance.

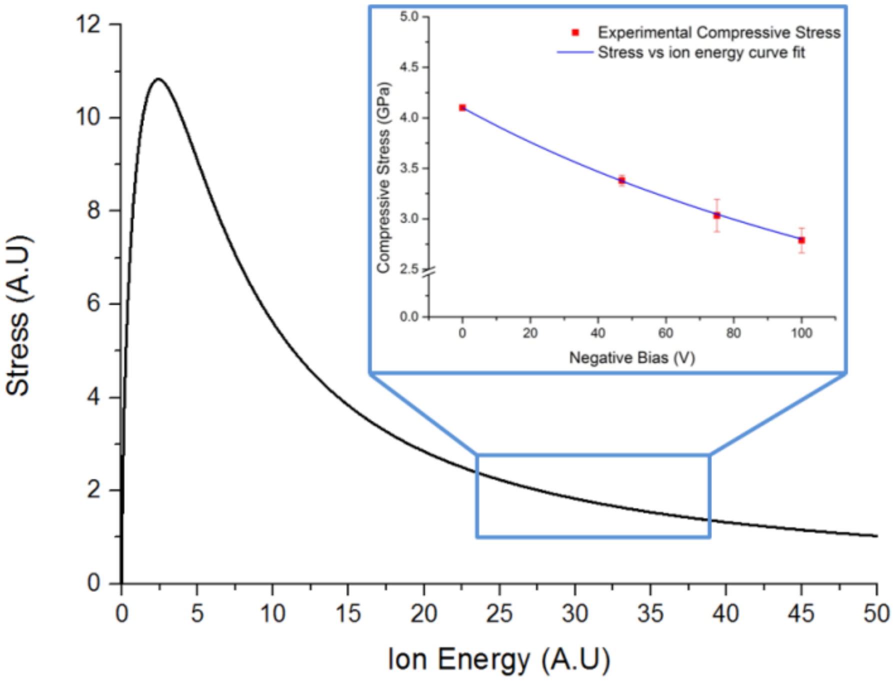

Figure 4.6 - Curve plotted from the stress curve formula given by McKenzie depicting the compressive stress depending on the ion energy for carbon. Assuming a similar curve distribution for boron nitride, the current results are located at the high ion energy portion as shown in the inset, displaying the computed compressive stress for ordered h-BN films grown at room temperature.[21]

In the case of HiPIMS, the generated plasma from the LaB_6 target is a result of the high current pulses, allowing a phase change from the amorphous BN structure to the hexagonal one. The HiPIMS discharge of LaB_6 generates two distinct types of B+ ions: a high density B^+ plasma with an average energy comprised between 1 eV and 5 eV, followed by a B^+ plasma with a large energy spread extending in the tens of eV.[14, 15] In addition to the ionization of the boron atoms, the sputtering of LaB_6 using the HiPIMS discharge mode, produces a plasma made of highly energetic $La^+/La^{2+}/La^{3+}$ ions, with energies extending in the several hundred of eV.[15] Combined with their heavy nature, it is suspected that those La atoms impact the thin film with sufficient energy to induce momentum transfer processes, such as recoil implantation, defect creation, resputtering or desorption.[40] During the BN growth with HiPIMS, La ions may lead to a change in stress through those momentum transfer processes, by either increasing the tensile stress or increasing the compressive stress. The correlation between ion energy and stress was experimentally observed and increase of ion energy (by increasing the DC bias voltage, see Figure 4.5) will decrease the compressive stress. However, not enough experimental data was available to conclude that the stress reduction observed is mostly driven by La ions instead of the B ions. In addition, even without any DC bias, the ion energy in the plasma has enough energy to lower the compressive stress sufficiently to avoid the maximum stress peak observed in the case of carbon growth with FCVA, yet there is no available data to conclude the extend of La ions' role in the observed result.

4.3.5 c-BN nanocrystals seeds for t-BN

Some cubic BN nanocrystals were obtained when increasing the peak power density to 200 W.cm^{-2}, with a bias voltage of -200 V and a growth temperature of 500 degC. The c-BN nanocrystals were 5 nm in size, and are embedded in a matrix of amorphous and turbostratic BN as shown in Figure 4.7.

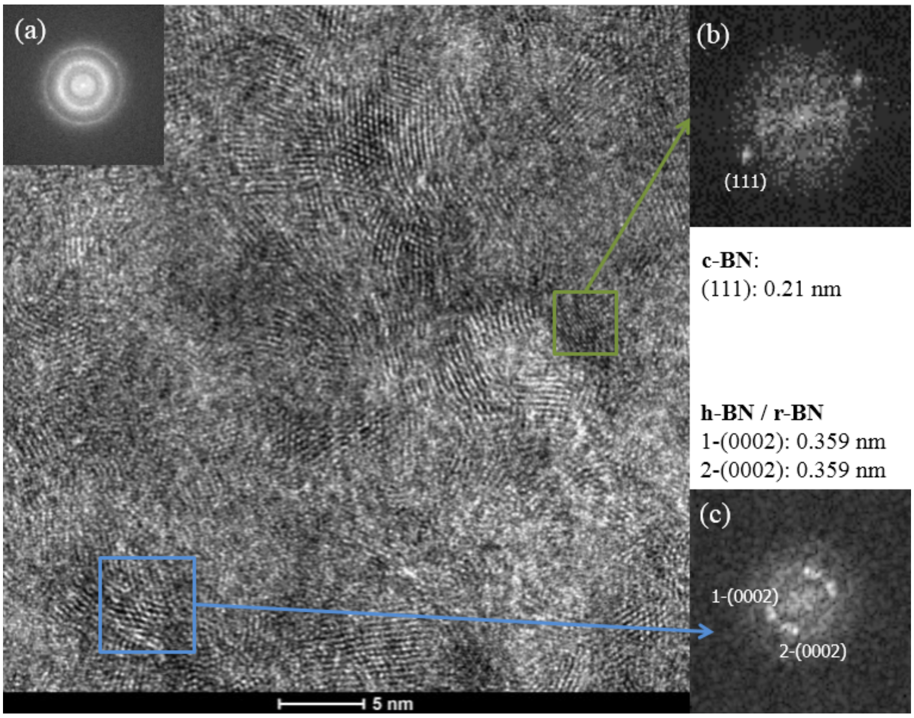

Figure 4.7 - HRTEM of a BN film deposited with a bias of -200 V at 600 degC and a HiPIMS maximum power density of 200 W.cm^{-2}. The film is highly disordered, with c-BN nanocrystals of 5 nm, embedded in a matrix of turbostratic sp^2 BN made of the hexagonal and/or rhombohedral structure. (a) is the FFT of the whole image, displaying the characteristic rings for turbostratic BN: the inner (0.36 nm/cycle) and outer (0.21 nm/cycle) rings are induced respectively by the random orientation of the h-BN (0002) and c-BN (111) configurations. (b) and (c) are respectively the FFT of the green (top) zone containing c-BN and the blue (bottom) zone made of h-BN/r-BN.[21]

The c-BN nanocrystals where further characterized using a XRD 2θ scan (Figure 4.8). Both XRD peaks corresponding to c-BN [111] and h-BN [101] are detected and by fitting them with Gaussian curves, a grain size of 10 nm was roughly calculated, which is in correlation with the TEM image shown in Figure 4.7.

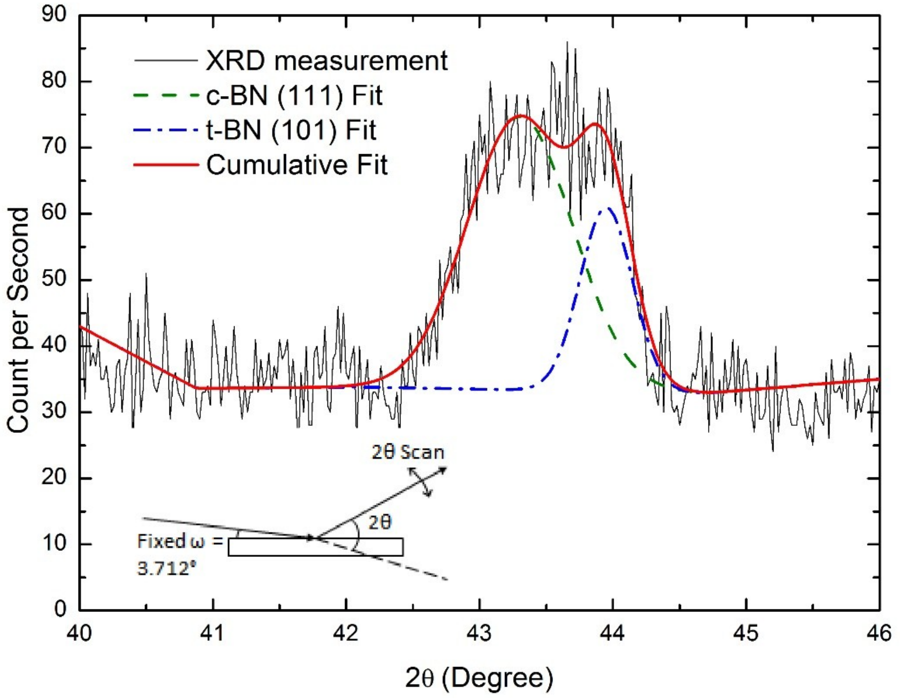

Figure 4.8 - 2θ scan of c-BN/t-BN sample with ω fixed at 3.712°. 2 Gaussian curves are used to fit the graph, which is contributed by c-BN (111) and h-BN (101) respectively. The fixed ω is determined by rocking curve scan on the c-BN/t-BN sample at various phi angles to detect the (111) plane of c-BN at 2θ of 43.314°. A weak peak is detected at ω of 3.712° for the rocking curve scan.[21]

The (111) plane of the cubic BN nanocrystals acts as a perfect surface for the growth of h-BN in the (002) direction. Indeed, both c-BN (111) and h-BN (002) are lattice matched when the hexagonal basal planes are oriented at a 45 degree angle, as shown in Figure 4.9.

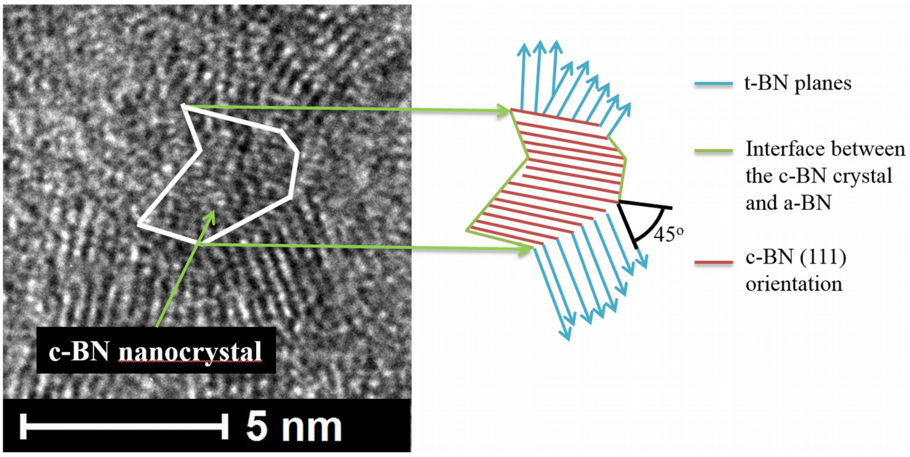

Figure 4.9 - Cross-section TEM image of a c-BN nanocrystal and its interface with t-BN and amorphous BN. The c-BN crystal induces changes in the film morphology at the nanoscale due to the change in orientation between the cubic and hexagonal phases. The t-BN planes will preferentially orientate themselves such that the lattice mismatch is minimized, i.e. 45°.

In the case of a BN growth where the cubic phase is absent, the hexagonal BN planes order themselves in the direction that would minimize the Gibbs free energy. In this case, the driver for basal plane ordering is the biaxial compressive stress seen across the whole substrate.[11] In the end, a t-BN thin film is a particular case of *voBN* where the c-BN nanocrystals disrupt the vertical ordering and randomize the h-BN plane orientation.

Additional XRD scans were performed in the case of a pure *voBN* thin film and the results are shown in Figure 4.10. The inset (a) shows a peak at 26.6° which is attributed to the crystal plane (002) of h-BN. Inset (b), which is the rocking curve measurement, shows a sharp peak at $\theta = 13.35^{o}$ which indicates a high ordering in the (002) direction.

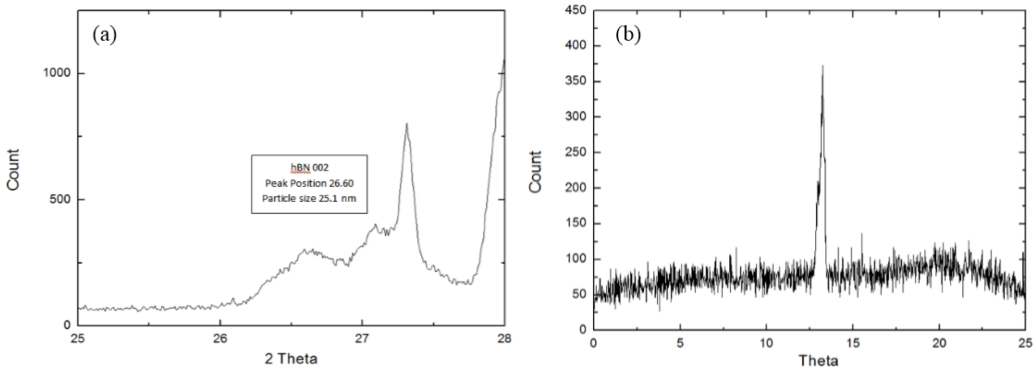

Figure 4.10 - XRD results for the vertically ordered h-BN film. (a) shows the XRD response for the sample. The particle size was computed using a Gaussian fitting of the curve and applying Scherrer equation. (b) is the rocking curve, showing a sharp peak indicating the 002 plane is highly oriented.[21]

Using Bragg's law as shown in equation 4.5 below, the inter-plane distance between two h-BN basal planes can be resolved:

$$d = \frac{\lambda}{2 \sin \theta} \qquad (4.5)$$

Where d is the distance between two h-BN planes, λ is the wavelength used for the XRD scan which is 0.1542 nm here, and $\theta = 13.35^{o}$ according to Figure 4.10b.

Using those values, we get $d = 3.339$ nm which indeed is the expected inter-plane distance between to basal planes in h-BN.

4.3.6 Lanthanum content in the film

The side effect of using an LaB_6 target is that the obtained thin films are contaminated with lanthanum. Figure 4.11 inset a, b and c are the EELS response from B, N and La respectively. When looking at figure 4.11a, the electron transition response of type π* is greater than the σ*, confirming the full sp^2 hybridization of the *voBN* thin film. Figure 4.11d provides the ratio between B, N and La and shows is remains constant across the thin film (see Figure 4.11e) with a ratio of approximately 0.4:0.5:0.1. The ratio between B and N is around 1.15, and the La content is in the 5-10 at.% region. The thin film was confirmed to be homogeneous, with no aggregation of one species in certain areas. It seems that the La atoms occupy some of the B vacancies in the h-BN atomic structure as the ratio between La+B and N is the same.

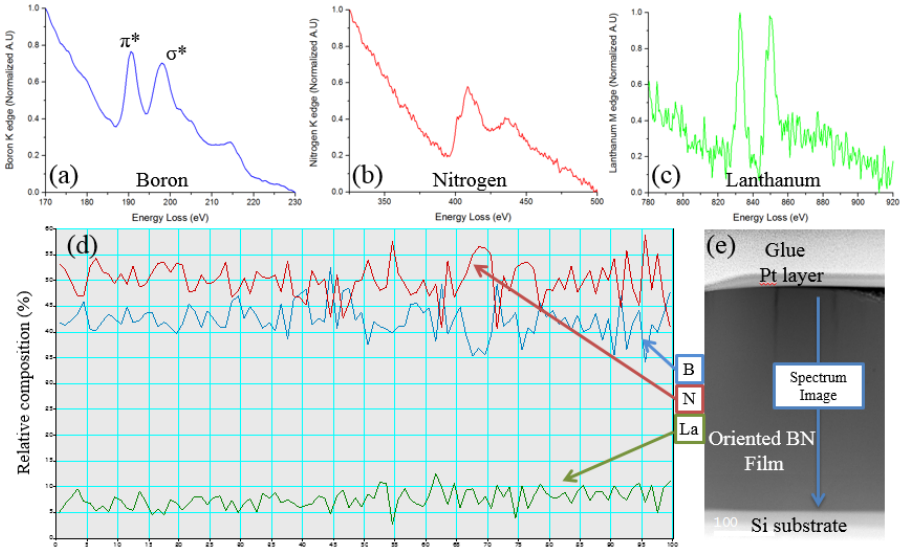

Figure 4.11 - Measurement of the relative atomic % composition of the film using EELS. (a), (b) and (c) respectively show the EELS spectra of B, N and La. (d) Computed atomic concentration of boron (blue), nitrogen (red) and lanthanum (green). The ratio of B and N indicates a BN film stoichiometry of 1.15. The lanthanum content is constant at around 7.5 at.%. The measurement is made along the whole film as shown in (e).[21]

As LaB_6 is conductive, some electrical characterization was performed to verify BN films containing La would retain their insulative property. A 4-point probe measurement was performed but no results could be derived from it as the film resistivity is too high to get an I-V curve. This is due to the equal or greater resistivity of the *voBN* film compared to the prober system's own impedance which is in the order of 10^{16} Ω.cm. This measurement, even though lacking an actual value, shows that the BN thin films are still electrically resistive even with 10 at.% La inside the film. In addition, the ratio between La and B measured in the film is around 1:12, which is half from what can be found in the target (1:6). This is due to the different ionization energies of B atoms and La atoms (it is easier to ionize boron). Oks and Anders have shown that the ratio of ionized B to ionized La in the plasma is directly correlated to the peak power density,[14] where an increase of the latter would increase the relative content of B in the plasma.

4.3.7 Impact of the gas ratio on *voBN* growth

The amount of nitrogen gas injected during the growth was investigated, and the resulting film structure was characterized with FTIR. Figure 4.12 shows the various spectra obtained with gas ratios between nitrogen and argon of 5%, 10% and 25%. It can be observed that an increase of nitrogen gas in the plasma discharge is correlated with a shift of the main h-BN peak at 1380 cm^{-1} towards higher wavenumbers, with the maximum value of around 1400 cm^{-1} reached for 25% of N_2 gas. This shift is a good indicator to the quality of the h-BN film, where a low value means low quality, where the film would mostly be made of BN soot (soot has a peak centred at around 1330 cm^{-1}). Increasing the quality of the film would shift the peak towards higher wavenumber values due to the h-BN peak being located at 1370 cm^{-1}, and in the particular case of *voBN*, the additional "derivative-like" bump in the 1400-1500 cm^{-1}

that will also contribute to the shift. In a similar fashion, the out-of-plane h-BN FTIR response at 780 cm^{-1} is affected by the nitrogen gas ratio during growth, where the peak intensity would increase with a higher nitrogen gas ratio. Finally, using a higher nitrogen gas ratio only marginally improved the film quality (higher peak intensity at 780 cm^{-1} and a shift toward higher wavenumber for the main h-BN peak) while making the plasma more unstable. Indeed, nitrogen gas is more difficult to ionize and the pulses of current generated in HiPIMS mode tend to destabilize the plasma discharge so 25% nitrogen gas ratio was found to be the optimum value, where the film quality would be good while having a stable plasma to work with.

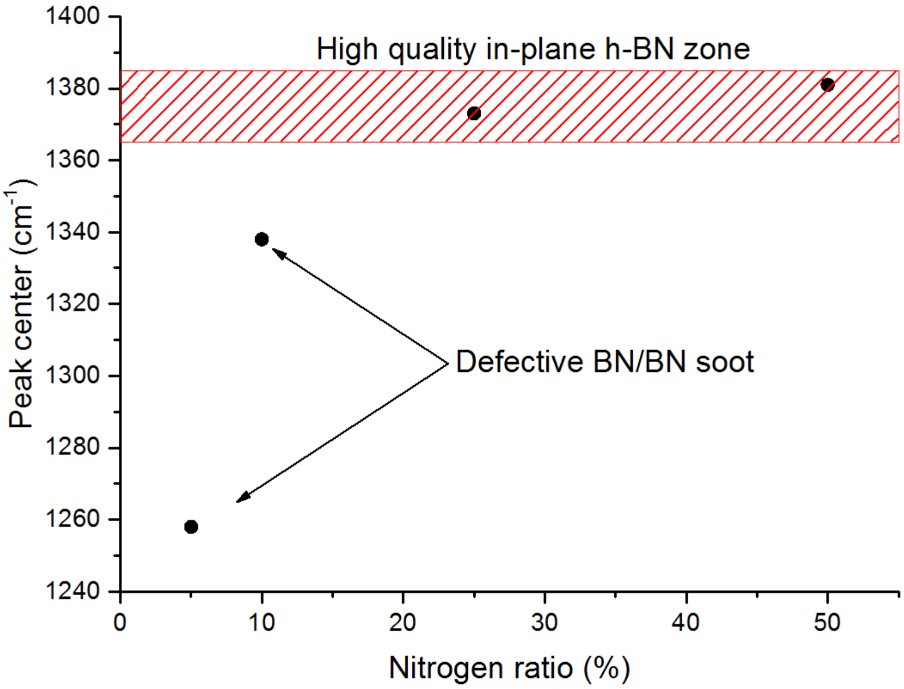

Figure 4.12 - In-plane h-BN FTIR peak centre depending on the nitrogen content during thin film growth. The zone represents the area for which the peaks indicate high quality h-BN crystals. Above values of 25% nitrogen content, h-BN of high quality is consistently obtained.

4.3.8 Cross-plane thermal conductivity of *voBN*

Both c-BN/t-BN and *voBN* samples where measured, to compare the impact of the nanostructure on the thermal conductivity. The c-BN/t-BN sample is made of 20% of the cubic phase and 80% of the amorphous/turbostratic phase as estimated by the FTIR measurements previously performed. TDTR was performed on both samples to measure the cross-plane (along the c axis) thermal conductivity and it was found that *voBN* shows a thermal conductivity at room temperature of 5.1 W m^{-1} K^{-1} while the other c-BN/t-BN sample is only 1.7 W m^{-1} K^{-1}. In comparison, bulk h-BN along the basal planes has a thermal conductivity around 80 times greater than *voBN* at 390 W m^{-1} K^{-1}.[31, 32] This could be due to the grain size in the *voBN* thin film which is only 10 nm (from TEM and XRD measurements). Indeed, it was previously reported that Si nanotubes with the same dimensions would be similarly affected,[33] and that it could be attributed to the increased phonon scattering caused by the greater amount of grain boundaries in the material. In the case of the c-BN/t-BN sample, the thermal conductivity comes close to that of amorphous materials due to its defective structure unable to propagate phonons efficiently.[34] Figure 4.13 summarizes the different thermal conductivities for some materials and shows that *voBN*'s thermal conductivity is as high as that of NCG grown at 300 degC,[1] four times higher than SiO_2 and up to 10 times higher than the electrically resistive filler used for encapsulating the electronically active parts in a circuit. This suggests a possible use of *voBN* in electronics as a passivating layer capable of extracting heat at the same time. It has to be noted that in order to be able to properly compare the results summarized in Figure 4.13, all reported results were obtained using the same measurement method (i.e. a method based on thermoreflectance). As such, the consistency in the measurement method warrants a direct comparison of the results, even though they were not performed by the same research group.

Material	**Thermal conductivity at 300K ($W.m^{-1}.K^{-1}$)**	**Resistivity (Ω.cm)**	**Growth parameters**
Random tr-BN/c-BN	1.7[†]	-	HiPIMS, 500°C, a few hundred nm thick
Ordered h-BN (along c-axis)	5.1[†]	~10^{16}[†]	HiPIMS, <50°C, 400 nm thick
Textured carbon (along c-axis – deposited at 300°C)[35]	5.32[1]	~10	FCVA, 300°C, max thickness <500 nm
Textured carbon (along c-axis – deposited at 400°C)[35]	16.72[1]	~10	FCVA, 400°C, max thickness <500 nm
SiO_2 for electronic devices	1.27[36]	10^{16}	Dry/wet oxidation, 600-1200°C

[†] Measured in this work

Figure 4.13 - Table summarizing the thermal conductivity of various amorphous materials such as BN, as well as textured carbon which is similar in structure to ordered h-BN.[21]

4.4 Conclusion

This chapter reports the first successful attempt at growing *voBN* as well as its first characterization via HRTEM and FTIR for the microstructure, as well as thermally with TDTR. A completely new method to grow BN was used, based on HiPIMS with a LaB_6 target in nitrogen gas. Using a peak power density ranging from 20 $W.cm^{-2}$ up to 100 $W.cm^{-2}$, the microstructure of the BN film would orientate itself vertically. In addition to its capability of growing large area BN, the new BN deposition method described here is capable of fairly high growth rates (in comparison to other growth methods of BN) of up to tens of nm per minute, while keeping the chamber conditions at room temperature, unlike other dielectric materials with high thermal conductivity such as diamond and c-BN which require temperatures of at least 350 degC.[37] In addition, *voBN* interfaces well with the silicon substrate and its surface roughness was computed to be below 1 nm RMS from AFM scans. Such properties allow potential applications for electronics where flatness is paramount for high quality production, while the high thermal conductivity of *voBN* in the through-film direction could be used to improve the heat extraction on devices plagued performance degradation due to overheating issues.[38, 39]

4.5 References

1. M. Shakerzadeh, M. K. Samani, N. Khosravian, E. H. T. Teo, M. Bosman and B. K. Tay, *Carbon*, 2012, **50**, 1428-1431.
2. M. Shakerzadeh, N. Xu, M. Bosman, B. K. Tay, X. Wang, E. H. T. Teo, H. Zheng and H. Yu, *Carbon*, 2011, **49**, 1018-1024.
3. D. W. M. Lau, A. Moafi, M. B. Taylor, J. G. Partridge, D. G. McCulloch, R. C. Powles and D. R. McKenzie, *Carbon*, 2009, **47**, 3263-3270.
4. D. W. M. Lau, D. G. McCulloch, M. B. Taylor, J. G. Partridge, D. R. McKenzie, N. A. Marks, E. H. T. Teo and B. K. Tay, *Physical Review Letters*, 2008, **100**, 176101.
5. J. Thomas, N. E. Weston and T. E. O'Connor, *J. Am. Chem. Soc.*, 1962, **84**, 4619-4622.
6. I. S. Gladkaya, G. N. Kremkova and V. N. Slesarev, *Journal of the Less Common Metals*, 1986, **117**, 241-245.
7. X. W. Zhang, H. G. Boyen, H. Yin, P. Ziemann and F. Banhart, *Diamond Relat. Mater.*, 2005, **14**, 1474-1481.
8. E. J. M. Hamilton, S. E. Dolan, C. M. Mann, H. O. Colijn, C. A. McDonald and S. G. Shore, *Science*, 1993, **260**, 659-661.
9. S. Alkoy, C. Toy, T. Gönül and A. Tekin, *J. Eur. Ceram. Soc.*, 1997, **17**, 1415-1422.
10. V. Kouznetsov, K. Macák, J. M. Schneider, U. Helmersson and I. Petrov, *Surf. Coat. Technol.*, 1999, **122**, 290-293.
11. D. R. McKenzie, W. D. McFall, W. G. Sainty, C. A. Davis and R. E. Collins, *Diamond Relat. Mater.*, 1993, **2**, 970-976.
12. D. R. McKenzie, *Journal of Vacuum Science & Technology B: Microelectronics and Nanometer Structures*, 1993, **11**, 1928.
13. E. H. T. Teo, J. Kulik, Y. Kauffmann, R. Kalish and Y. Lifshitz, *Appl. Phys. Lett.*, 2011, **98**.
14. E. M. Oks and A. Anders, *J. Appl. Phys.*, 2012, **112**, 086103.
15. R. Franz, C. Clavero, R. Bolat, R. Mendelsberg and A. Anders, Plasma Sources Sci. Technol., 2014, 23, 035001.
16. K. Kang, Y. K. Koh, C. Chiritescu, X. Zheng and D. G. Cahill, *Rev. Sci. Instrum.*, 2008, **79**, 114901.
17. Y. K. Koh, M. H. Bae, D. G. Cahill and E. Pop, *Nano Lett*, 2010, **10**, 4363-4368.
18. C. Chiritescu, D. G. Cahill, N. Nguyen, D. Johnson, A. Bodapati, P. Keblinski and P. Zschack, *Science*, 2007, **315**, 351-353.
19. Y. K. Koh, Y. Cao, D. G. Cahill and D. Jena, *Advanced Functional Materials*, 2009, **19**, 610-615.
20. D. G. Cahill, *Rev. Sci. Instrum.*, 2004, **75**, 5119-5122.
21. O. Cometto, B. Sun, S. H. Tsang, X. Huang, Y. K. Koh and E. H. Teo, *Nanoscale*, 2015, **7**, 18984-18991.
22. P. B. Mirkarimi, K. F. McCarty and D. L. Medlin, *Materials Science and Engineering: R: Reports*, 1997, **21**, 47-100.
23. Y. Shi, C. Hamsen, X. Jia, K. K. Kim, A. Reina, M. Hofmann, A. L. Hsu, K. Zhang, H. Li, Z.-Y. Juang, M. S. Dresselhaus, L.-J. Li and J. Kong, *Nano Letters*, 2010, **10**, 4134-4139.
24. T. A. Friedmann, K. F. McCarty, E. J. Klaus, J. C. Barbour, W. M. Clift, H. A. Johnsen, D. L. Medlin, M. J. Mills and D. K. Ottesen, *Thin Solid Films*, 1994, **237**, 48-56.
25. R. Geick, C. H. Perry and G. Rupprecht, *Physical Review*, 1966, **146**, 543-547.
26. W. Dworschak, K. Jung and H. Ehrhardt, *Thin Solid Films*, 1995, **254**, 65-74.
27. A. Schütze, K. Bewilogua, H. Lüthje, S. Kouptsidis and S. Jäger, *Surf. Coat. Technol.*, 1995, **74-75**, 717-722.
28. V. L. Solozhenko, V. Z. Turkevich and W. B. Holzapfel, *The Journal of Physical Chemistry B*, 1999, **103**, 2903-2905.

29. D. R. McKenzie, D. Muller and B. A. Pailthorpe, *Phys. Rev. Lett.*, 1991, **67**, 773-776.
30. M. Shakerzadeh, E. H. T. Teo, A. Sorkin, M. Bosman, B. K. Tay and H. Su, *Carbon*, 2011, **49**, 1733-1744.
31. E. K. Sichel, R. E. Miller, M. S. Abrahams and C. J. Buiocchi, *Phys Rev B*, 1976, **13**, 4607-4611.
32. I. Jo, M. T. Pettes, J. Kim, K. Watanabe, T. Taniguchi, Z. Yao and L. Shi, *Nano Letters*, 2013, **13**, 550-554.
33. M. C. Wingert, S. Kwon, M. Hu, D. Poulikakos, J. Xiang and R. K. Chen, *Nano Letters*, 2015, **15**, 2605-2611.
34. D. G. Cahill, S. K. Watson and R. O. Pohl, *Phys Rev B*, 1992, **46**, 6131-6140.
35. M. Shakerzadeh, G. C. Loh, N. Xu, W. L. Chow, C. W. Tan, C. Lu, R. C. C. Yap, D. Tan, S. H. Tsang, E. H. T. Teo and B. K. Tay, *Adv. Mater.*, 2012, **24**, 4112-4123.
36. M. G. Burzo, P. L. Komarov and P. E. Raad, *Components and Packaging Technologies, IEEE Transactions on*, 2003, **26**, 80-88.
37. A. Soltani, A. Talbi, V. Mortet, A. BenMoussa, W. J. Zhang, J. C. Gerbedoen, J. C. De Jaeger, A. Gokarna, K. Haenen and P. Wagner, *AIP Conference Proceedings*, 2010, **1292**, 191-196.
38. C. Sukwon, E. R. Heller, D. Dorsey, R. Vetury and S. Graham, *Electron Devices, IEEE Transactions on*, 2013, **60**, 159-162.
39. A. Pérez-Tomás, A. Fontserè, M. Placidi, N. Baron, S. Chenot, J. C. Moreno and Y. Cordier, *Semicond. Sci. Technol.*, 2012, **27**, 125010.
40. D. M. Mattox, Journal of Vacuum Science & Technology A: Vacuum, Surfaces, and Films, 1989, 7, 1105.

Chapter 5 – The anisotropic thermal conductivity of vertically ordered Boron Nitride

5.1 Introduction

5.1.1 Rationale

The race toward faster and more powerful electronics, combined with a trend to miniaturize further each generation of electronic chips has raised the issue of overheating circuits. In particular, the active electronic region has been effected by overheating due to thermal crosstalk: the neighboring hot spots are exchanging heat with each other instead, inducing a spiraling heating effect. Overheating of electronics can be dangerous and cause drops in performance as well as ultimately cause a device failure.[1, 2] Over the past decade, the active hot spot regions have shrunk to sub micrometre scales, urging to look for novel materials with interesting thermal properties in order to cope with the increasing thermal load. For instance, materials with anisotropic thermal conductivity have been prospected[3] and most of the focus was on materials with a high thermal conductivity in the planar direction compared to the through plane direction (graphene,[4] hexagonal BN[5] or multi-layered thin-films[6]). Unfortunately, those materials promote in-plane heat spreading, which would contribute to the thermal crosstalk instead of preventing it. On the other hand nanomaterials with high thermal anisotropy in the through-plane direction such as vertically aligned nanotubes[7] seem to improve the thermal issues by extracting the heat vertically.[8] In particular, Boron Nitride Nanotubes or BNNTs are an excellent example, when combined with their electrically insulative property,[8-10] could offer a solution by being placed directly on top of the hot spot. Unfortunately, synthesis of such nanotubes requires high temperatures,[11-13] and are limited to small areas only. As previously shown and explained in chapter 2, NCG with vertical ordering was studied and it was shown that its thermal conductivity in the through-film direction would be improved by a factor 20 compared to amorphous carbon films.[14] The downside of NCG is its electrical conductivity, which makes it unsuitable for the use directly on top of the heating elements which are typically transistors and require an insulative passivating layer. This is precisely where *voBN* becomes of interest as it can fill the gap that NCG cannot. The previous chapter reported a significant improvement in through film Thermal Conductivity (TC) of *voBN* compared to its amorphous counterpart, however no study of its in-plane TC was performed.[15]

5.1.2 Work performed

We show here that *voBN* is indeed a material with anisotropic TC by experimentally characterizing its TC in both directions. In addition, Molecular Dynamics simulations were run to identify the reason of this anisotropy. Both experimental and simulated results show a through film TC an order or magnitude higher than the in-plane TC. Finally, using those thermal results, some COMSOL Multiphysics was used to run some simulations on the thermal behavior of a hot spot array and illustrates how the thermal anisotropy of *voBN* allows an increase in device density by up to 300% when compared to SiO_2.

5.2 Experimental setup

5.2.1 Sample preparation

The *voBN* samples used in this study were all prepared using the method described in the previous chapter, based on the reactive sputtering of an LaB_6 target in nitrogen in HiPIMS mode. The vacuum chamber was pumped down to 10^{-6} mbars and the partial pressure during growth was maintained at 2.5×10^{-3} mbars. In the same fashion as in the previous chapter, the films were grown with pulses 25 µs long and 30 A of peak current at a 4 KHz repetition rate. The discharge voltage was 700 V with a average current of 500 mA, yielding an average power of 350 W and a peak power density of over 100 $W.cm^{-2}$. FTIR and cross section HRTEM was used to characterize the film microstructure and confirm the presence of h-BN basal planes with vertical alignment.

5.2.2 Thermal characterization

To measure the thermal conductivity for both in-plane and through plane (referred later as K_x and K_y), the 3ω method was used.[16-18] Using the same method, the thermal boundary resistance was R_{BN-Si} also computed. The principle of the 3ω method is to use a thin metallic wire micro-fabricated on the surface of the thin film that requires thermal measurement to play the role of both the thermometer and the heater. An AC current with pulsation ω is injected into the wire and the signal measured in output from the wire is the third harmonic voltage at 3ω to compute its temperature variation. By sweeping the pulsation ω through a wide range of frequencies, an experimental curve representing the temperature oscillations depending on the pulsation is obtained and a two-dimensional model of the heat conduction in the thin film layer and substrate can be used to infer K_x , K_y and R_{BN-Si} .[17, 19, 20] For the actual measurements, three Au/Cr metal wires of thicknesses 200/5 nm were deposited onto a 300 nm thick *voBN* thin film on Si substrate via electron beam evaporator. Each was 1 mm long with various widths: 4, 10 and 40 µm. Both 40 and 4 µm wires were used to get the through plane and in-plane TC while the 10 µm one was to confirm the accuracy and robustness of the heat conduction model used. All measurements were made in vacuum and each wire was connected to a chip carrier via gold wire bonding.

5.2.3 Molecular Dynamics (MD) simulation

The principle for the MD simulations was to start with simple elements and put them together at the end to get the final result. As *voBN* is made of h-BN nanocrystals oriented in the same direction, with amorphous BN in between, the MD simulations focused on computing both h-BN and a-BN TCs separately to finally use a series model to compute the final TC when both are mixed together. To achieve that, the simulation was achieved in three separate steps: generation of amorphous BN via MD simulation, *voBN* TC computation and *voBN*-Si thermal boundary conductance computation.

5.2.3.1 Amorphous BN generation through MD

Manually entering the parameters for creating amorphous materials in MD simulations is not possible and requires alternative solutions to get amorphous materials. Here, the BN is “amorphitized” by melting and quenching a cubic BN crystal. The method used was based on the fairly standard liquid-quench method,[21, 22] using the Large-scale Atomic/Molecular Massively Parallel Simulator (LAMMPS) code combined with the Tersoff potential.[23, 24] Using a periodic boundary condition in all directions, the temperature in the crystal vicinity is increased with increments of 1000 K from 0 K up to 5000 K (NVT setup – constant number of atoms, volume and temperature). For each increment, the temperature is raising at 100 K/ps, with a 20 ps wait time in between two steps to allow the temperature to equalize in the whole crystal structure. Once the whole system has stabilized at 5000 K, it is then cooled down to 300 K at a rate of 1000 K/ps. Once at 300 K, the system is changed from NVT to NPT (constant number of atoms, pressure and temperature) and the simulation is run for another 50 ps to allow some time for the obtained amorphous BN to relax fully. In order to verify the successful conversion from crystalline to amorphous BN, the Radial Distribution Function (RDF) was used to compare both atomic structures before and after the liquid-quench process. The RDF displays the probability density for the presence of an atom with regards to its distance from an origin point. For instance, a crystalline structure will display a RDF with a cyclical sharp peak response due to the well ordered structure that will display high probability of an atom being at multiples of the structure's bond length. The RDF is shown in Figure 5.1 below and shows the difference between both h-BN and a-BN. Hexagonal BN (inset b) displays high intensity and sharp peaks while in comparison, amorphous BN (inset a) produces lower intensity and fewer peaks, with a tail-like distribution across the whole range of radii due to the disorder and lack of crystalline structure within the BN structure. A similar transition between graphite and amorphous carbon has previously been studied by Li et al. where the RDF would show less peaks, with lower sharpness, after amorphitization of carbon.[25] Overall, this data is in good agreement with McCulloch et al. who reported a RDF for amorphous BN made of a fairly sharp peak at 1.5 Å, followed by another peak at 2.6 Å and finally a weak response at 3.8 Å.[26] In contrast, the h-BN response displays an additional peak at 3 Å, with all the peaks having higher intensity and being sharper, with a zero RDF response in between each peak, showing the complete absence of atoms at those distances. This type of RDF response is typical of a highly ordered atomic structure. Additionally, the RDF for a-BN shows a flat region between the second and third peaks which has been shown by McKenzie et al. to be characteristic of amorphous materials.[27]

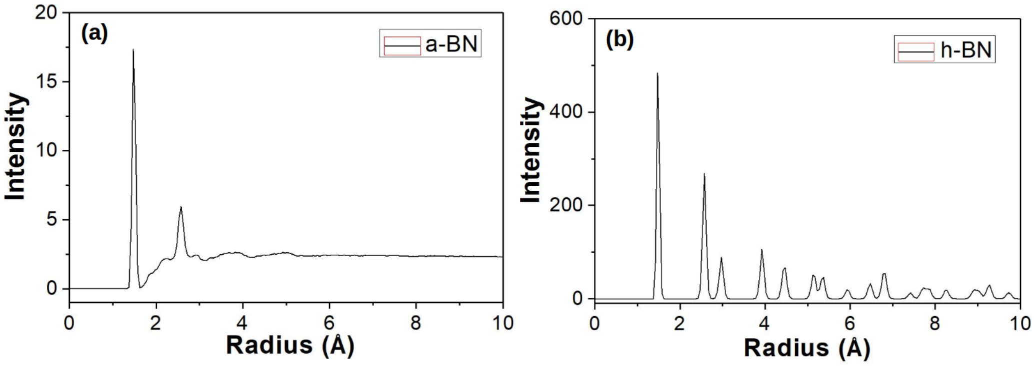

Figure 5.1 - Comparison of the RDF between amorphous BN (a) and hexagonal BN (b).

5.2.3.2 TC computation for voBN

Once a-BN was generated, the TCs for both hexagonal and amorphous phases were first computed. In the case of h-BN, the TC had to be computed in the plane direction as well as in the intra-plane direction, as shown in Figure 5.2. For h-BN the bond length used is 1.45 Å, and the distance between two h-BN sheets is 3.35 Å. For the computation, the simulation cell size was set as a cube of size 50 Å in order to have a crystal size of 5 nm.

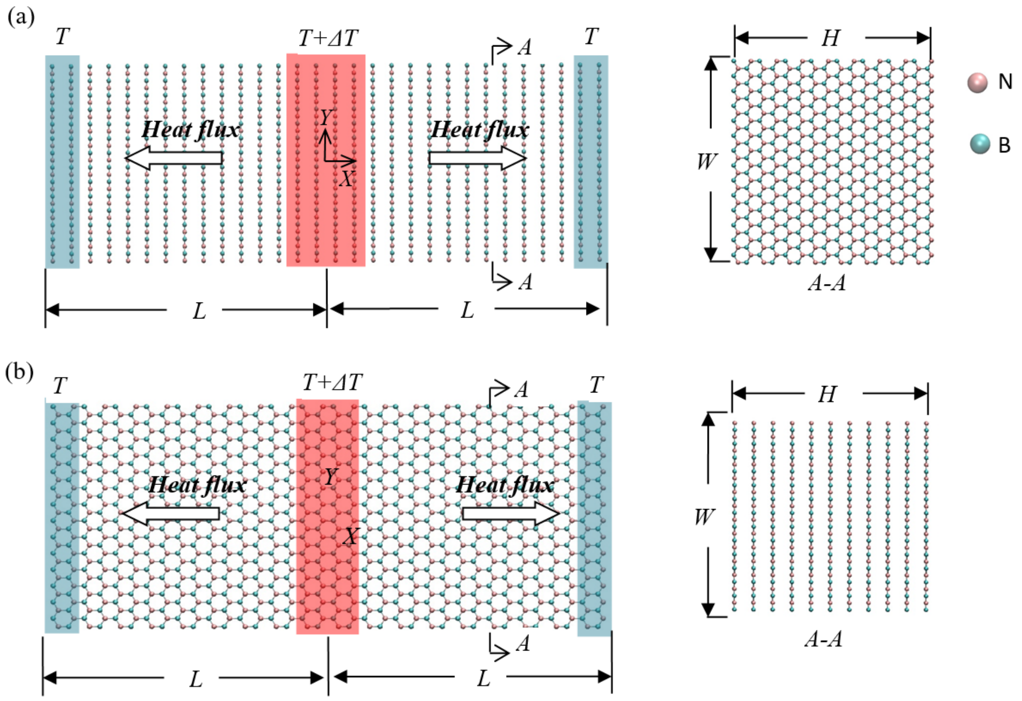

Figure 5.2 - Schematics of the simulation models for the thermal conductivity along (a) the inter-plane and (b) the intra-plane directions of the crystalline h-BN phase. The simulation model for the thermal conductivity of the amorphous BN is similar to that for the crystalline h-BN layers and thus is not shown here. The region highlighted with red in the middle is set as the heat source region and held at the temperature at T+ΔT, and the regions highlighted with blue at the two ends are set as heat sinks and held at a lower temperature of T.[28]

In their thermal conductivity MD simulation of h-BN nanocrystals, Lindsay and Broido successfully used a combination of Tersoff and Lennard-Jones potentials for the in-plane and inter-plane interactions respectively to obtain accurate thermal conductivity values.[29] A similar approach was used here to model the h-BN crystals required to compute the thermal conductivity of *voBN*. Free boundary conditions are applied to the y and z directions while a periodic boundary condition is applied in the x direction. For the covalent bonding between B and N atoms in the hexagonal planar structure, the interaction is described by the Tersoff potential.[30, 31] The weak Van der Waals forces for the inter planar bonding as well as the bonding between the atoms from the hexagonal and amorphous BN are described by the Lennard-Jones (LJ) potential. The Universal Force Field (UFF)[32] provides the LJ parameters for the N-N and B-B bondings while the parameters for the B-N pair are given by the Lorentz-Berthelot mixing rules. The Fourier's law of thermal conduction, given by $J = -\lambda \nabla T$ where

J is the heat flux, ∇T is the gradient of temperature in the direction of the heat flux and λ is the thermal conductivity, is applied to compute the TC by running a reverse non-equilibrium MD simulation. The simulation starts first with relaxation of the NPT system for 20 ps using steps of Δt of 0.1 fs, followed by another 20 ps with the system changed to NVT to ensure it has reached an equilibrium state. From then on, the system is changed to a constant volume and energy (NVE) mode as the energy needs to be conserved. In order to create a temperature gradient in the x direction, the atoms in the red region of length 2δ as shown in Figure 5.2 are set to $T+\Delta T=400$ K and are coupled with a Nosé-Hoover thermostat to maintain the Δt constant. On the other end of the system, the atoms in the blue zone of length δ as shown in Figure 5.2 are kept at a temperature of $T=300$ K and are used as heat sinks by coupling them with a Nosé-Hoover thermostat each. In Figure 5.2a, the distance δ is set to 6.7 Å as it is the length of two h-BN planes. In a similar fashion, δ is set to 4.35 Å in Figure 5.2b as this is the distance to encompass a whole BN hexagon. After setting up those initial conditions, the simulation is run for 100 ps so that the system has enough time to reach a steady-state and the gradient ∇T has stabilized along the x direction. Once ∇T is constant, the simulation is executed for another 50 ps in order to measure the time-averaged gradient profile as well as the heat flux. The heat flux (or energy change rate) is computed by recording the accumulative energy changes over time at both the heat sinks and heat source. The gradient profiles for both configurations (Figure 5.2a and b) are computed by calculating the temperature of each h-BN plane for the Figure 5.2a case, or dividing the system in small slices of length equal to a zigzag chain, i.e. 2.175 Å. The temperature is deducted from the average kinetic energy contained in each slice. Finally, using Fourier's law, the TC can be found as shown in the results section.

5.2.3.3 Thermal boundary conductance computation for the amorphous-crystalline interface

For a system that has an interface between two different phases, a sudden temperature drop can be ΔT_{drop} observed when there is a temperature gradient imposed by a heat flux J . From that heat drop, the thermal boundary conductance G , or Kapitza conductance, is derived by $G = J / \Delta T_{drop}$. The simulation used to compute G is shown in Figure 5.3. The system is the same size as the one shown in Figure 5.2 and the blue (heat sink of temperature T) and red zones (heat source of temperature ΔT) have a distance δ which is the same as Figure 5.2a and b (6.7 Å and 4.35 Å), respectively to Figure 5.3a and b. The simulation process is the same as in the previous section.

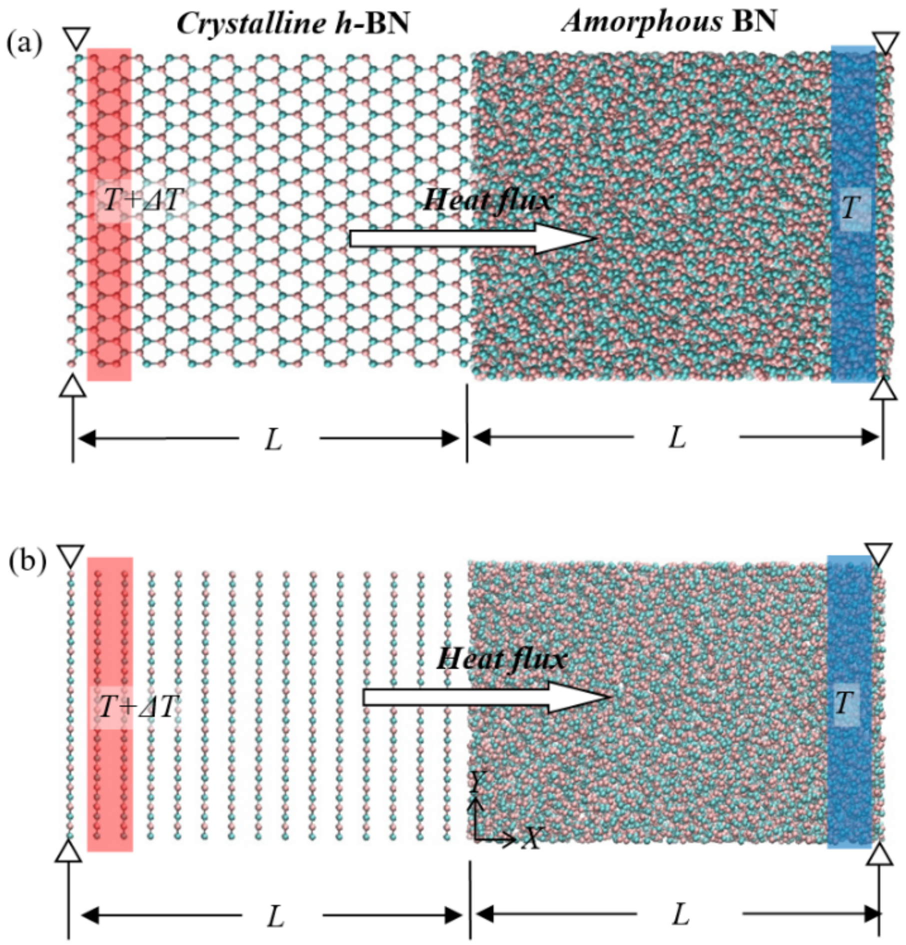

Figure 5.3 - Schematics of the simulation models for the calculation of the thermal conductance of the interface between the crystalline h-BN layers and amorphous BN with (a) intra-plane covalent bonding and (b) inter-plane non-covalent bonding. The region highlighted with red at the left end is set as the heat source region and held at the temperature of $T+\Delta T$. And the region highlighted with blue at the right end is set as the heat sink and held at a lower temperature T . Atoms in thin slabs with a width of ~2 Å near the heat source and sink are fixed as rigid.[28]

5.2.4 COMSOL Multiphysics simulation

5.2.4.1 Simulation model assumptions

As for all simulations, the model needs to be bounded and defined with limit conditions in order to have the computation converging towards a stable solution.

- The first assumption is that the simulations are run with materials of 100 µm in thickness. This is to facilitate the impact of anisotropic TC and be able to “visually” see it. However, a thinner layer would behave the same as the physics underlying the simulation model would remain the same, whichever geometry is used.

- As seen in actual devices such as microprocessors, the number of heating devices (or transistors) is so huge that the simulation can consider their amount to be infinity. As such, the simulation can be considered to be made of many transistors encased in a "unit cell" as seen in Figure 5.4. Each unit cell is set with a length of 100 µm and as they are all identical, there won't be any heat gradient between cells, meaning a single cell can be considered as an adiabatic system, with only the top part of the cube is set to 20 degC to allow the heat to escape from the top (as per an actual electronic device).
- Only the stationary solutions are studied here and no transient simulation are performed.

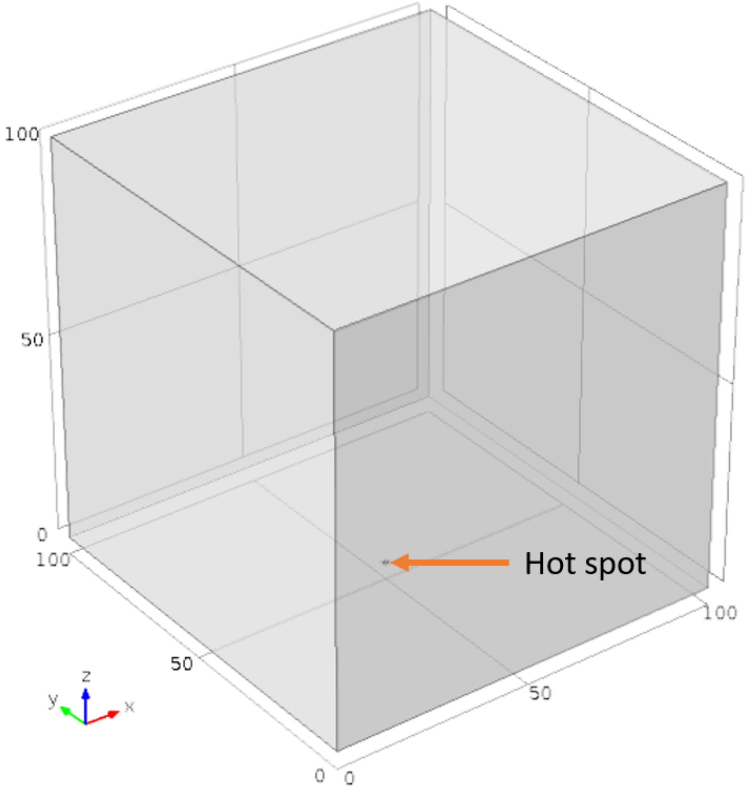

Figure 5.4 - Unit cell where thermal crosstalk will be simulated.[28]

5.2.4.2 Set of equations used in the model

The Heat Transfer Module in COMSOL comes with a standard set of equations:

- Heat transfer within solids (Fourier's Law): $\nabla T + \nabla \vec{q} = Q$ with $\vec{q} = -k \nabla T$. Q is the heat source or sink (depending on its sign) and $\vec{q}$ is the vector heat flux.
- As the system is defined as adiabatic on the bottom and sides of the cube, those surfaces would contain the following condition: $-\vec{n}.\vec{q} = 0$ to ensure no heat can escape.
- The face on top of the cube is set to $T = 20$ degC as it will act as heat sink in the simulation.
- At the center of the cube's bottom face, a 1 µm by 1 µm hot spot is defined. The heat it inputs in the system is set to 0.1 mW, and is evenly generated through the hot spot surface: $-\vec{n}.\vec{q} = Q_{hotspot}$ where $Q_{hotspot}$ is set to 10^8 W.m^{-2}, which is 0.1 mW per µm^2. A square surface instead of a point is used to simulate the hot spot as a point without surface will create a singularity at the point, where 0.1 mW would be generated from an infinitesimal surface point, inducing temperatures reaching $+\infty$.

5.2.4.3 Design of the mesh

Meshing a simulation is a critical part of the process and a wrong or not properly designed mesh could affect the simulation results and their precision. Indeed, in areas were metrics are varying widely over a small distance, the mesh has to be sufficiently small to properly and accurately model their behavior. Figure 5.5a displays an example of bad mesh design, and how the results look like in comparison to Figure 5.5b where a proper meshing was applied. The difference in meshing is shown in Figure 5.5c and d where the number of mesh elements for the 1 µm by 1 µm hot spot is changed from two (insufficient meshing) to over twenty (proper meshing). Figure 5.5d also show how the meshing is more detailed in the surrounding areas of the hot spot, to allow greater flexibility where larger temperature gradients are expected. In addition, the mesh generated for the simulation was made of tetrahedral elements, with a 1.4 µm minimum size and 10 µm maximum size, except for the hot spot region where the mesh was refined to a minimum element size of 0.02 µm and a maximum of 2 µm. Using a small mesh was attempted but the results would not improve further and the computing time would grow exponentially, indicating the chosen mesh was the optimal one.

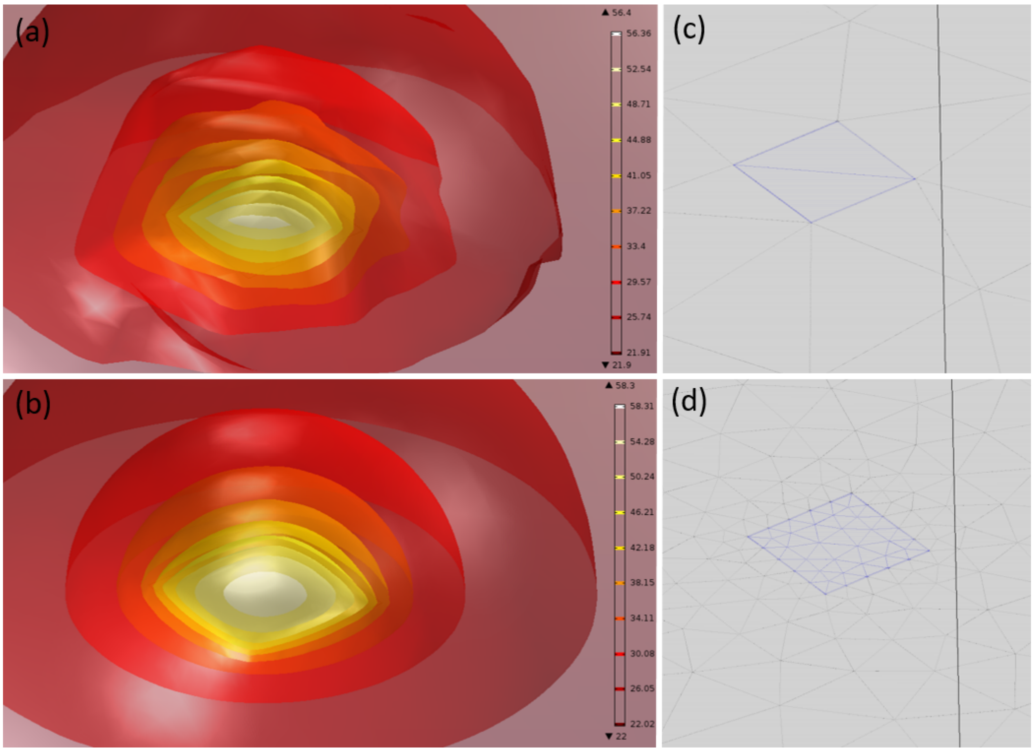

Figure 5.5 - Comparison of isothermal contours simulations with SiO_2 around the hot spot with a bad mesh (a) and a good mesh (b). It can also be observed that the computed temperatures between both simulations are not the same. Inset (c) and (d) show the difference in meshing quality for both simulations.[28]

5.3 Results and discussion

5.3.1 *voBN* microstructure verification

Figure 5.6a shows the HRTEM image of the *voBN* thin film used for the thermal characterization in this work. The film thickness was 1134 nm according to the cross section TEM and the vertical alignment of the h-BN nanocrystals can be clearly seen in the image. The vertical ordering is further evidenced through the FFT computation of the image itself, showing two partial rings for the (0002) h-BN plane with an average spacing between planes of 0.35 nm, which is comparable to bulk h-BN (0.33 nm). FTIR was also used to assess the amount of ordering and whether it was h-BN as shown in Figure 5.6b. The ratio between the peak located at 1380 cm^{-1} (for the in-plane B-N stretching vibration mode) and 780 cm^{-1} (for the B-N-B out-of-plane bending vibration mode) in order to assess the amount of ordering in the vertical direction. The method for the peak measurement and how to get the ratio is explained in Chapter 4 and a ratio above 0.5 indicates a good vertical ordering of the h-BN basal planes, while anything below 0.2 would indicate the presence of in-plane h-BN only.[15, 33-35] In Figure 5.6b, the ratio between the two peaks is 0.613, which confirms the HRTEM results. In addition, the absence of c-BN in the film is also confirmed as there is no peak at all located at 1050 cm^{-1}, indicating the film is made of 100% of sp^2 h-BN clusters.

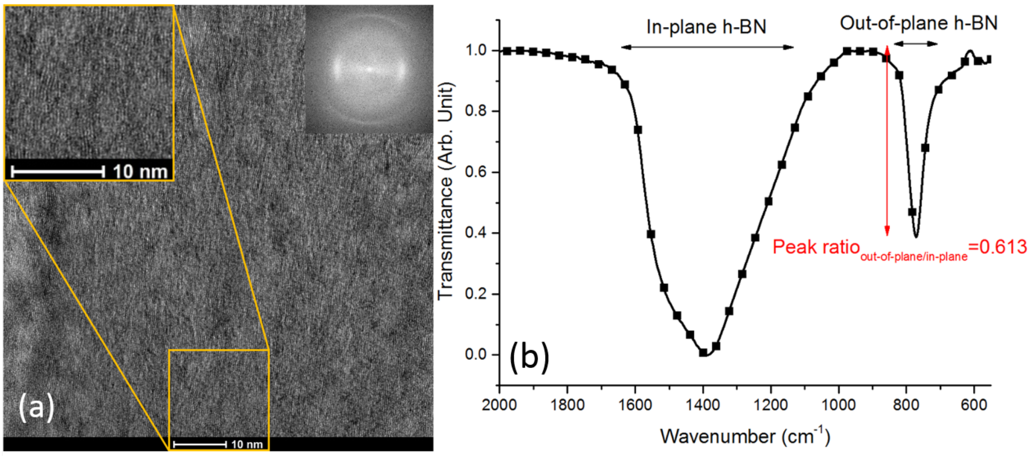

Figure 5.6 - (a) High resolution cross section TEM image of a vertically ordered BN thin film. The top left image is a zoom-in showing in more detail the BN crystal lattice with vertical alignment. The vertical alignment is further confirmed by the computed FFT which displays the typical partial rings for the (0002) h-BN planes with alignment perpendicular to the substrate plane. The outer ring corresponds to the (-2110) h-BN plane. (b) FTIR response for a typical BN film with h-BN planes vertically ordered with respect to the silicon substrate. The determining criteria is a value above 0.5 when computing the normalized ratio between the in-plane and out-of-plane IR active modes.[28]

5.3.2 Dielectric constant computation

VoBN can only be useful as a thermal extractor if it is a dielectric material. BN is indeed one, meaning that *voBN* should naturally be one. However, when growing *voBN* with HiPIMS, a non-negligible concentration of La can be found in the film, which could affect the electrical properties of the film. In order to confirm the dielectric property of *voBN*, its dielectric constant is calculated here by sandwiching it between two copper electrodes and computing the complex impedance of the whole device. The principle of this technique is to measure the capacitance C in order to retrieve the *voBN* dielectric constant ε_r by using the parallel plate capacitor formula:

$$C = \varepsilon_r \varepsilon_0 \frac{A}{t} \quad (5.1)$$

A is the capacitor plate area, t is the distance between the two plates, which is here the *voBN* thin film thickness and ε_0 is the permittivity of free space which is 8.854×10^{-12} F.m^{-1}. The formula above works in the particular case where the capacitor plate's smallest cord is much bigger than the film thickness. With a capacitor plate in the cm range and a film thickness in the hundreds of nm range, this assumption is valid. Figure 5.7 below shows a picture and design of the capacitor used to compute the dielectric constant.

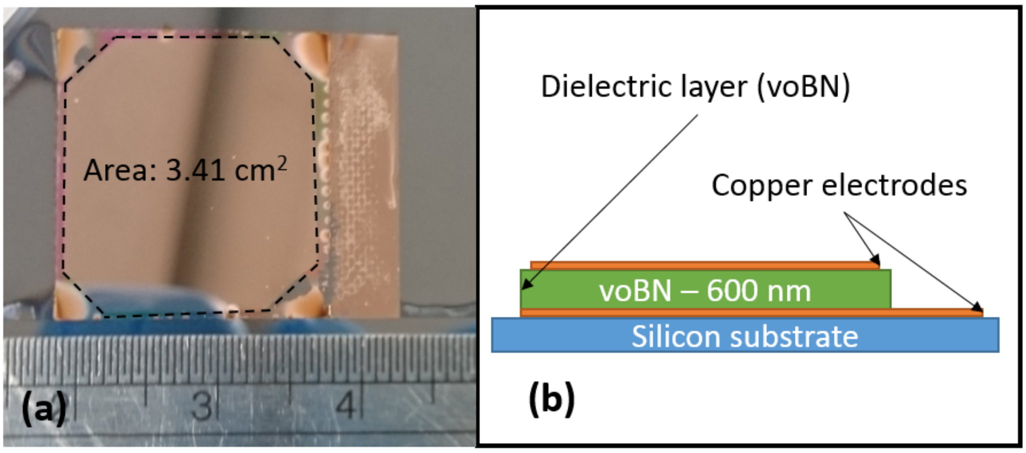

Figure 5.7 - Inset (a) is a photo of the device, with the area of the top copper electrode computed to be 3.41 cm^2. Inset (b) is a schematic of the design in cut view. The *voBN* film thickness was computed to be 600 nm via surface profiling.[28]

With the help of a probe station and with the assumption that the device was behaving like a RC series circuit, the complex impedance of the capacitor device was measured across frequencies ranging from 1 KHz to 1 MHz. Using the definition of the Cartesian form of the complex impedance and its derivation for series RC circuits, we get the following two equations:

$$\begin{cases} Z = R + jX \\ Z = R + \dfrac{1}{j\omega C} \end{cases} \leftrightarrow X = \frac{-1}{\omega C} \leftrightarrow Cf = \frac{-1}{2\pi X} \qquad (5.2)$$

Z is the complex impedance, with R being the real part of it (resistance) and X is the imaginary part (reactance). The pulsation ω can be written using the frequency f via the equality $\omega = 2\pi f$. When sweeping f from 1 KHz to 1 MHz, the plot shown in Figure 5.8a is obtained.

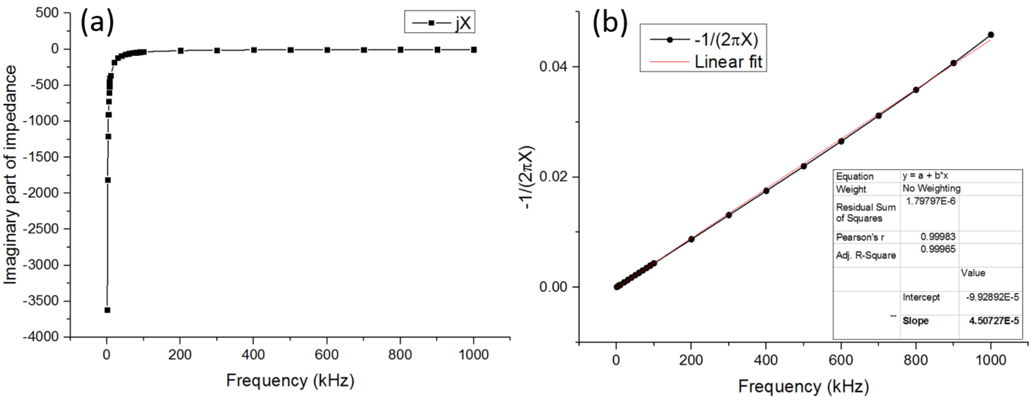

Figure 5.8 - (a) is a plot of the imaginary part of the complex impedance. (b) is a plot of $\frac{-1}{2\pi X}$ and is linearly fitted in order to extract the capacitance. The computed slope is 45×10^{-6} , which gives a capacitance of 45 nF (there is a factor 1000 due to the plot axis being in kHz instead of Hz).[28]

Figure 5.8a is a plot of the reactance depending on the frequency of charge/discharge in the capacitor. From the equation above, the inverse reactance is a linear fit of the capacitance with regards to the frequency and a slope of 45×10^{-6} is obtained, which is equivalent to 45 nF. This leads to *voBN* having a dielectric constant of around 8.9, which is more than what the literature reports.[34] However, the accuracy of this value is small, due to the number of measurements involved, from the film thickness to the capacitor plate area, as well as the frequency sweep of the reactance. In the end, the main objective here was to prove *voBN* (containing La) was still as dielectric that can be used to passivate and cool down active electronic devices.

5.3.3 3ω thermal characterization

3ω was used to measure the thermal properties of the BN thin film as it is able to measure the thermal conductivity in both the in-plane and through-plane directions.[36, 37] The slope method was used to compute the through-plane thermal conductivity, based on the temperature oscillation ΔT_{s+f} of the 40 µm wire as shown in equation 5.3:[17]

$$\Delta T_{s+f} = \Delta T_s + \frac{p d_f}{2 b l k_f} \quad (5.3)$$

Here, p is the input power, l and b are the heater length and half width, k_f and d_f are the thin film through plane TC and thickness. The temperature oscillation of the bare substrate is ΔT_s and is obtained via the equation 5.4 below:[17]

$$\Delta T_s = \frac{p}{\pi l k_s} f_l(\ln \omega) \qquad (5.4)$$

In equation 5.4, p and l are the same as for equation 5.3. k_s is the TC of the bare silicon substrate and f_l is a linear function with regards to $ln\omega$. In Figure 5.9a, the temperature oscillation for the 40 µm wire is plotted in function of the frequency, for both the BN thin film on Si substrate as well as the reference bare Si substrate. Using equations 5.3 and 5.4, the through plane thermal conductivity for *voBN* was found to be 4.26±0.4 $W.m^{-1}.K^{-1}$. In order to compute the in-plane TC as well as R_{BN-Si} , the use of the 4 µm is necessary. In addition, the use of more complex equations for the temperature oscillation is necessary, and equations 5.5 to 5.7 can accurately describe the thermal oscillation ΔT for a heater on top of a thin layer that has an anisotropic TC. As such, ΔT , while taking into account the contribution of R_{BN-Si} can be expressed as:[17, 19]

$$\Delta T = \frac{-p}{\pi l k_{y1}} \int_0^\infty \frac{1}{A_1 B_1} \frac{\sin^2(bx)}{(bx)^2} dx \qquad (5.5)$$

In equation 5.5, p and l are the same as for equation 5.3 and k_{y1} is the through plane thermal conductivity of the BN thin film. In addition, A_1 and B_1 are described as follows:

$$A_1 = \frac{\left(A_2 + \kappa_{y2} B_2 R_{th}\right) \dfrac{\kappa_{y2} B_2}{\kappa_{y1} B_1} - \tanh\left(\varphi_1\right)}{\left(1 - \left(A_2 + \kappa_{y2} B_2 R_{th}\right) \dfrac{\kappa_{y2} B_2}{\kappa_{y1} B_1} \tanh \varphi_1\right)} \quad (5.6)$$

$$B_i = \left(k_{xi}/k_{yi} x^2 + \frac{2 i\omega}{\alpha_{yi}}\right)^{1/2}, \varphi_i = B_i d_i, i = 1{,}2, A_2 = -\tanh^{-1}\left(B_2 d_2\right) \quad (5.7)$$

k and α are the TC and thermal diffusivity respectively. The subscripts in both of them refer to the in plane direction for x and through plane for y, while 1 refers to the BN thin film while 2 is for the substrate. Using equation 5.5 and the previously computed through plane TC, the experimental temperature oscillation ΔT was fitted, with the best fit providing the in-plane TC as well as R_{BN-Si}. In the end k_{y1},was computed to be 0.26±0.05 $W.m^{-1}.K^{-1}$ and R_{BN-Si} was (5.9±1.2)x10^{-8} $m^2.K.W^{-1}$. The fitting and experimental data for the 4 µm wire is shown in Figure 5.9b, as well as the experimental data and theoretically computed curve for the 10 µm wire. The data for the 10 µm was used to confirm the fittings from the 2 other wires, and make sure of the accuracy of the results by making sure there is a good agreement between the computed data and the experimental one. In the end, the TC in both directions could be computed and it was found that the through plane TC was 16 times greater than the in plane TC, confirming that *voBN* has an anisotropic TC. This anisotropy could be explained by the vertically ordered h-BN basal planes, which are facilitating the phonon transport in the through plane direction.

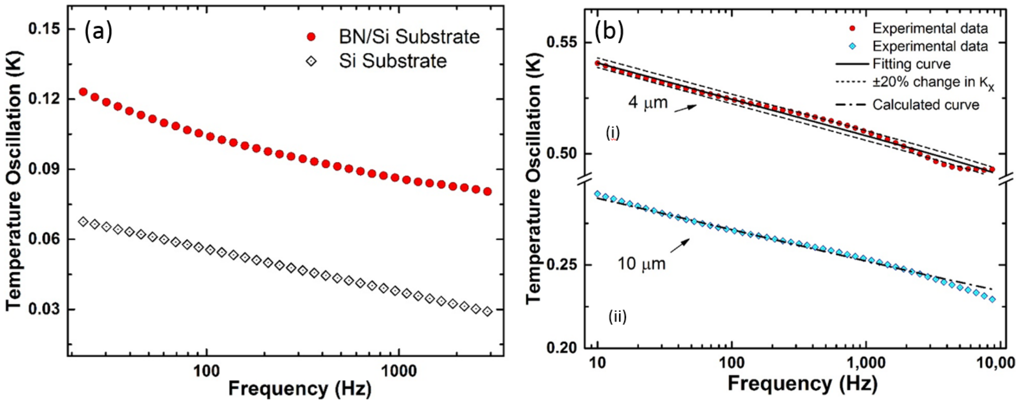

Figure 5.9 - (a) The experimental and the calculated temperature oscillation for the 40 µm wide wire deposited on BN/Si and reference (bare Si), respectively. The temperature difference between the Si substrate and the BN/Si is used to calculate the cross-plane thermal conductivity of BN film on Si substrate. (b) (i) The experimental temperature oscillation for the 4 µm wide deposited wire on BN/Si and corresponding fitting curve from the two-dimensional heat conduction model and calculated curve for ±20% change in the best fitted value for K_x. (ii) The experimental temperature oscillation for 10 µm wide deposited wire on BN/Si and corresponding calculated curve from the two-dimensional heat conduction model based on the K_y, and the fitted K_x and R_{BN-Si} values determined by fitting the 4 µm wide heater.[28]

5.3.4 Molecular Dynamics results

In order to study the impact of the peculiar microstructure of *voBN* on the thermal anisotropy, Molecular Dynamics simulations were performed. Figure 5.10a shows the temperature distribution between two basal planes in the through plane direction, while Figure 5.10c shows the same distribution in the planar direction.

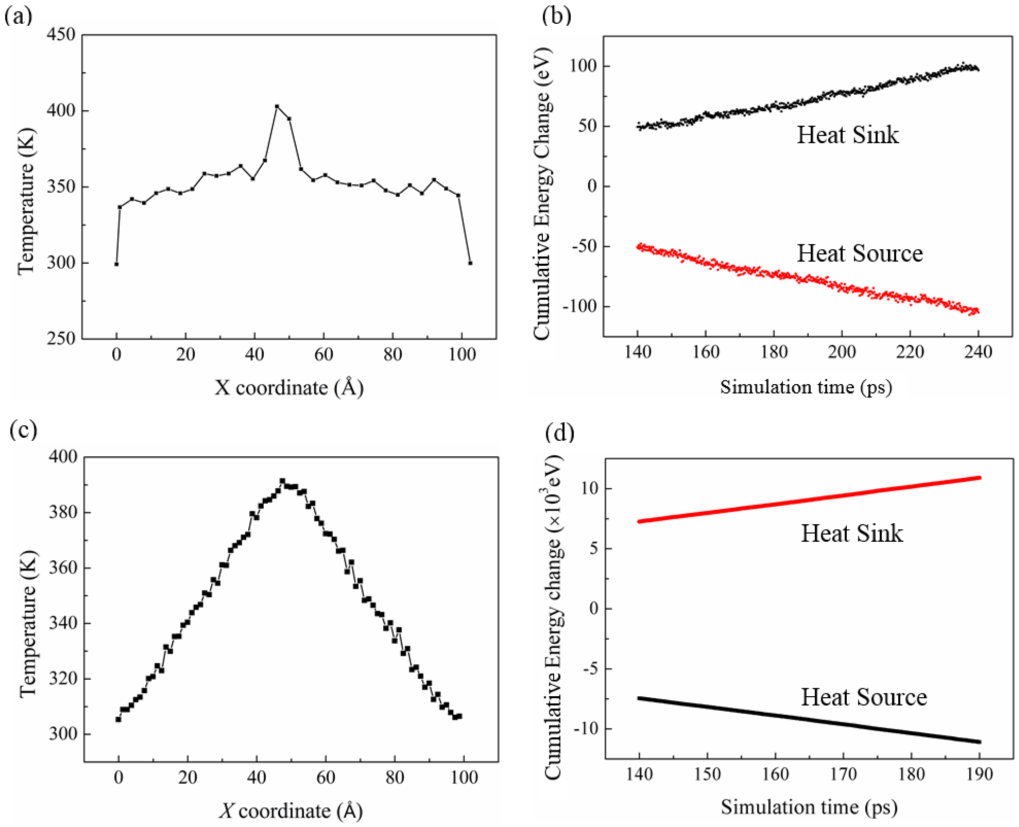

Figure 5.10 - Temperature distribution and the accumulative energy changes with the simulation time between 2 planes (a, b) and within the same plane (c, d) directions for the crystalline h-BN.[28]

In both directions, the temperature decreases from the heat source to the heat sink in a linear fashion, with the exception of the heat source and sinks vicinities in the through plane direction where a sharp drop in temperature can be observed and is caused by the weak non-covalent bonds between the different h-BN planes. Insets b and d in Figure 5.10 are displaying the cumulative energy change in both heat source and sinks for the through plane and in plane directions respectively. In both cases, the energy changes linearly with time. Similar results have been computed for amorphous BN as they will be required later on, and they are not shown here. Applying a linear fitting on those results provides the temperature gradient as well as the heat flux, and using Fourier's law of heat conduction $J=-\lambda\nabla T$, the thermal conductivity λ was computed. The TC for amorphous BN was computed to be 6.61 W.m^{-1}.K^{-1} while for h-BN, the values obtained changed depending on the direction, with a value of 26.97 W.m^{-1}.K^{-1} in the planar direction, and 1.39 W.m^{-1}.K^{-1} in the through plane direction.

Now that the TC for pure amorphous and pure hexagonal BN has been computed, both are bonded together to study the interface (see section 2.3.3 for more details). Figure 5.11 is a plot of the temperature distribution in the heat flux direction between a crystalline h-BN zone and its amorphous counterpart. The figure shows a sharp temperature drop at the interface, with $\Delta T_{\ln}=17\,K$ and the heat flux is 8.245 eV/ps. Using the relation $G=J/\Delta T_{\ln}$, the thermal conductance for the covalently bonded interface is computed to be 4.08x10^{9} W.m^{-2}.K^{-1}. In a similar fashion, the same process was applied to a system where the interface was non-covalently bonded to obtain a thermal boundary conductance of 0.514x10^{9} W.m^{-2}.K^{-1}.

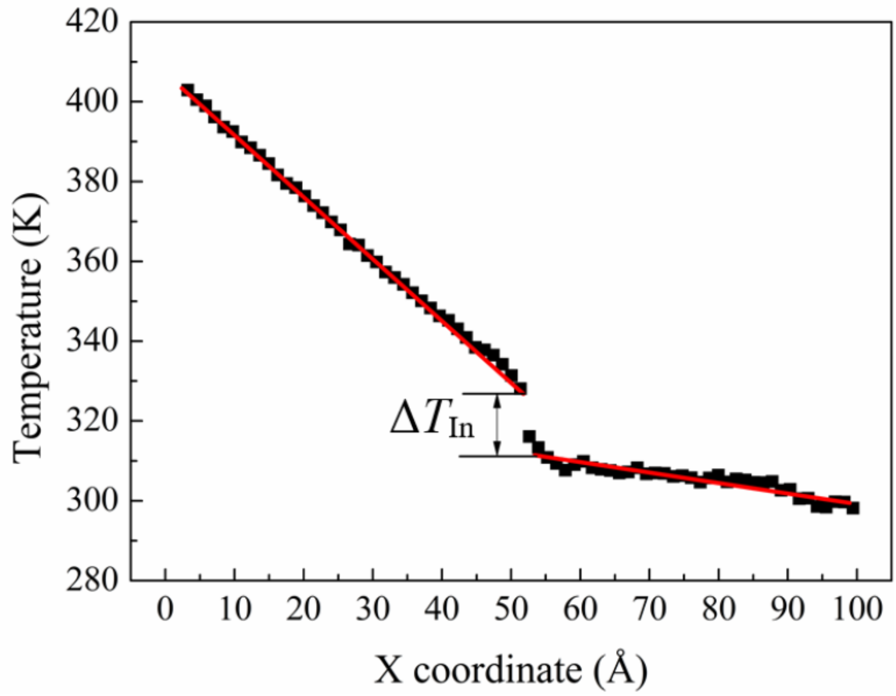

Figure 5.11 - Temperature distribution along the heat flux direction for the hybrid system of the crystalline h-BN and amorphous BN with covalent-bonded interface shown in Figure 5.1a. The red lines are drawn to guide the eye.[28]

The model in figure 5.12 is used to predict the thermal conductivity of *voBN* in both the in plane and through plane directions. The model consists of a series chain where some h-BN crystals of cubic shape are aligned in series and are surrounded by amorphous BN, which plays the role of the boundary layer between two h-BN nanocrystals. Based on the rule of mixtures, equation 5.8 is used to compute the thermal conductivity κ of the whole chain system:[38, 39]

$$k^{-1} = \sum_i f_i k_i + nG^{-1} \qquad (5.8)$$

In the equation above, k_i and f_i are the TC and length fraction of the component i and G is the thermal boundary conductance added n times for the number of interfaces per unit length.

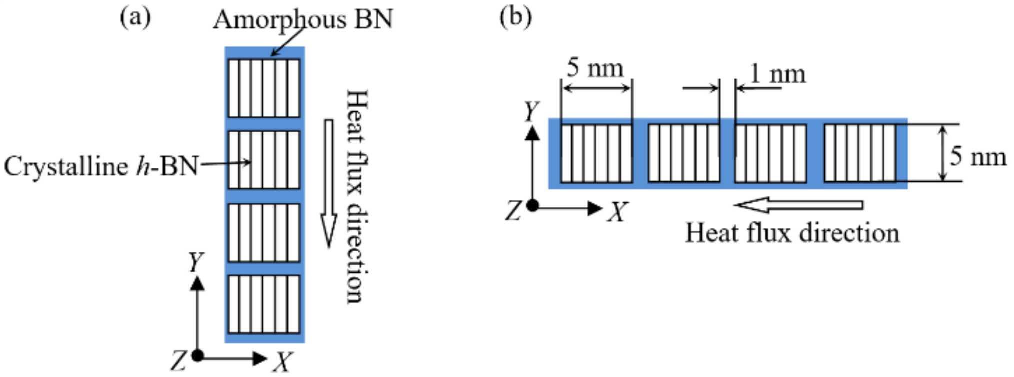

Figure 5.12 - Series chain model for the calculation of thermal conductivity along the (a) through plane and (b) in plane directions.[28]

As observed from the TEM images, a length of 5 nm was used for the ridge of the cube shaped h-BN crystal, with a boundary of 1 nm or amorphous BN between two cubist crystals. Such dimensions give length fractions of 0.833 and 0.167 for h-BN and a-BN respectively, while the number of interfaces per unit length is calculated to 0.33 nm^{-1}. By using the in plane TC of h-BN in equation 5.6, the *voBN* TC in the through plane direction is computed to be 7.30 W.m^{-1}.K^{-1}. Conversely, the in plane TC of *voBN* is found to be 0.79 W.m^{-1}.K^{-1} when using the through plane TC of h-BN with equation 5.6. The computed TC for *voBN* in both directions is slightly higher than the experimental one, and could be due to the chain series model as this model represent the perfect case of h-BN crystals aligned in the exact same direction. In the actual *voBN* thin film, the crystals are never fully aligned and thus the TC reading is actually lower. In addition, the MD simulations used defect-free h-BN nanocrystals which contributes to giving a higher TC value as the phonons tend to scatter less. In the end, both simulation and experiment agree to the same extent on the high anisotropy of *voBN*, with a through plane TC around an order of magnitude higher than the in plane direction. This anisotropy is believed to come from the anisotropic TC of h-BN, coupled with the thermal boundary resistance at the interfaces between h-BN and amorphous BN. The ratio $R=nG^{-1}/\kappa^{-1}$ is used to assess the impact of the interfaces on the overall TC, and R shows to which extent the interfaces contribute to the TC. The obtained R is 51% and 59% for the TC in the in plane and through plane directions respectively, suggesting the crystalline/amorphous interfaces in the material play a major role in preventing the phonons to propagate. Such outcome is in agreement with other studies focusing on the interfacing of hybrid systems.[40, 41] As such, a way to increase the thermal conductivity for *voBN*, based on equation 5.8, would be to lower the interface density which means to increase the crystal size in the material. Figure 5.13a and b provides a plot of the TC in function of the h-BN grain size in the *voBN* thin film (assuming the grain boundary interfaces do not change in thickness), and it can be seen that an increase of the size would induce and increase of TC in both planar and through plane directions. Figure 5.13c is the computation of the anisotropic ratio between the through plane and in plane TCs and it can be observed that an increase of crystal size in the thin film induces an increase in anisotropy, in favour of the through plane direction. It has to be highlighted that for the values computed in Figure 5.13, the TC in both directions was computed using equation 5.8, based on the TC values for a 5 nm grain of h-BN, and only the length fractions were changed. In general, the TC in both directions is expected to increase with an increase in size, especially for the planar direction of h-BN which contributes to the though plane TC of *voBN*. Therefore the values presented in Figure 5.13a are expected to be higher, meaning that in practice, the ratio plotted in inset (c) should be greater than computed.

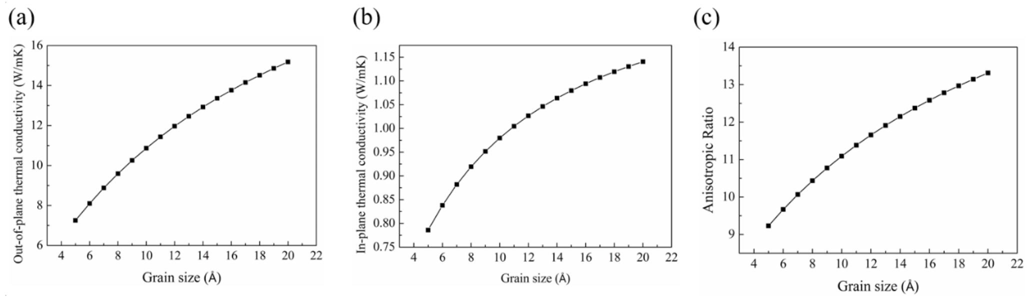

Figure 5.13 - The dependences of (a) the out-of-plane, (b) the in-plane thermal conductivities and (c) the anisotropic ratio between them on the grain size of the crystalline h-BN.[28]

Finally, the thermal boundary conductance at the interface between amorphous and crystalline h-BN is directly linked to the phonon spectra in both materials. Indeed, a good matching between both spectra will induce a good thermal interface conductance.[42, 43] Figure 5.14 shows a plot of both spectra with a weak correlation between the two, especially in the 0-10 THz and 45-55 THz ranges, inducing a lot of phonon scattering at the interface between both materials. This big mismatch will result in an increase in thermal boundary resistance which in turns contributes to lowering the overall thermal conductivity of the material.

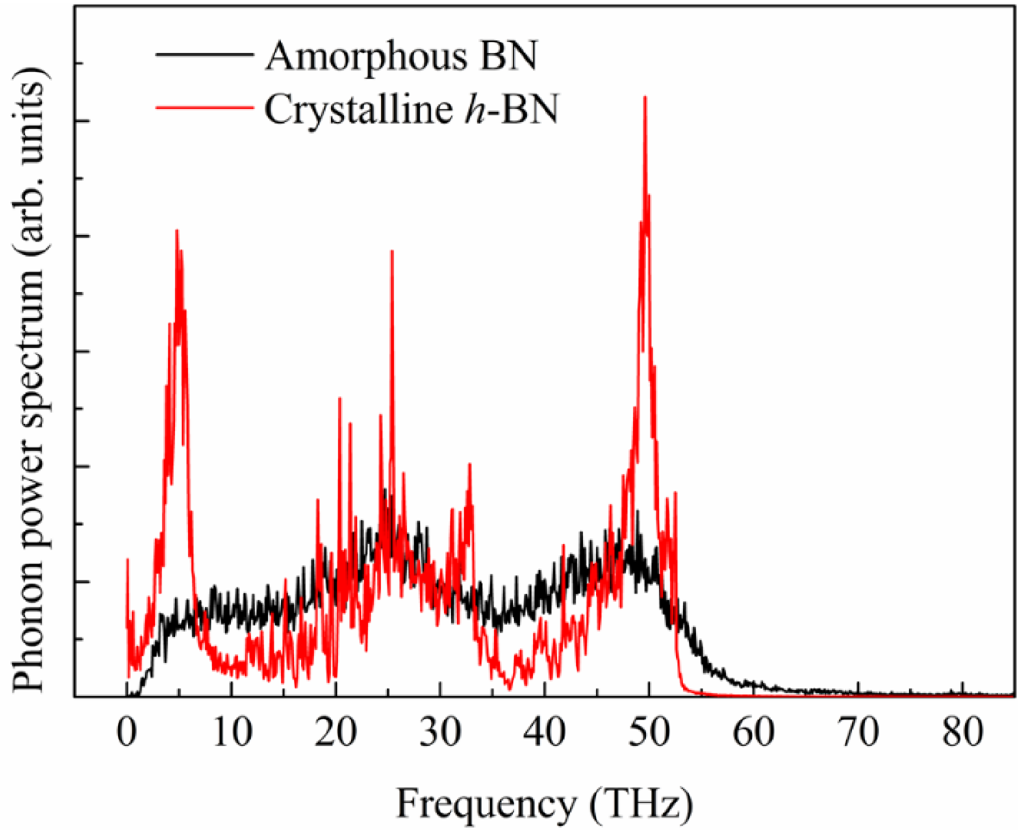

Figure 5.14 - Phonon spectra of the amorphous BN and crystalline h-BN in the 0 to 80 THz bandwidth.[28]

5.3.5 *voBN* thermal crosstalk mitigation

COMSOL Multiphysics was used to showcase how the anisotropic TC of *voBN* could be used to prevent thermal crosstalk in densely packed integrated circuits (ICs). In order to reduce the computing time in the simulation, the system consists only of one unit cell containing one hot spot, with each wall reflecting perfectly the heat (adiabatic conditions) as the neighboring hot spot can be considered as a symmetrical condition.[44] The simulations results are shown using 3D plots of the isothermal contours as shown in Figure 5.15. Their shape gives a good visual clue on the anisotropic thermal conductivity property of *voBN* as seen in Figure 5.15b. Indeed the isothermal contours would stretch in the z direction due to the improve TC in that direction. On the other hand, the isothermal contours exhibit a spherical shape (see Figure 5.15a) when the TC is isotropic, as the heat is spreading in all directions at the same speed. This particular property could be used in the case of heat spread prevention and heat extraction, and its effectiveness is evaluated in these simulations.

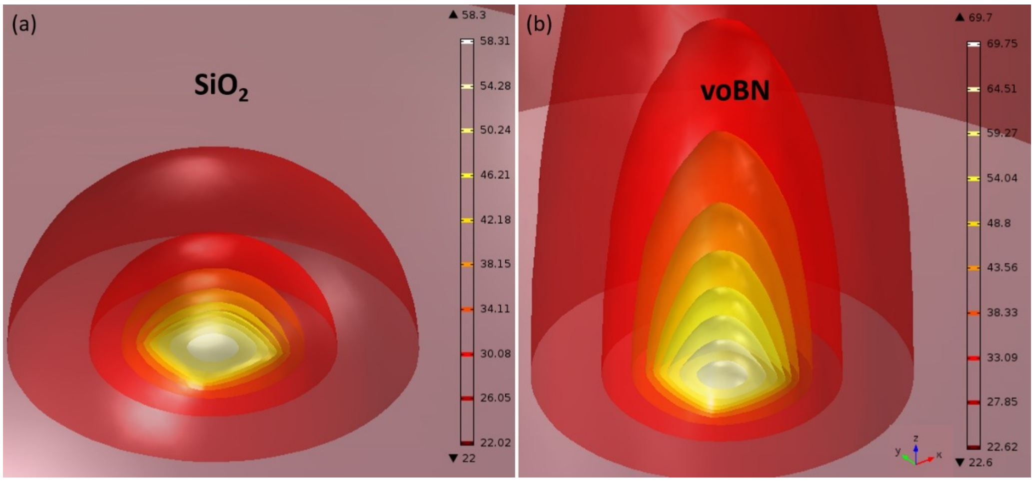

Figure 5.15 - Isothermal contours around the hot spot for SiO$_2$ (a) and *voBN* (b). The spherical contour shape in SiO$_2$ is the typical response from isotropic materials while the stretched contours along the z axis for *voBN* is characteristic of a material with greater thermal conductivity along the z axis compared to the x and y axis.[28]

When switching to a cross section view of the hot spot unit cell, the heat distribution from the hot spot to the unit cell walls can be observed, as seen in Figure 5.16. The schematics in the figure are describing the unit cell (cube) and the cut plane from which the plane view is extracted.

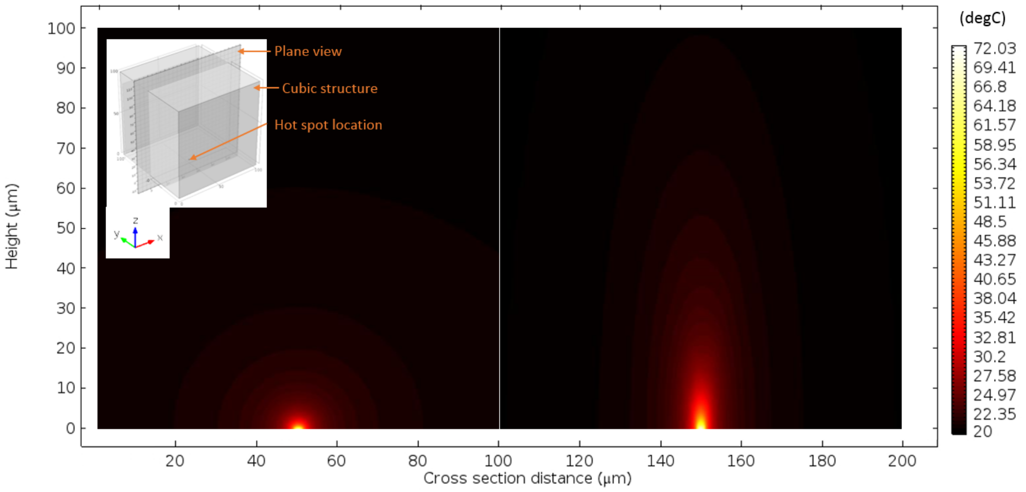

Figure 5.16 - Cross section image (as per the inset image) of the isothermal contours for the temperature response of a hot spot (0.1 W heat source) heating up from the bottom a 100 µm cubic structure. The diagram on the left is for the case of a device made of SiO$_2$ while the one on the right is a device made of *voBN*. The anisotropy of *voBN* induces an elongated temperature response in height, while keeping the in-plane temperature spread more compact compared to SiO$_2$.[28]

The isothermal contours shown in the left part of Figure 5.16 are for the case of using SiO$_2$ to encapsulate the hot spot, while *voBN* is depicted on the right hand side. The impact the anisotropic TC has on the heat propagation in the case of *voBN* can clearly be seen, while SiO_2 isotropic TC produces perfect circles. As expected, the maximum in temperature is located at the hot spot itself while the minimum is at the edge of the unit cell, which is exactly in between two hotspots and is consistent with other similar simulation models.[44, 45] In order to compare how efficient SiO_2 and *voBN* are at preventing heat spreading, the temperature along the line which is equidistant between two hot spots was used as a means of comparison. Figure 5.17c indicates the line in question and inset (a) gives the temperature variation along the line, depending in the height (0 µm being the plane where the hot spot is, and 100 µm being the opposite face of the unit cell which is set to 20 degC as a boundary condition in the simulation). From these plots, it can be seen that for the same unit cell base length of 100 µm, *voBN* is keeping the temperature in between hot spots much lower compared to SiO_2. This means that by using *voBN*, two hot spots could be put closer to each other and produce a thermal crosstalk with the same intensity as a normal 100 µm unit cell with SiO_2. Figure 5.17a shows the optimized values of the unit cell size (the height remains unchanged to 100 µm), and the unit cell can be reduced to as low as 50.3 µm if only the temperature in the hot spot plane has to match the SiO_2 performance, of 54.1 µm if the temperature needs to be equal or lower at any point on the line compared to SiO_2.

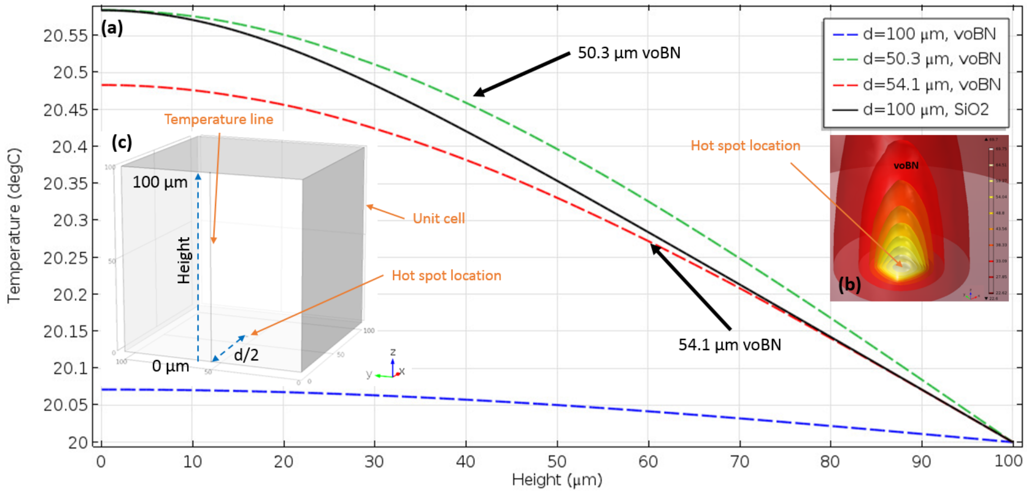

Figure 5.17 - Temperature line plot (inset a) along the temperature line as shown by the vertical dotted arrow located at a distance of d/2 from the hot spot in the unit cell schematic (inset c). The distance d is the square dimensions in the xy plane, which can be seen as the distance between two adjacent hot spots. Each line represents the temperature variation across the 100 µm thick layer, for various hot spot distances. The temperature response of SiO_2 is sandwiched between two *voBN* responses with closer hot spot distances: 50.3 and 54.1 µm. Inset b shows the stretched isothermal contours in the vicinity of a hot spot due to the anisotropic nature of *voBN*.[28]

In the end, the use of *voBN* allows the distance between two hot spots to be decreased while keeping the temperature lower than a similar design with SiO_2. In the basic design, a hot spot would occupy a space of 100 µm x 100 µm, or 10000 $µm^2$. When using *voBN*, the most conservative redesign would put two hot spots 54.1 µm from each other, reducing the unit cell to a surface of 2927 $µm^2$. This provides an improvement of around 242% in hot spot density, at equivalent thermal performance. In the best case scenario (cell size of 50.3 µm), the improvement can go up to almost 300%, meaning that the density of hot spots can be multiplied by 4 with *voBN*, or conversely the area used by the IC can be shrunk 4 times, while maintaining similar thermal characteristics as when using SiO_2.

5.4 Conclusion

In this chapter, the thermal conductivity of *voBN* was fully studied, from the experimental point of view using the 3ω characterization technique as well as through MD simulation. As expected, *voBN* exhibits an anisotropic thermal conductivity with the experimental values found to be 4.26 $W.m^{-1}.K^{-1}$ in the through film direction, and 0.26 $W.m^{-1}.K^{-1}$ in the film plane direction, which is a 16 times ratio between the two directions. Furthermore, the thermal boundary resistance between *voBN* and the silicon substrate was found to be comparable to that of SiO_2 on Si,[46] with a TBR of $0.17x10^8$ $W.m^{-2}.K^{-1}$. The thermal anisotropy was successfully reproduced via Molecular Dynamics simulations and this anisotropic phenomenon explained by the many interfaces between the nanocrystals and the surrounding amorphous regions, creating an increased thermal interface resistance. In addition, *voBN* is made of nanocrystals of h-BN all ordered in the vertical direction, creating a preferred path for phonon propagation in the vertical direction, thus increasing the thermal conductivity in the through film direction. MD simulations also deduced that an increase in crystal size was highly correlated with a possible increase in thermal conductivity, suggesting a possible enhanced thermal performance of *voBN* depending on its grain size. In order to understand how this anisotropy could be used in thermal management of hot spot devices, COMSOL Multiphysics simulations were run to compare the performance of *voBN* compared to that of SiO_2, which is conventionally used in electronics. Thanks to its improved vertical heat extraction capability, *voBN* allows an increase in hot spot density by almost a factor 4 compared to SiO_2, at equal thermal performance. Combining its electrically insulative property (dielectric constant of 8.9), with its enhanced capability in heat extraction in the vertical direction, *voBN* is outperforming the existing dielectric solution in electronics, namely SiO_2. Thanks to its room temperature growth conditions, at wafer scale dimensions, *voBN* is a readily available material that could be used as a passivation layer on active electronics, with an added capability of extracting heat away efficiently.

5.5 References

1. A. J. Lohn, P. R. Mickel and M. J. Marinella, *J. Appl. Phys.*, 2014, **115**, 234507.
2. A. Pirovano, A. Redaelli, F. Pellizzer, F. Ottogalli, M. Tosi, D. Ielmini, A. L. Lacaita and R. Bez, *IEEE Trans. Device Mater. Rel.*, 2004, **4**, 422-427.
3. A. Vassighi and M. Sachdev, *Thermal and Power Management of Integrated Circuits (Integrated Circuits and Systems)*, Springer, New York, 2006.
4. J. Renteria, S. Ramirez, H. Malekpour, B. Alonso, A. Centeno, A. Zurutuza, A. Cocemasov, D. Nika and A. Balandin, *arXiv preprint arXiv:1503.07239*, 2015.
5. M. Tanimoto, T. Yamagata, K. Miyata and S. Ando, *ACS Appl. Mater. Interfaces*, 2013, **5**, 4374-4382.
6. G. Chen, C. L. Tien, X. Wu and J. S. Smith, *J. Heat Transfer*, 1994, **116**, 325-331.
7. I. Ivanov, A. Puretzky, G. Eres, H. Wang, Z. Pan, H. Cui, R. Jin, J. Howe and D. B. Geohegan, *Appl. Phys. Lett.*, 2006, **89**, 223110.
8. C. W. Chang, D. Okawa, A. Majumdar and A. Zettl, *Science*, 2006, **314**, 1121-1124.
9. N. G. Chopra, R. J. Luyken, K. Cherrey, V. H. Crespi, M. L. Cohen, S. G. Louie and A. Zettl, *Science*, 1995, **269**, 966-967.
10. D. Golberg, Y. Bando, C. C. Tang and C. Y. Zhi, *Adv. Mater.*, 2007, **19**, 2413-2432.
11. D. P. Yu, X. S. Sun, C. S. Lee, I. Bello, S. T. Lee, H. D. Gu, K. M. Leung, G. W. Zhou, Z. F. Dong and Z. Zhang, *Appl. Phys. Lett.*, 1998, **72**, 1966-1968.
12. C. Y. Zhi, J. D. Guo, X. D. Bai and E. G. Wang, *J. Appl. Phys.*, 2002, **91**, 5325-5333.
13. D. Golberg, P. M. F. J. Costa, O. Lourie, M. Mitome, X. Bai, K. Kurashima, C. Zhi, C. Tang and Y. Bando, *Nano Lett.*, 2007, **7**, 2146-2151.
14. M. Shakerzadeh, M. K. Samani, N. Khosravian, E. H. T. Teo, M. Bosman and B. K. Tay, *Carbon*, 2012, **50**, 1428-1431.
15. O. Cometto, B. Sun, S. H. Tsang, X. Huang, Y. K. Koh and E. H. Teo, *Nanoscale*, 2015, **7**, 18984-18991.
16. D. G. Cahill and R. O. Pohl, *Physical Review B*, 1987, **35**, 4067-4073.
17. T. Borca-Tasciuc, A. R. Kumar and G. Chen, *Rev. Sci. Instrum.*, 2001, **72**, 2139-2147.
18. T. Sun, M. K. Samani, N. Khosravian, K. M. Ang, Q. Yan, B. K. Tay and H. H. Hng, *Nano Energy*, 2014, **8**, 223-230.
19. B. W. Olson, S. Graham and K. Chen, *Rev. Sci. Instrum.*, 2005, **76**, 053901.
20. Y. Zhang, M. Edwards, M. K. Samani, N. Logothetis, L. Ye, Y. Fu, K. Jeppson and J. Liu, *Carbon*, 2016, **106**, 195-201.
21. M. D. Kluge, J. R. Ray and A. Rahman, *Physical Review B*, 1987, 36, 4234.
22. R. Ranganathan, S. Rokkam, T. Desai and P. Keblinski, *Carbon*, 2017, 113, 87-99.
23. M. Ishimaru, S. Munetoh and T. Motooka, *Physical Review B*, 1997, 56, 15133.
24. C. Tomas, I. Suarez-Martinez and N. A. Marks, *Carbon*, 2016, 109, 681-693.
25. F. Li and J. S. Lannin, *Phys. Revi. Lett.*, 1990, 65, 1905-1908.
26. D. G. McCulloch, D. R. McKenzie and C. M. Goringe, *J. Appl. Phys.*, 2000, 88, 5028.
27. D. R. McKenzie, D. Muller and B. A. Pailthorpe, *Phys. Rev. Lett.*, 1991, 67, 773-776.
28. O. Cometto, M. K. Samani, B. Liu, S. Sun, S. H. Tsang, J. Liu, K. Zhou and E. H. Teo, *ACS Appl Mater Interfaces*, 2017, DOI: 10.1021/acsami.6b15014.
29. L. Lindsay and D. A. Broido, *Physical Review B*, 2011, 84, 155421
30. J. Tersoff, *Physical Review B*, 1989, **39**, 5566-5568.
31. K. Matsunaga, C. Fisher and H. Matsubara, *Japanese Journal of Applied Physics*, 2000, **39**, L48-L51.
32. A. K. Rappe, C. J. Casewit, K. S. Colwell, W. A. Goddard and W. M. Skiff, *J. Am. Chem. Soc.*, 1992, **114**, 10024-10035.

33. T. A. Friedmann, K. F. McCarty, E. J. Klaus, J. C. Barbour, W. M. Clift, H. A. Johnsen, D. L. Medlin, M. J. Mills and D. K. Ottesen, *Thin Solid Films*, 1994, **237**, 48-56.
34. R. Geick, C. H. Perry and G. Rupprecht, *Physical Review*, 1966, **146**, 543-547.
35. W. Dworschak, K. Jung and H. Ehrhardt, *Thin Solid Films*, 1995, **254**, 65-74.
36. B. Yang, W. L. Liu, J. L. Liu, K. L. Wang and G. Chen, *Appl. Phys. Lett.*, 2002, **81**, 3588-3590.
37. K. Kurabayashi, M. Asheghi, M. Touzelbaev and K. E. Goodson, *J. Microelectromech. Syst.*, 1999, **8**, 180-191.
38. A. Bagri, S.-P. Kim, R. S. Ruoff and V. B. Shenoy, *Nano Letters*, 2011, **11**, 3917-3921.
39. Y. Zhou, B. Anglin and A. Strachan, *Journal of Chemical Physics*, 2007, **127**.
40. B. Liu, J. A. Baimova, C. D. Reddy, S. V. Dmitriev, W. K. Law, X. Q. Feng and K. Zhou, *Carbon*, 2014, **79**, 236-244.
41. B. Liu, C. D. Reddy, J. Jiang, H. Zhu, J. A. Baimova, S. V. Dmitriev and K. Zhou, *J. Phys. D: Appl. Phys.*, 2014, **47**, 165301.
42. B. Liu, F. Meng, C. D. Reddy, J. A. Baimova, N. Srikanth, S. V. Dmitriev and K. Zhou, *RSC Adv.*, 2015, **5**, 29193-29200.
43. B. Liu, C. D. Reddy, J. Jiang, J. A. Baimova, S. V. Dmitriev, A. A. Nazarov and K. Zhou, *Appl. Phys. Lett.*, 2012, **101**, 211909.
44. Y. Han, B. L. Lau, X. Zhang, Y. C. Leong and K. F. Choo, *IEEE Trans. Compon. Packag. Manuf. Technol.*, 2014, **4**, 983-990.
45. B. Jie, E. Michael, H. Shirong, Z. Yong, F. Yifeng, L. Xiuzhen, Y. Zhichao, J. Kjell and L. Johan, *J. Phys. D: Appl. Phys.*, 2016, **49**, 265501.
46. J. Zhu, D. Tang, W. Wang, J. Liu, K. W. Holub and R. Yang, *J. Appl. Phys.*, 2010, **108**, 094315.

Chapter 6 – Texturing CN and its thermal properties

6.1 Introduction

6.1.1 Rationale

Carbon nitride (CN) materials have attracted a lot of interest since Liu and Cohen predicted in 1990 that the β-C_3N_4 phase of carbon nitride could outperform diamond in hardness[1-2] as well as exhibit a high thermal conductivity.[3] Since then, many research groups have attempted the synthesis of the β metastable phase with only very limited results, with one only having obtained nano-sized crystallites.[4] At the same time, amorphous CN (a-CN) films have been studied extensively as nitrogen implantation in an amorphous carbon matrix proved to improve both the hardness (a hardness of up to 60 GPa has been reported[5]) and the elastic behaviour of the film (≈90% recovery) substantially.[6-7] In the past, CN films have been deposited using various techniques which can be derived in two categories: deposition of carbon in a N_2 reactive environment and direct nitrogen implantation. The former uses techniques such as direct current magnetron sputtering (DCMS),[7] RF sputtering,[8] ion plating[9] or Pulsed Laser Deposition[10] while the latter consists of deposition methods such as Ion Vapor Deposition (IVD)[11] or Ion Beam Assisted Deposition (IBAD).[12-13] The common aspect about those methods is that they all failed to produce the β-C_3N_4 phase. More information on the CN growth can be found in the literature review chapter. In addition, it can be noted that the maximum N ratio reported in the literature using N_2 reactive techniques would be 35 at.%[14] while ion implantation methods would go as high as a 50%.[15] In an attempt to understand how to obtain the various phases for a-

CN better, Hellgren et al.[14] created a diagram based on the growth temperature and the nitrogen film concentration (see Figure 6.1), concluding that amorphous CN films could only be obtained for deposition temperatures below 200 degC, while higher temperatures would yield graphitic-like or fullerene-like films. In addition, it is interesting to note that the diagram does not allow a nitrogen concentration of above 25 at.% and this is explained by the effect of chemical sputtering where volatile molecules such as N_2 and C_xN_y are being formed at the surface of the film during growth and contribute to lower the nitrogen content.[16]

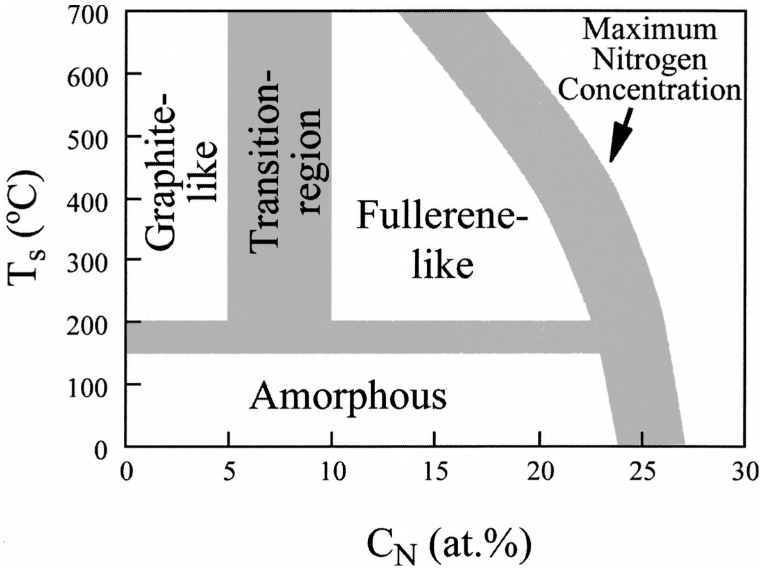

Figure 6.1 - Phase diagram of CNx for varying deposition temperature and nitrogen film concentration for reactive deposition techniques.[14]

6.1.2 Work performed

In this study, we are considering a novel way of growing CN films by using High Power Impulse Magnetron Sputtering (HiPIMS), using a carbon target reactively sputtered in nitrogen gas. HiPIMS is a relatively recent physical vapour deposition (PVD) method introduced by Kouznetsov et al. in 1999.[17] It is of interest here as it can produce high power densities at the sputtered target surface, thus enhancing the deposition rate and the ionization rate of the plasma, facilitating bonding with nitrogen. As explained in the literature review, amorphous CN (or CN_x) thin films were extensively studied for their tribological properties but no data was ever gathered on their thermal performance. CN_x thin films have a unique nanostructuring variation, in particular the fullerene-like structure which does not exist in pure carbon thin films. Here, various thin films were grown on silicon substrate, such as amorphous carbon and carbon nitride as well as nanocrystalline C and CN with vertical ordering. Their thermal diffusivity was computed using thermal grating spectroscopy (TGS) in order to compare the impact of the material's nanostructure on its thermal property as well as benchmarking the performance of CN and assess the impact of nitrogen on thermal performances, as it has never been reported before.

6.2 Experimental setup

6.2.1 Sample preparation

A high-power impulse magnetron sputtering (HiPIMS) was used to grow the samples using a 3" carbon target of purity 99.995%. The carbon film was obtained by sputtering the carbon target with argon while the CN samples would be reactively sputtered in a mixture of argon and nitrogen. The chamber was pumped down until the base pressure reached a pressure below 1x10^{-6} mbar and would rise up to 3-5x10^{-3} mbar during deposition due to the combined gas flow of argon and nitrogen injected in the chamber to initiate the glow discharge plasma. The pulsed current supplied to the magnetron was generated by a Hipster 1 power supply from Ionautics. In order to obtain the required samples, which are amorphous carbon, amorphous carbon nitride, vertically ordered nanocrystalline graphite and vertically ordered nanocrystalline carbon nitride, many different recipes for the growth have been tried and only the successful ones have been kept for this study. The recipes are displayed in the table in Figure 6.2 below:

	Sample name	**Gas mixture (sccm)**	**Growth pressure (mbar)**	**Temp. (degC)**	**Bias volt. (V)**	**Pulse current (A)**	**Pulse freq. (Hz)**	**Pulse volt. (V)**	**Peak power density (W.cm^{-2})**
Amorphous carbon	aC	Ar:32	3.7x10^{-3}	25-80	0	22	4000	750	180
Nanocrystalline graphite with vertical ordering	NCG	N/A	Below 1x10^{-5}	600	200	N/A	N/A	N/A	N/A
Amorphous carbon nitride	aCN	N:40	6.8x10^{-3}	25-45	0	28	4000	650	122
Nanocrystalline graphitic carbon nitride with vertical ordering	flCN (fullerene -like CN	Ar:32 N:8	4.5x10^{-3}	350	500	1	4000	535	29

Figure 6.2 - Summary of the successful recipes used for the growth of carbon and carbon nitride thin films. All films are grown using HiPIMS except the NCG sample which was grown using FCVA based on a technique reported elsewhere.[18]

It can be observed from the above Figure 6.2 that the room temperature growths have an actual temperature ranging from 25 degC at the beginning, after which the temperature climbs up to almost 100 degC due to the plasma power heating up the sample. In addition, the growth time was varied depending on the samples so that all samples have the same thickness of around 150 nm (more or less 10 nm), except for NCG which was obtained using another growth method (FCVA) and was only 90-100nm thick.

6.2.2 Sample characterization

Raman spectroscopy (Witec 300) was used to determine the film structure, using a laser wavelength of 532 nm. The laser power was kept to a minimum as the thin films grown tended to get laser annealed (especially the amorphous films) and the data acquisition time was increased to compensate the low laser power. Several spectra were taken from 900cm^{-1} to 1900cm^{-1} for a duration of 30 seconds each and the results were averaged in order to lower the noise to a minimum. Special care was made to ensure that the film was not damaged in any way by the laser after each measurement. The treatment on the Raman response was done using OriginPro 9 SR2 with its Peak Analyzer module and was based on the work done by Ferrari et al.[19] which consists of the three-stage model for carbon,[20] where the change in G peak position and the ratio of intensity between the G and D peaks give information on the nanocrystalline structure of the film. The deconvolution of the signal is based on a Lorentzian function for the D peak, while the G peak is modelled by a Breit-Wigner-Fano (BWF) function. The maximum intensity for both the BWF and Lorentzian functions was used for the I(D)/I(G) ratio computation. In order to verify the Raman findings, the samples' cross section by the same process as explained in chapter 4: FIB milling was used to obtain slices of the samples and HRTEM (Tecnai F20) was used to image the cross section. The samples' nitrogen content as well as their sp^2 to sp^3 ratio was also computed.

6.2.3 Transient Grating Spectroscopy

Transient Grating Spectroscopy (TGS) was used to measure the thermal diffusivity of the films. TGS has been around for almost two decades and is based on heterodyne detection using gratings created by laser pulses.[21] Such gratings would generate surface acoustic waves (SAW) on the surface of the film and their decay is measured by a continuous probe laser. SAWs decay both acoustically and thermally and the thermal decay gives information on the effective thermal diffusivity of the material measured. A laser, with an excitation spot of around 225 µm rasterized on the film surface with a wavelength of 7.41 µm, was used. The measurement was performed in near vacuum (roughly 15 mTorr) in order to avoid the interference of air in the measurements. The TGS setup is described elsewhere and will not be discussed here.[22] Each sample was measured 10 times in order to minimize background noise and thus reduce the standard deviation for each measurement. The first measurement is performed on a known tungsten substrate to calibrate the system. From there, by computing the SAW decay rate for the samples, the effective thermal diffusivity of the film-substrate system is computed by using curve fitting.

6.3 Results and discussion

6.3.1 Microstructure analysis

The 4 samples described in the section above have been analyzed using the TEM. Figure 6.3 shows a high resolution cross section image of both amorphous carbon and amorphous carbon nitride thin films. The TEM images show a fully amorphous structure for both samples, with no identifiable atomic pattern. In addition, EELS measurements were performed to identify the sp^2 content of each film, which was computed to be 81% and 93% for the aC and aCN films respectively. EELS provided extra information on the nitrogen content for the aCN sample, with a nitrogen at.% of 14.79%.

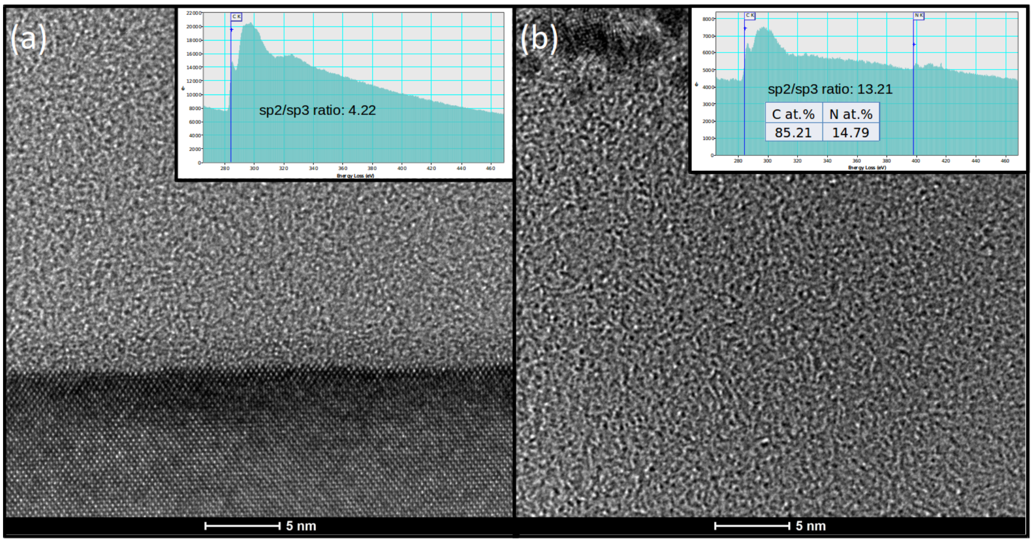

C at.%	N at.%
85.21	14.79

Figure 6.3 - (a) A cross-section TEM of an amorphous carbon film. EELS measurements give a 81% sp^2 content in the film. (b) FIBTEM of an amorphous carbon nitride film. EELS measurements give a 93% sp^2 content in the film and an at.% of C and N of respectively 85.21% and 14.79%.

In the same fashion as for the amorphous samples, the cut view of the NCG and flCN samples were analyzed with HRTEM and the results are displayed in Figure 6.4. Unlike the amorphous samples, some nano crystal ordering can be observed for both samples, which is validated by the 002 fringes seen in the computed FFT added at the top right corner of each TEM image. Figure 6.4a shows the cross-sectional view for the

NCG sample, which is made of graphitic planes with vertical orientation. The FFT inset displays two partial circles aligned horizontally, indicating a vertical ordering with a cycle of 0.34 nm, which corresponds to the 002 graphitic plane with vertical orientation. Figure 6.4b is an HRTEM image of the flCN sample, which displays less ordering than the NCG sample. This fullerene-like structure seen here is due to the extra nitrogen atom which disrupts the graphitic structure. Indeed, in a pure carbon film, each hexagonal ring is made of six carbon atoms and the planes are able to grow in a linear fashion. In the case of carbon nitride growth, the introduction of nitrogen in the film disrupts the planar growth of the graphitic planes, as nitrogen atoms replace some carbon atoms in the hexagonal structure, increasing the sp^3 content and sometimes changing the structure from hexagonal to pentagonal, which induces a buckling of the planes and generates this fullerene-like structure observed in the TEM image here.[5, 16] The FFT image of the flCN TEM image shows a ring indicating a cyclical pattern with random orientation and an average interplanar spacing of 0.44 nm. The expected inter-planar distance for CN is supposed to be the same as carbon (i.e. 0.33 nm) and the increased value obtained here might be due to the buckling which prevents an optimal stacking of the planes. EELS measurements showed a nitrogen content of 22.18 at.% for the flCN sample.

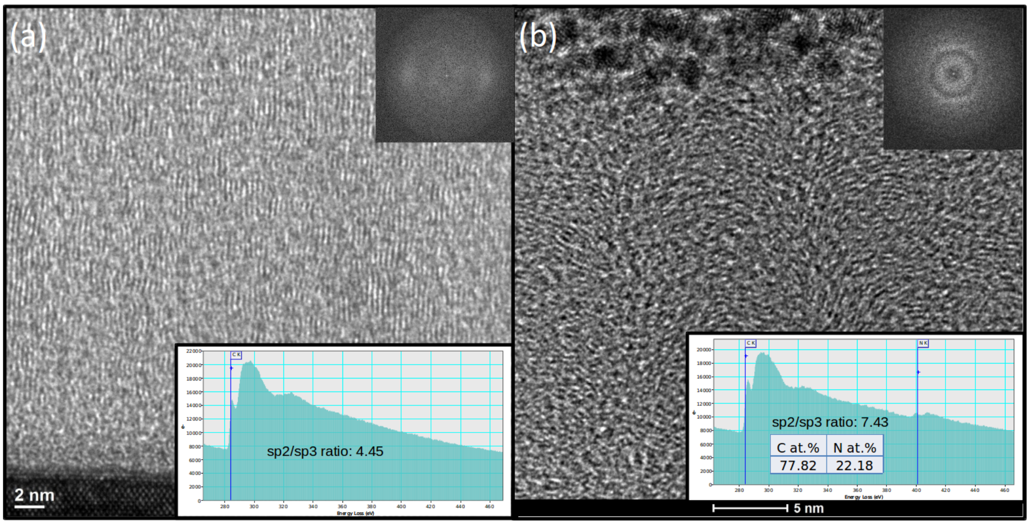

Figure 6.4 - (a) A cross-section TEM of the NCG film with a 82% sp2 content. The computed FFT image in the inset at the top of the image shows partial circles indicating an interplanar distance of 0.34 nm corresponding to the 002 direction. (b) FIBTEM of the fullerene-like carbon nitride film. EELS measurements give a 88% sp2 content in the film with an at.% of C and N of 77.82% and 22.18% respectively. The inset located on top is showing the computed FFT of the image and its circle indicating an interplanar distance of 0.44 nm.

As TEM provides only information on a very small local zone, Raman was performed to corroborate the results and confirm that the film structure is homogeneous across the whole sample. Figure 6.5 shows the Raman response for the NCG sample and its curve fitting computation. As explained before, the D peak was fitted with a Lorentzian function while a BWF function would be used to fit the G peak. Once the closest fitting is achieved, the maximum of both curves is used to compute the I(D)/I(G) ratio and G peak centre would be obtained by taking the wavenumber of the BWF function maximum. In the case of NCG, the ratio is 1.28 and the G peak centre is located at 1585 cm^{-1}. Using the three-stage model devised by Ferrari and Robertson,[20] a fairly close estimate of the carbon film nanostructure can be deduced as such I(D)/I(G) ratio and G peak location falls in between Stage 1 and Stage 2 which is the characteristic response for nanocrystalline graphite (thus with 100% sp^2 content), which is in agreement with the TEM images. However, the orientation of those crystals cannot be deduced from the Raman response and only the TEM images can determine the vertical ordering.

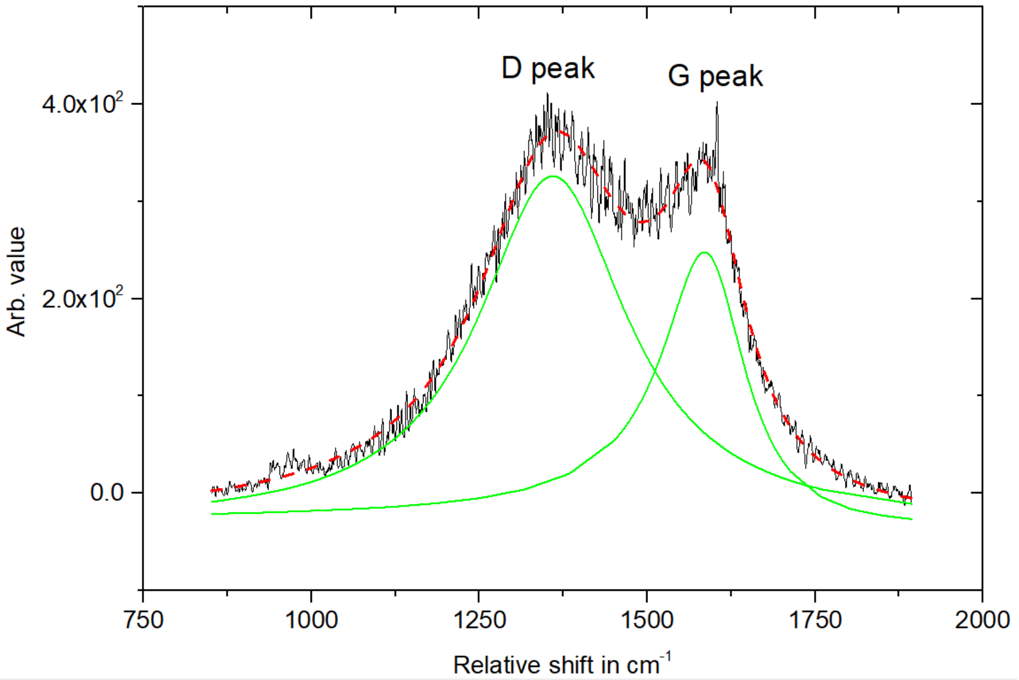

Figure 6.5 - Raman spectrum of the NCG sample (noisy line) and its curve fitting in thick green color (Lorentzian for the D peak and BWF for the G peak). The red dotted line is the sum of both the Lorentzian and BWF fit which is a close match to the actual Raman response. I(D)/I(G) is 1.28 and the G peak centre is 1585 cm^{-1}.[28]

In the same way as for NCG, the other samples were characterized with Raman and their Raman response is shown in Figure 6.6. The G peak shift and the I(D)/I(G) peak ratio are used to determine the film crystallinity. For instance, for amorphous carbon, the obtained peak ratio is 0.67 with a G peak center at 1565 cm^{-1}. This corresponds to early Stage 2, indicating a film made of amorphous carbon with high (around 90%) sp^2 content. For CN films, the three-stage model differs slightly due to the introduction of nitrogen in the film. Ferrari et al. adapted the model for CN[19] and that new model was used to interpret the Raman response for the amorphous and fullerene-like CN samples. The former showed a peak ratio of 0.97 and a G peak center of 1570 cm^{-1} while the latter had a higher ratio of 1.17 with a G peak center of 1564 cm^{-1}. According to the three-stage model for CN, the first results confirmed the presence of an amorphous film with high sp^2 content (around 90%), while a higher peak ratio and a shift of the G peak towards lower wavenumbers means that the film tends to contain more graphitic nanocrystals while keeping a similar amount of sp^2 content. As for the

NCG sample, no conclusions can be drawn on the crystalline orientation of the graphitic planes from the Raman measurements.

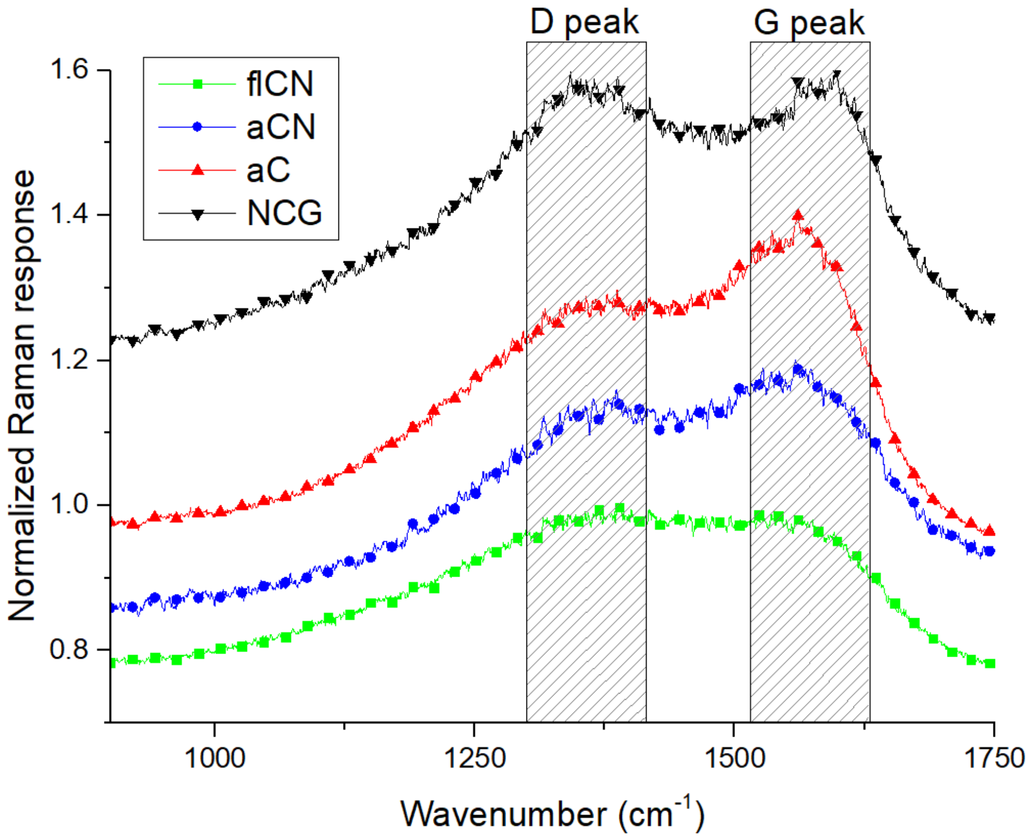

Figure 6.6 - Raman spectra for all 4 samples. The D and G peak regions are shown in here. Each spectrum shows a different shift for the G peak, which is a clue to the nanocrystalline structure of the film.[28]

Overall, the Raman spectroscopy measurements confirmed what was observed during TEM on a larger scale as each spectrum contains the crystalline structure from the laser spot size (around a few hundred micrometres), and the characterization can be easily scaled up by measuring at various locations on the film or performing a Raman mapping across the surface.

6.3.2 Thermal diffusivity analysis

Once the films' nanostructure was characterized, TGS measurements were performed on them in order to extract some information about thermal design. Figure 6.7 shows the SAW decay curves obtained for all 4 samples. From this information, the thermal diffusivity can be obtained by fitting the curves with the theoretical equations as explained below.

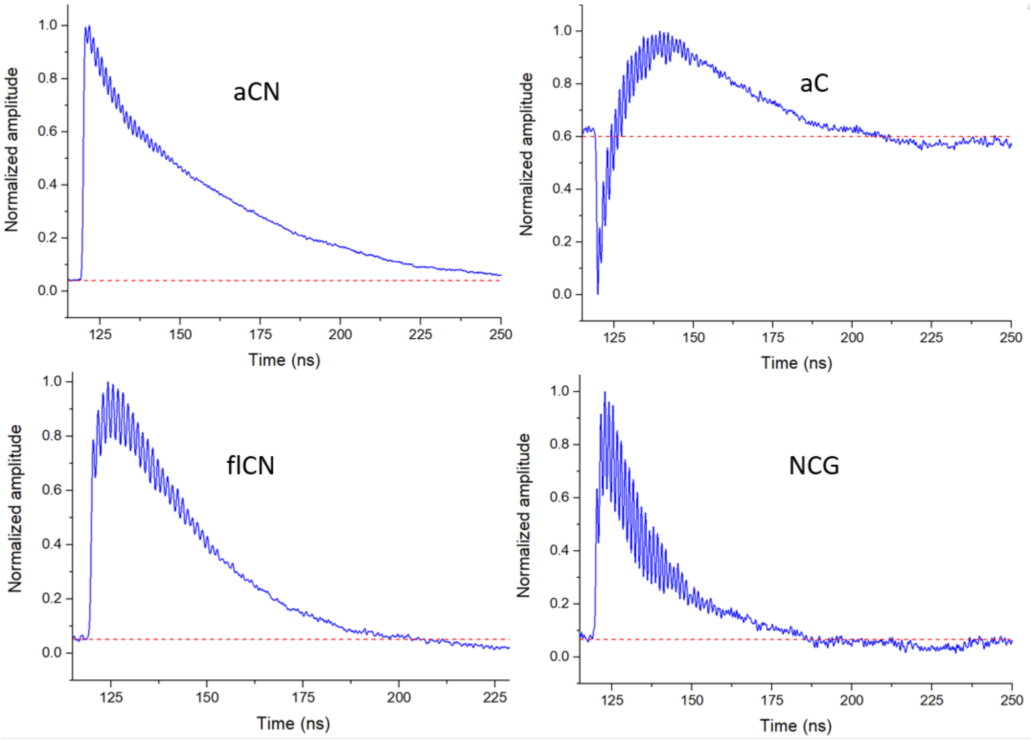

Figure 6.7 - Surface acoustic waves decay after excitation by the grating. The exponential decay curve is input into a fitting model in order to compute the thermal diffusivity of the film-substrate system. The small sinusoidal oscillations are due to the elastic properties of the material. The dashed line in each plot is the zero line.[28]

For the thermal decay analysis, the method used is described by Kading et al.[23] where the temperature evolution in the system is described by Fourier's Law extended in several dimensions as shown in equation 6.1:

$$\rho c \frac{\partial \Delta T}{\partial t} - k_x \frac{\partial \Delta T}{\partial x^2} - k_z \frac{\partial \Delta T}{\partial z^2} = Q_0 \cos\left(\frac{2\pi}{L} x\right) e^{-z/\zeta} \delta(t) \qquad (6.1)$$

ρ is the film density, c its heat capacity, ΔT is the variation of temperature from the initial temperature, k_x and k_z are the thermal conductivities respectively in the plane and cross plane directions, Q_0 is the total amount of energy transmitted by the laser pulse while the pulse itself is described by the $\delta(t)$ function. L is the grating size and ζ is the penetration depth of the laser. Equation 6.1 can be further transformed by using a set of assumptions deemed valid in this case, such as the sinusoidal spatial dependence of T on the surface of the film, and since we are only interested in what happens at the film surface, we can take $z=0$. Finally, the temperature evolution of the film surface when excited by a short laser pulse can be written as, as seen in equation 6.2:

$$T(z=0,x,t)=\frac{A\zeta}{\sqrt{\pi}}(\alpha_z t)^{-1/2}\cos\left(\frac{2\pi}{L}x\right)e^{-\alpha_x\left(\frac{2\pi}{L}\right)^2 t} \qquad (6.2)$$

From equation 6.2, it can be deduced that the decay itself is not dependant on α_z as changing its value is equivalent to changing the signal amplitude A . Fitting the exponential decay curves in Figure 6.7 with equation 6.2 yields the value of α_x as it is the only variable that can be changed to improve the fitting. Once the fitting is achieved, the different values for the in plane thermal diffusivity α_x are shown in Figure 6.8.

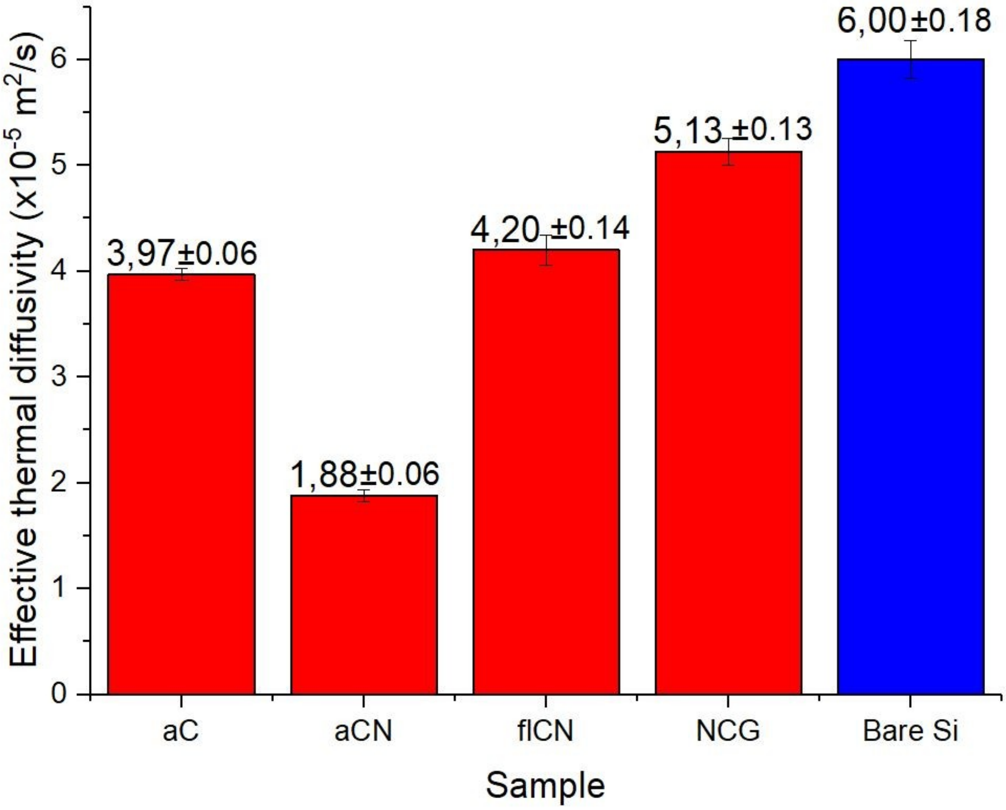

Figure 6.8 - Thermal diffusivity value for each sample. As the excitation wavelength is 7.4 µm deep, the thermal diffusivity value is made of a two-layer system made of the 150 nm thick C or CN film + several microns of silicon 100, which has a thermal diffusivity of around 6x10^{-5} m^2/s.[28]

The thermal diffusivity results in Figure 6.8 show that all 4 samples, which are made of silicon with a thin layer (around 100-150 nm) of carbon/carbon nitride, exhibit a lower thermal diffusivity compared to a bare silicon wafer. This could be due to the poorer thermal performance of the thin films compared to the silicon substrate, as well as the additional thermal interface between both layers, inducing thermal resistance. As the laser excitation wavelength is 7.41 µm, the majority of the thermal diffusivity contribution will come from the silicon substrate which means that aCN, which is able to divide the result by 3 with just a layer 150 nm thick, has the potential to be an excellent thermal isolator. As the film thicknesses are small compared to the depth of excitation (which is in the order of the excitation wavelength of several microns), they can be considered the same, which allows a direct thermal diffusivity comparison between them. When comparing aC and aCN, it can be noted that introducing nitrogen in the film halves the diffusivity, which is likely due to the increased disorder introduced by the incorporation of nitrogen. As expected and previously observed,[24] NCG thermal performance is better than aC, thanks to its fully sp^2 hybridized matrix of basal planes, facilitating phonon transport along the hexagonal structure, whereas aC amorphous nature provides no clear path for phonons, and gets dispersed while propagating. On the other hand, a similar conclusion cannot be reached for aCN and flCN. In this case, both films have approximately the same amount of sp^2 bonding in the film, and the only difference is their nanostructure where flCN exhibits more ordering with, to some extent, vertical alignment. Finally, both films with improved crystalline ordering (NCG and flCN) perform better than their amorphous counterpart. However, the addition of nitrogen in the film degrades performance in both crystalline and amorphous cases, as it introduces additional disorder in the film structure. It can also be noted that due to the amorphous nature of the aC and aCN samples, their thermal diffusivity is anisotropic by essence so the planar diffusivity computed with equation 6.2 works in all directions. The same cannot be concluded for flCN and NCG as their microstructure will most likely create an anisotropy in thermal conductivity, as seen in the case of the vertically aligned boron nitride thin films.[25]

Until now, the discussion on the thermal performance of the samples was focused solely on the nanostructure, which is equivalent to the phonon transport in the material. However, electrons, similarly to phonons, can transport heat and this effect carries the name of the empirical Wiedemann–Franz law[26] for metals and it is understood in general that increased electrical conductivity will lead to an increased thermal conductivity. Figure 6.9 shows the electrical sheet resistance for the 4 samples, with the sheet resistance axis written in a logarithmic scale. It can be seen that aC and aCN, which have a sheet resistance several orders of magnitude higher than flCN and NCG, indeed have a lower thermal diffusivity. However, the thermal diffusivity of aCN is also much lower than aC, while having an electrical sheet resistance 4 orders of magnitude better. This contradicts the Wiedemann–Franz law and implies that the nanostructure and phonon transport plays a dominant role in the thermal conductivity in this case, meaning that the nitrogen doping in the aCN sample plays a key role in lowering the thermal diffusivity.

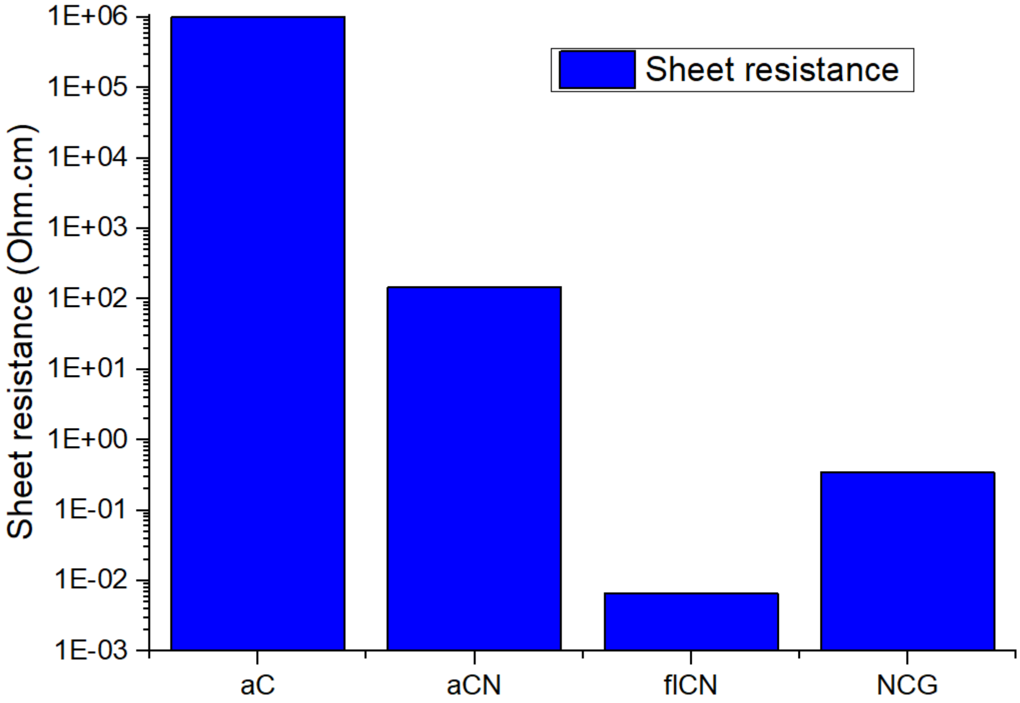

Figure 6.9 - Sheet resistance measurement on all 4 samples. The y axis is in log scale to account for the wide range in measurements between the amorphous and graphitic samples.

As explained before, Figure 6.8 provides only the in-plane thermal diffusivity for the substrate-thin film sample. However, this two-layer system is well understood[27] and both layers can be independently resolved based on the thermal resistance for two layers in series given in equation 6.3:

$$\frac{l}{k}=\frac{l_1}{k_1}+\frac{l_2}{k_2} \quad (6.3)$$

l and k refer to the thickness and thermal conductivity of the whole film-substrate system respectively, while l_i and k_i refer to the individual thickness and thermal conductivity of layer i. At the same time, the effective heat capacity of the film-substrate system is given by equation 6.4:

$$\varrho V c = \varrho_1 V_1 c_1 + \varrho_2 V_2 c_2 \qquad (6.4)$$

ϱ is the density, V the total material volume and c the specific heat of the material. The index i specifies either the material 1 or 2 which stands for the thin film and the substrate. Using equations 6.3 and 6.4, the effective thermal diffusivity of the whole film-substrate system is given by equation 6.5:

$$\alpha = \frac{1}{x^2/\alpha_1 + \left(1 - x^2\right)/\alpha_2 + x\left(1 - x\right)\left(\lambda/\alpha_1 + 1/\lambda\,\alpha_2\right)} \qquad (6.5)$$

$x = l_1/l$ which is the thickness fraction of the thin film compared the total thickness of the thin film + substrate. λ is the ratio between k_1 and k_2 . Equation 6.5 shows that the system's thermal diffusivity not only depends on the thickness ratio x , it also relies on the thermal conductivity ratio λ . In our case, λ is unknown as we do not have the value of k_1 (k_2 is known and can be found easily in the literature), and α_1 is unknown as well. Those two parameters are linked by equation 6.6:

$$\alpha_1 = \frac{k_1}{\rho_1 c_1} \qquad (6.6)$$

ρ_1 and c_1 are the density and the specific heat capacity of the thin film respectively and are unknown here, which means that α_1 and k_1 have to be considered as 2 independent variables. Because of this, equation 6.5 is insufficient to solve the value for either unknown, and an additional data point is required, by changing the ratio x for instance, so as be able to solve the system.

6.4 Conclusion

Pure carbon and carbon nitride films with different crystalline structures were studied using TGS. The thermal diffusivity results obtained show a similar trend between the carbon and CN films, which is a decrease of diffusivity for amorphous films compared to the graphitic ones, while the CN films would show results inferior to the pure carbon films, most likely due to the additional nitrogen atoms disrupting the crystalline quality of the films, hence limiting the phonon transport. The lack of data on the TGS results and the limited number of samples with various nitrogen contents limited the study scope. No actual thermal conductivity value for the materials themselves was measured, and little is known about the role of nitrogen on the thermal performance and how it impacts it. However, it was also shown that the electrical conductivity of the films is not correlated to the thermal diffusivity results, implying that the key actor in the thermal diffusivity reduction in the case of the carbon nitride thin films comes from the addition of nitrogen in the nanostructure. This is the first time some thermal related study on CN has been performed and that the impact of nitrogen on the thermal diffusivity has been demonstrated.

6.5 References

1. Sung, C.-M.; Sung, M., Mater. Chem. Phys. 1996, 43, 1-18.
2. Liu, A. Y.; Cohen, M. L., Physical Review B 1990, 41, 10727-10734.
3. Morelli, D. T.; Heremans, J. P., Appl. Phys. Lett. 2002, 81, 5126-5128.
4. Yin, L.-W.; Li, M.-S.; Luo, G.; Sui, J.-L.; Wang, J.-M., Chem. Phys. Lett. 2003, 369, 483-489.
5. Sjöström, H.; Stafström, S.; Boman, M.; Sundgren, J. E., Phys. Rev. Lett. 1995, 75, 1336-1339.
6. Li, D.; Chung, Y. W.; Wong, M. S.; Sproul, W. D., J. Appl. Phys. 1993, 74, 219-223.
7. Broitman, E.; Hellgren, N.; Wänstrand, O.; Johansson, M. P.; Berlind, T.; Sjöström, H.; Sundgren, J. E.; Larsson, M.; Hultman, L., Wear 2001, 248, 55-64.
8. Cuomo, J. J.; Leary, P. A.; Yu, D.; Reuter, W.; Frisch, M., Journal of Vacuum Science & Technology 1979, 16, 299-302.
9. Taki, Y.; Kitagawa, T.; Takai, O., Thin Solid Films 1997, 304, 183-190.
10. Yap, Y. K.; Kida, S.; Aoyama, T.; Mori, Y.; Sasaki, T., Appl. Phys. Lett. 1998, 73, 915-917.
11. Fujimoto, F.; Ogata, K., Japanese Journal of Applied Physics 1993, 32, L420-L423.
12. Kohzaki, M.; Matsumuro, A.; Hayashi, T.; Muramatsu, M.; Yamaguchi, K., Thin Solid Films 1997, 308–309, 239-244.
13. Bousetta, A.; Lu, M.; Bensaoula, A.; Schultz, A., Appl. Phys. Lett. 1994, 65, 696-698.
14. Hellgren, N.; Johansson, M. P.; Broitman, E.; Hultman, L.; Sundgren, J.-E., Physical Review B 1999, 59, 5162-5169.
15. Ogata, K.; Chubaci, J. F. D.; Fujimoto, F., J. Appl. Phys. 1994, 76, 3791-3796.
16. Hultman, L.; Neidhardt, J.; Hellgren, N.; Sjöström, H.; Sundgren, J.-E., MRS Bull. 2003, 28, 194-202.
17. Kouznetsov, V.; Macák, K.; Schneider, J. M.; Helmersson, U.; Petrov, I., Surf. Coat. Technol. 1999, 122, 290-293.
18. Teo, E. H. T.; Kulik, J.; Kauffmann, Y.; Kalish, R.; Lifshitz, Y., Appl. Phys. Lett. 2011, 98.
19. Ferrari, A. C.; Rodil, S. E.; Robertson, J., Physical Review B 2003, 67, 155306.
20. Ferrari, A. C.; Robertson, J., Physical Review B 2000, 61, 14095-14107.
21. Maznev, A. A.; Nelson, K. A.; Rogers, J. A., Opt. Lett. 1998, 23, 1319-1321.
22. Dennett, C. A.; Short, M. P., Appl. Phys. Lett. 2017, 110, 211106.
23. Kading, O. W.; Skurk, H.; Goodson, K. E., Appl. Phys. Lett. 1994, 65, 1629-1631.
24. Shakerzadeh, M.; Samani, M. K.; Khosravian, N.; Teo, E. H. T.; Bosman, M.; Tay, B. K., Carbon 2012, 50, 1428-1431.
25. Cometto, O.; Samani, M. K.; Liu, B.; Sun, S.; Tsang, S. H.; Liu, J.; Zhou, K.; Teo, E. H., ACS Appl Mater Interfaces 2017, 9 (8), 7456-7464.
26. Franz, R.; Wiedemann, G., Annalen der Physik 1853, 165, 497-531.
27. Lucio M, J. L.; Alvarado-Gil, J. J.; Zelaya-Angel, O.; Vargas, H., physica status solidi (a) 1995, 150, 695-704.
28. Cometto, O.; Dennet, C. A.; Tsang, S. H.; Short, M. P.; Teo, E. H., Carbon 2018, 130, 355-361.

Chapter 7 – Conclusion and recommendations

The work encompassing this thesis will be summarized in this final chapter and conclusions will be drawn from the work produced during the four years of my PhD candidature. The objectives stated at the beginning of this thesis were outlined in three main sections: the setup of a new growth method for BN and CN based on HiPIMS, the growth and study of *voBN* and flCN and finally the in-depth anisotropic thermal study of *voBN*.

The first objective of this PhD project was to set up, learn and understand the basic principles of HiPIMS based growth techniques. Once the initial HiPIMS setup was commissioned and tested, a proof of concept for growth of BN and CN using HiPIMS was completed. In addition, the system was upgraded and modified to increase reliability and repeatability. The HiPIMS growth method has never been used before to grow BN and CN. Achieving such a milestone can open paths for the growth of ceramic-based materials other than carbon and BN. Even though the increased difficulty to ionize ceramics such as carbon and boron limit the advantage of HiPIMS, alternative solutions were found to completely offset this weakness and ceramic films with high density and quality were successfully obtained using HiPIMS (see Literature review chapter for more details).

Once the setup and proof of concept phase of the HiPIMS system was completed, work on the growth of textured BN was performed. At full optimization, the BN films would be stable and free of delamination or oxidation and a recipe for the growth of vertically aligned h-BN nanocrystals (*voBN*) was obtained for the first time and its formation was linked to the amount of compressive stress applied to the film during growth, inducing a vertical ordering of the basal planes in order to minimize the stored mechanical energy in the material. In addition, a factor 3 improvement in the cross film thermal conductivity was obtained for *voBN* versus a film containing a mixture of cubic and hexagonal BN with random orientation, thereby suggesting that the thermal conductivity of the film is dependent on its crystalline structure orientation.

Following the previous study on the cross plane thermal conductivity of *voBN*, thermal measurements were performed on *voBN* to establish its anisotropic thermal conductivity. In this study, *voBN* cross plane and in plane thermal conductivities were measured to be 4.26 W.m^{-1}.K^{-1} and 0.26 W.m^{-1}.K^{-1} respectively, which yield a ratio of 16 between the two directions. Such anisotropy was assumed to be due to the preferred path in the vertical direction for phonons to travel thanks to the highly vertically ordered nature of *voBN* and Molecular Dynamics simulations successfully verified that assumption by accurately reproducing the same amount of anisotropy as what was found experimentally. Finally, COMSOL simulations showed that using such anisotropy in dense hot spot arrays could allow an increase of hotspot density by a factor 4 at equal thermal performance compared to using SiO_2, thanks to *voBN* being capable of directing the heat away from the hotspot plane, minimizing horizontal heat spread and thus reducing thermal crosstalk. In a similar fashion to BN, the controlled growth of CN with tunable microstructure was for the first time achieved using HiPIMS. This study is the first one measuring the thermal diffusivity of some CN thin films, and attempting to understand what drives the thermal behavior in CN. CN samples were found to have lower thermal diffusivity than pure carbon films and it was suggested that this is due to the introduction of nitrogen in the nanocrystalline structure which introduces additional disorder, and thus impacting the phonon propagation along the film. Additionally, no correlation was found between electrical conductivity and thermal diffusivity, which implies that the key driver for thermal performance in CN is the phonon transport of heat as opposed to the electron transport.

Unlike the previous work performed on NCG which focused mainly on nanostructure study as well as electrical properties of the material, this thesis focused more on the thermal properties of nanocrystalline h-BN in with regards to its nanostructure. Even though BN is electrically insulative, its thermal properties remain good, and show that controlling the film structure and crystal ordering at the nanoscale can have a great impact on the thermal properties of the material at the macroscale. Up until now, and apart from the work performed on BN and CN here, not much research has been performed on the thermal properties of dense thin film materials with varying crystalline ordering. Indeed, most efforts were concentrated on the mechanical properties such as hardness or friction and wear. The thermal study of such materials can potentially open up novel applications of those materials with poorer tribological properties, but yet possess hidden thermal properties thanks to their nanocrystalline ordering.

Currently, not many concrete applications exist in the industry for thin films with anisotropic thermal conductivity. Nonetheless, the ease of production and its simple scalability can unveil new avenues for thermal design in electronics, up to the point where it could become a new standard material used in the circuit packaging production line. This will be discussed more in the following section on further research recommendations.

7.1 Further research recommendations

The work accomplished throughout the past four years has led to many questions being answered when it comes to BN and HiPIMS. However, it also raised many more interesting topics that have yet to be explored.

7.1.1 Boron Nitride

7.1.1.1 Thermal performance test on actual devices

The next step for the work on *voBN* would be to run performance tests on actual devices and compare the results with other typical materials used as an encapsulant for hot spots. Additional simulations should also be run in order to fine tune the result accuracy and enable the extrapolation of theoretical performance for various electronic circuit thermal design. This will allow the comparison in performance between materials with isotropic and anisotropic thermal conductivities. Please refer to Appendix C for more details about a preliminary feasibility study.

7.1.1.2 BN growth with a pure B target

Once the growth of BN with the LaB_6 target was achieved, some work was carried out in attempting to grow BN with a pure B target, requiring system upgrades. The proof of concept milestone for obtaining BN form a B target was achieved, however there was not sufficient time for further work on producing good quality BN films with tunable nanocrystalline structure. Further work on this can be done, in order to achieve greater film quality and compare the obtained BN with the existing *voBN* thermal performances to see whether the presence of lanthanum improves or degrades it.

7.1.1.3 Cubic BN growth with HiPIMS

The growth of high density carbon thin films such as diamond-like carbon has been covered with HiPIMS, but no similar research has been performed for the growth of cubic BN. The main reason is the difficulty to grow BN using HiPIMS, as it relies on using a pure B target and the plasma ionization rate is low, of which case is similar to carbon. As a solution was proposed in the carbon case (see literature review chapter for more details), an equivalent solution for BN might be possible.

7.1.1.4 High quality and large area h-BN monolayer growth

Some work on high quality large area monolayer h-BN film was achieved using the DC magnetron sputtering technique and this work should be reproducible with HiPIMS. In addition, the improved ionization obtained in HiPIMS mode should provide higher h-BN crystal quality, or could enable a lower temperature growth. Such novel avenues of h-BN growth should be explored as it would be of high interest to the industry.

7.1.2 Carbon Nitride

7.1.2.1 Full study of the thermal properties of CN

It has been established that nitrogen plays a key role in the thermal properties of CN and the study of its impact, depending on its concentration, must be evaluated. This could lead to the development of thin films with tunable thermal conductivity, which would have applications in thermal rectification for instance, using a CN film with varying nitrogen content. The previous study was limited to in-plane thermal diffusivity and additional data points are required to compute the thermal conductivity, as well as to obtain the cross-plane thermal conductivity. Fullerene-like CN is most likely an anisotropic material. Combined with its potential tunability with nitrogen doping, full control of its thermal properties can be achieved.

7.1.2.2 Dense CN phases with HiPIMS

Intense research was performed on the beta phase of C_3N_4 as it was predicted to be a material harder than diamond but no irrefutable proof of its existence has been found so far. Attempts to the growth with HiPIMS could succeed where all other methods have failed so far, and as such, it is worthwhile to do so.

7.1.2.3 Graphitic CN with HiPIMS

Up until this point in time, the main growth method for the graphitic structure of C_3N_4 is via CVD, and similar to the beta phase, it is worth investigating the growth with HiPIMS, where it could lead to a new, cheaper and larger scale method of growing carbon nitride.

7.1.3 Boron Carbon Nitride

7.1.3.1 Dual HiPIMS of CN and BN

The natural next step after CN and BN growth would be to combine both materials together in an attempt to selectively harness their individual properties into a BCN compound with tunable characteristics. The HiPIMS setup already supports dual sputtering with a synchronization unit capable of accurately controlling the duty cycles of both BN and CN growth simultaneously (see chapter 3 on HiPIMS). By combining to the low electrical resistance of CN with the high band gap of BN, bandgap engineering of BCN thin films could be accurately explored with HiPIMS.

7.1.3.2 Thermal, mechanical and electrical study of BCN compounds

In addition to bandgap engineering, thermal and mechanical properties of BCN compounds could be carefully measured thanks to the accurate pulse control offered by HiPIMS.

7.1.4 HiPIMS

7.1.4.1 Ion gun upgrade

Further upgrades can be performed for the current HiPIMS system, in particular with adding an ion gun to increase the reaction rate of single nitrogen atoms with the plasma. This could lead to improved results for the growth of nitrides (or even oxides), and the fine tunability of an ion gun when it comes to controlling the ion energy could produce denser material phases previously out of reach. Ion beam assisted growth of materials combined with HiPIMS was never performed before and could lead to the discovery of a new growth method yielding better results and even new materials.

7.1.4.2 Plasma simulation

A deeper understanding of HiPIMS generated plasmas could help a lot in the design of experiments and very little work has been done on it, especially for non-metallic targets where the ionization rate is much lower. Upgrading the HiPIMS system with a plasma analyzer could help understand how a plasma behaves differently from a DC magnetron sputtering generated plasma, and simulations in COMSOL for instance could be run to help optimize the growth to increase plasma ionization or increase the growth rate.

Appendices

1. Appendix A- HiPIMS SOP

The HiPIMS system being a new asset in the laboratory, a complete standard operating procedure (SOP) had to be written and updated to include new upgraded elements. The SOP is divided in three sections: one for fully starting the system and bringing it to readiness level, one on normal conditions operation and the last one on bringing a ready system to full shutdown.

1.1. Preparing system to full readiness

During long periods (more than one week) when the system will not be used, it is brought to full shutdown, when all systems are off. The chamber may be vented or still in vacuum (depending on how long the shutdown was). The steps below describe how to bring the HiPIMS system to full readiness level.

i. Start the water cooler by switching the switch to ON state. Make sure the set point is at 16 degC. Check that all water valves are open and verify that the water flows in the pipes going to the turbomolecular pump, as well as both magnetrons.

ii. On the main rack (right one), switch on the main power of the "Interlock controller" at the top.

iii. Switch on the power supply for the backing pump at the bottom of the main rack.

iv. Open the vent valve at the back of the chamber to pump it down.

v. Switch on both computers.

The system is now in ready mode. The next section will explain how to operate it.

1.2. Growth operating procedure

This section explains how to run an experiment from beginning to end, which includes loading and unloading a sample as well as operating the system to growth thin films.

1.2.1. Sample loading and unloading

i. Check that the temperature is below 100 degC to avoid oxidation during venting.
ii. Shutdown turbomolecular pump using the controller at the bottom of the main rack. The pump frequency should start decreasing from its nominal speed of 820 Hz.
iii. When the frequency falls below 100 Hz, open the vent valve at the back of the chamber.
iv. When the pressure reading reaches 1000 mBar and there is a 1 mm gap between the door and the chamber, close the vent valve tightly.
v. Open the chamber door and load/unload the substrate holder with the sample attached to it. It is safer and easier to use pliers as the substrate holder and surroundings might still be warm.
vi. Once sample is loaded/unloaded, close the chamber door, make sure the door shutter is closed and open the backing valve located at the back of the chamber. Verify that the shutter located between the turbopump and the chamber is fully open to facilitate the pumping down process. Check that the shutters for the target and the substrate holder are closed as well.
vii. Wait until pressure falls below 1 mbar then turn the turbomolecular pump on. The speed reading should increase from 0 Hz up to 820 Hz.

The chamber is now ready for another user and it should take around 3 hours to pump down to an acceptable vacuum to start another growth.

i. If last user of the day: switch off all systems except the two pumps and the main power switch for the rack. Close all gas valves at the MFC and on the wall.
ii. If last user for the week: do step (i) with the additional task of switching off the turbopump and once it reaches a speed below 100 Hz, switch off the water pump by flipping the switch.

1.2.2. Experiment run in HiPIMS mode

This section explains how to run an experiment on the HiPIMS system and assumes it is in ready state, with a sample already loaded in the chamber, and assumes the user has a recipe to use. If user is unsure about recipe, please ask a user admin to ensure it is correct. A wrong recipe could potentially damage the system, and could be dangerous to the user as well!

i. Make sure off the following: water cooling is running, turbopump is running at nominal speed (820 Hz), vacuum is below 1e^{-5} mbars.
ii. On the main rack, switch on the following: substrate table controller, MFC controller, DC power supply of HiPIMS I/II (for the HiPIMS II, the over voltage protection will trigger and need to be disabled – press the "reset" button to do so), then pulsed power supply (Hipster unit) of HiPIMS I/II. Only the HiPIMS unit used should be turned on. Finally, turn on the oscilloscope.
iii. If necessary, turn on DC substrate bias (Chroma), the RF power supply and RF matching unit and/or the heater power supply (TDK Lamdba).
iv. Wait for the MFC controller to heat up (the word "heat" will stop blinking once ready). This usually takes around 5 min.
v. Set the substrate holder rotation speed to match what the recipe requires.

vi. Note down the base pressure in excel spreadsheet in the computer labelled HiPIMS I then open the MFC valves as well as the gas valves on the wall (the gauge on the wall should show around 5 bars pressure) and the main control valve to reach the deposition pressure.

vii. Use the MFC controller to set the gas output to the required value and use the shutter in between the turbopump and the chamber to adjust the growth pressure to the desired value.

viii. If substrate heating is required, adjust the set temperature by pressing the arrow keys "Mode" on Substrate Table controller. To start heating make sure first that the vacuum gauge reads a pressure above $1e^{-3}$ mbars to avoid outgassing, then press the "Out" button on the TDK Lambda power supply.

ix. If DC bias at the substrate is required, check that the red wire coming out from the top of the chamber is connected to DC bias connector instead of the grounded wire. Then turn on the DC power supply (Chroma, for substrate bias) and set the voltage to the desired value, and set the current (on Chroma) set to 0.3A (as a protection limit in case of arcs). Finally, press the "Output" button to enable DC biasing.

x. Start the HiPIMS control software that is located on the desktop of each computer and press Connect.

xi. Setup your recipe using the software, making sure to key Enter every time a parameter is changed. Once the recipe is ready, set the toggle button to "internal", then ON the DC HiPIMS supply (turn the key for HiPIMS I, press On button for HiPIMS II) and finally start plasma by switching the toggle button from Off to On in the software. If growth parameters are correct, plasma should be visible in the chamber. If unsure about the parameters, please check with a system admin first before attempting an experiment.

xii. To start deposition, open the sample holder shutter for the defined amount of time required by the recipe and write down the deposition parameters in the excel spreadsheet on the computer HiPIMS I.

xiii. To finish the growth, change the Pulse toggle button to Off in the software controller and set the DC power supply for HiPIMS to Off state (either turn the key for HiPIMS I or press the "Off" button for HiPIMS II).

xiv. Stop the heater by pressing the "Output" button on the heater power supply.

xv. Check that the temperature is below 100 degC and stop the gas input from the MFC to prevent outgassing.

The experiment is now finished. Check the section about loading/unloading samples for the unloading steps.

1.2.3. Experiment run in RF mode

i. Do the same as steps (i) to (ix) explained in section 2.

ii. Check the no power is being output in either RF or HiPIMS, then switch the coaxial cable feeding the magnetron to the RF one.

iii. On the RF power supply, set the forward power to 50 W and press the "on" button. The light should change from blue to red and a reflected power should be displayed. Fine tune the matching using the matching controller so that the reflected power is close to 0 W then increase the forward power to the desired power by increments of 50 W and making sure the reflected power remains below 10 W. If the plasma does not start, increase the pressure by adjusting the vacuum shutter or increase the MFC flow rate. Once the plasma is started, decrease the flow rate back to the desired value.

iv. To start deposition, open the sample holder shutter for the defined amount of time required by the recipe and write down the deposition parameters in the excel spreadsheet on the computer HiPIMS I.

v. To finish the growth, press the "Off" button on the RF power supply.

vi. Stop the heater by pressing the "Output" button on the heater power supply.

vii. Check that the temperature is below 100 degC and stop the gas input from the MFC to prevent outgassing.

The experiment is now finished. Check the section about loading/unloading samples for the unloading steps.

1.3. Full system shutdown

If the system is not being used for more than a week, it is better to fully switch it off, to reduce the risk of any issue occurring with no one to notice it.

i. If not the case yet, bring the system to full readiness first, in the case of a closing for the weekend. The turbopump and water cooling should be shutdown.
ii. Close the backing valve at the back of the chamber.
iii. Switch off the backing pump using the switch at the bottom of the main rack.
iv. Switch off the main rack using the button at the top left of it.
v. Switch off the computers.

The chamber should be capable of maintaining a fairly acceptable vacuum for over a week without the backing pump running.

2. Appendix B- HiPIMS maintenance

The HiPIMS setup requires regular maintenance in order to have it perform to its optimal capabilities. This section describes what is done for maintenance as well as the various system failures that occurred and how they were solved.

2.1. Standard maintenance work

There is regular work to perform to keep the system working at optimal capacity and they are listed below.

2.1.1. Chamber cleaning

When growing materials, some of the sputtered species will deposit themselves on the chamber walls. After a certain thickness is reached, it will peel off the chamber walls and create small flakes and dust, which can contaminate samples a swell as making the chamber pump down much slower. The chamber is usually cleaned with the use of IPA and non-abrasive scouring pads. In order to facilitate the cleaning, some chamber wall shields were installed. Those shields can be removed easily from the chamber and are easier to clean. The chamber is cleaned every 6 months to ensure the best vacuum conditions.

2.1.2. Vacuum gauge cleaning

The HiPIMS chamber is used for the growth of dielectric material. Those materials will eventually coat the chamber walls, and especially at the vicinity of the vacuum gauge were the space is confined, will create charging during growth, which will tend to locally increase the plasma density as the negative charging at the walls will repulse the ions in the plasma. This accumulation of charges has the effect of locally increasing the pressure at the vacuum gauge, making the reading higher than what it should be. In order to avoid misreading the pressure, another vacuum gauge was installed to double check the reading, as well as a regular monthly (or whenever the pressure reading seems too high) cleaning of the wall at the area around the vacuum gauge.

2.1.3. Magnetron cleaning

The magnetron is made up the main magnetron body made of copper, the target holder and target (cathode) and the anode which is connected to the ground through the magnetron body. Both anode and cathode are made of molybdenum and require cleaning at least once a month when used with the same target as the target materials will deposit themselves on the parts and peel off, which could create extra dust and potential shorts between anode and cathode. The magnetron will also need to be cleaned every time the target is changed in order to avoid contamination between the different target materials.

2.1.4. Substrate holder cleaning

There are 4 substrate holders currently used in the HiPIMS system. One for BN growth, one for carbon based materials, one for compound materials using both magnetron simultaneously, and the last one is for metallic growths. This separation is required to avoid contamination at the sample, and in order to keep it to a minimum, the target holders are cleaned monthly, in a similar fashion to the magnetrons.

2.1.5. Changing magnetron target

Targets are regularly changed depending on the type of growth the user wants. When changing the target, one must be careful not to break the targets as they are quite fragile (especially ceramic ones) and the resistance between anode and cathode must be checked and be of the order of the megaohm to ensure a proper glow discharge.

3. Appendix C – Experimental comparison of SiO_2 and *voBN*

Building an actual testing apparatus comparing *voBN* with any other material was looked into during this thesis. However, after further consideration and running simulations, it was quickly abandoned as the task required to successfully build an experimental test device were extremely complex.

3.1. Thin film on heater simulations

There was an actual attempt at building some test apparatus to compare the thermal performance of SiO2 and *voBN* (as well as any other future thin film material). However, this is no trivial matter: simulations of a heater covered with a SiO_2/BN layer showed not a single difference in temperature between the 2 materials. This is due to the very small material thickness that can be neglected in front of other physical factors impacting the temperature, such as the heat dissipation from the bottom of the device, through the substrate. Indeed, to compare the thermal resistance of *voBN* and SiO_2. Two factors are contributing to this resistance: the material thermal conductivity T_c , which is dependant on the Boundary Line Thickness (BLT) l_{BLT} . The second term is the thermal interface resistance $R_{Si-voBN}$ which is the contact resistance between silicon and *voBN*. The thermal resistance R_T can then be written as seen in the equation 1 below:

$$R_T = \frac{l_{BLT}}{T_c} + \frac{R_{Si-voBN}}{a} \quad \text{K/W} \qquad (1)$$

a is the area of contact of the interface. The issue here is that l_{BLT} for *voBN*, $R_T = 8.25\text{e-}3$ K/W for a surface contact of 1 cm^2, while R_T for SiO_2 would be

9.87e-3 K/W. When running a simple simulation with those 2 resistance values on a small 10 mm by 10 mm heating chip of 1 W of heating power, the maximum temperature reaches 210 degC for both materials. The simulation results are shown in Figure 1 below. Note that the simulation uses symmetries, on the x-z and y-x planes, in order to cut by 4 the amount of computation. In this simulation, the heat seems to be trapped in the device, as only a natural convective heat flux was applied on top of the device. A more standard design would be to apply a heatsink on top of the device so that the thermal interface material becomes the heat extraction bottleneck, which would highlight any difference in performance between materials.

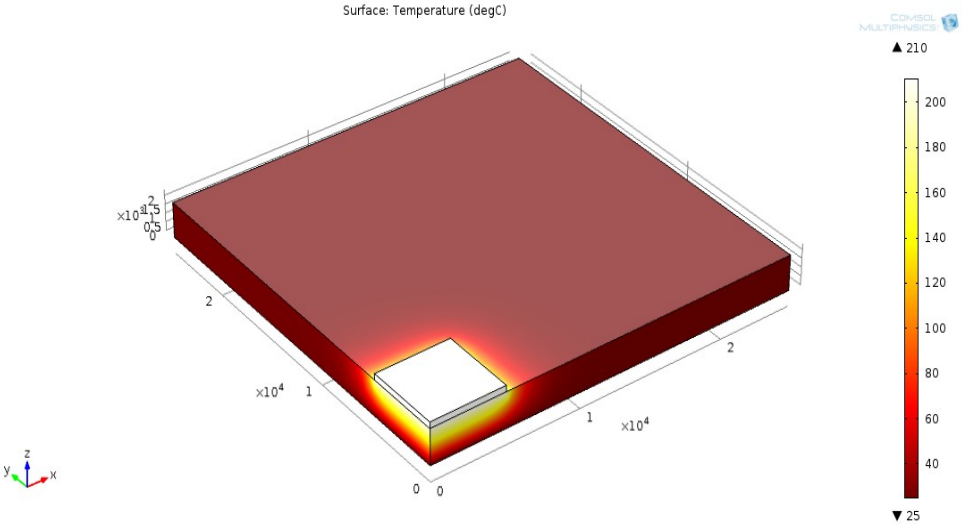

Figure 1 - Simple COMSOL simulation of the thermal behaviour of a 1 cm x 1 cm heater. The power output is 1 W and the bottom surface has a temperature condition set to 25 degC. The top surfaces are cooled down by natural air convection. A symmetry condition is used on the x-z and y-z planes to divide by 4 the computation time.

3.2. Heat sink coupled simulations

However this approach has a big problem: it requires the use of thermal paste to make the contact between the thin material and the heat sink, introducing another set of thermal resistances, such as $R_{voBN-paste}$ which is the thermal contact resistance between the thermal paste and the *voBN*/SiO_2 layer, $R_{paste-heatsink}$ which is the thermal contact resistance between the paste and the heatsink, and finally

$l_{BLT-paste}/T_{c-paste}$ which is the thermal resistance contribution from the thermal paste ifself. Here, we would need to experimentally compute $R_{voBN-paste}$ first, using the ASTM standard. The second step would be to sum all contributions and this is where the issue arises: the thermal contact resistance and BLT of the thermal paste is over an order of magnitude higher than the other contributions at $R_{paste-heatsink}=7\text{e-}2$ K/W and $l_{BLT-paste}/T_{c-paste}=4.17\text{e-}2$ K/W for the best thermal paste compounds found in the industry, meaning that the thermal paste contribution to the thermal resistance would make the thin film contribution negligible, which defeats the purpose. Assuming here we have $R_{paste-heatsink}=R_{voBN-paste}$, we get a total thermal resistance R_T of 0.112 K/W, 0.191 K/W and 0.193 K/W for respectively the thermal paste applied directly on the heating element, *voBN* and the thermal paste, and finally SiO_2 and the thermal paste. Here, an input of 10 W was applied as much more heat could be extracted through the heatsink, and the temperature condition of 25 degC was applied on the top surface of the sink. For the thermal paste alone, a maximum temperature of 43.3 degC was obtained, and for *voBN* and SiO_2, the same temperature of 44.1 degC was obtained (see Figure 2). The increase of 0.8 degC between the experiment with the thermal paste alone and the *voBN*/SiO_2 thin film plus thermal paste makes sense as any additional layer would increase the overall thermal resistance, however good the layer is.

However this approach has a big problem: it requires the use of thermal paste to make the contact between the thin material and the heat sink, introducing another set of thermal resistances, such as $R_{voBN-paste}$ which is the thermal contact resistance between the thermal paste and the *voBN*/SiO_2 layer, $R_{paste-heatsink}$ which is the thermal contact resistance between the paste and the heatsink, and finally

$l_{BLT-paste}/T_{c-paste}$ which is the thermal resistance contribution from the thermal paste itself. Here, we would need to experimentally compute $R_{voBN-paste}$ first, using the ASTM standard. The second step would be to sum all contributions and this is where the issue arises: the thermal contact resistance and BLT of the thermal paste is over an order of magnitude higher than the other contributions at $R_{paste-heatsink}=7\text{e-}2$ K/W and $l_{BLT-paste}/T_{c-paste}=4.17\text{e-}2$ K/W for the best thermal paste compounds found in the industry, meaning that the thermal paste contribution to the thermal resistance would make the thin film contribution negligible, which defeats the purpose. Assuming here we have $R_{paste-heatsink}=R_{voBN-paste}$, we get a total thermal resistance R_T of 0.112 K/W, 0.191 K/W and 0.193 K/W for respectively the thermal paste applied directly on the heating element, *voBN* and the thermal paste, and finally SiO_2 and the thermal paste. Here, an input of 10 W was applied as much more heat could be extracted through the heatsink, and the temperature condition of 25 degC was applied on the top surface of the sink. For the thermal paste alone, a maximum temperature of 43.3 degC was obtained, and for *voBN* and SiO_2, the same temperature of 44.1 degC was obtained (see Figure 2). The increase of 0.8 degC between the experiment with the thermal paste alone and the *voBN*/SiO_2 thin film plus thermal paste makes sense as any additional layer would increase the overall thermal resistance, however good the layer is.

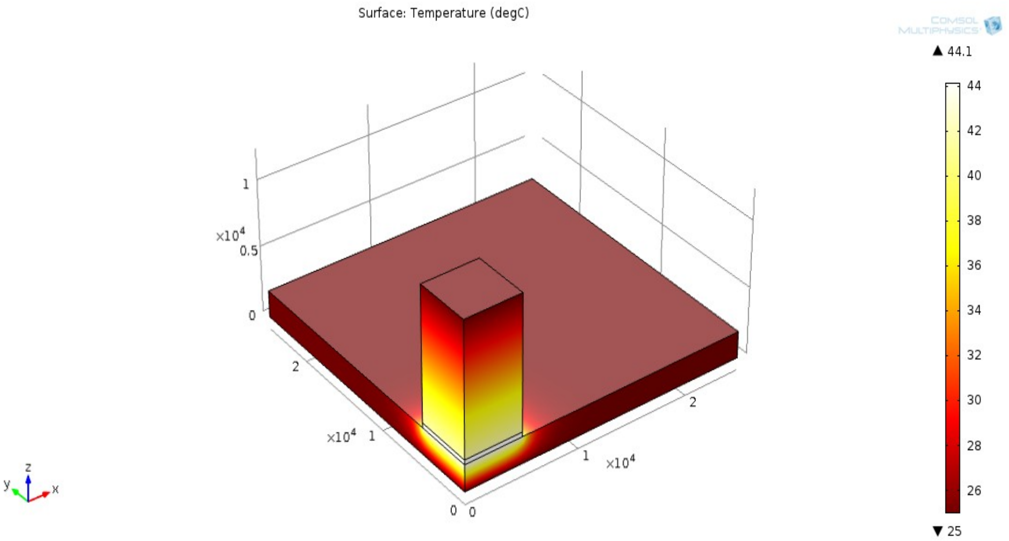

Figure 2 - Simple COMSOL simulation of the thermal behaviour of a 1 cm x 1 cm heater with a 1 cm high heatsink on top. The power output is 10 W and the bottom surface has a temperature condition set to 25 degC. The top surfaces are cooled down by natural air convection, except for the top surface of the heatsink which has a temperature condition of 25 degC. A symmetry condition is used on the x-z and y-z planes to divide by 4 the computation time.

3.3. Testing the anisotropy of *voBN*

In addition, the true greatness of *voBN* resides in its anisotropic thermal behaviour, which is not tested in this type of experiment. One would like to investigate the effect of anisotropy, and for that it is required to have heating elements of similar size to the film thickness, which is below 1 µm. Also, an array of heaters should be made, with varying distances between them, as well as another array of temperature probes to measure the temperature as varying distances between each heating element. In addition, the problem gets more complex when trying to understand how much the probes impact the thermal performance of the whole device, as their number and size cannot be neglected in the overall thermal computations. This is why this real-life testing step was put in the further research recommendation list, as it would take a considerable amount of time to design, build and test a testing apparatus for live-testing the thermal performance of thin film materials.